The University of Osaka
Institutional Knowledge Archive

Title	Proposal and numerical analysis of the semiconductor nanogap microcavities
Author(s)	植本, 光治
Citation	大阪大学, 2014, 博士論文
Version Type	VoR
URL	https://doi.org/10.18910/34513
rights	
Note	

The University of Osaka Institutional Knowledge Archive : OUKA

https://ir.library.osaka-u.ac.jp/

The University of Osaka

Proposal and numerical analysis of the semiconductor nanogap microcavities

A dissertation submitted to
THE GRADUATE SCHOOL OF ENGINEERING SCIENCE
OSAKA UNIVERSITY
in partial fulfillment of the requirements for the degree of
DOCTOR OF PHILOSOPHY IN SCIENCE

BY

MITSUHARU UEMOTO

MARCH 2014

Abstract

When a light illuminates metallic nanoparticles, a strongly enhanced electric field appears on the surface due to the excitation of a surface plasmon. For a metallic nanodimer, the strong enhanced field appears at the nanogap, and thus, this system can act as an optical cavity. However, the quality factor (*Q* factor) of such a plasmonic cavity is extremely low ($Q \approx 10$) because of the large plasmon damping. The improvement of the *Q* factor is expected to be achieved by utilizing exciton resonance of semiconductor nanostructures because the damping rate of an exciton is much smaller than that of the plasmon.

In this thesis, I theoretically propose and design semiconductor nanogap as a new high-Q cavity, utilizing the exciton effect. In general, electromagnetic (EM) simulation methods such as a finite-difference time-domain (FDTD) method are usually employed to analyze the performance and determine the optimal design of various optical devices. However, the established simulation methods cannot be applied to semiconductor having exciton resonance because of the nonlocality of a dielectric function near the exciton resonance. At first, therefore, I develop a simulation method to calculate the EM field scattered by semiconductor nanostructure taking account of an exciton confined in arbitrary geometry.

We consider the nanogap structure constructed by two CuCl islands, and calculate EM fields using the developed simulation method. A light field at the nanogap is significantly enhanced by a factor of $\approx 10^3$. This enhancement factor is about 10 times

smaller than that of metallic nanogap with the same structure. However, the semiconductor nanogap exhibits much higher Q factor ($Q \approx 10^4$) at $T = 40°K$ than that of a metallic nanogap. The result indicates that the semiconductor nanogap functions as a high-performance optical cavity.

In order to demonstrate the performance of the semiconductor nanogap cavity, a vacuum-Rabi splitting of a two-level system placed at the nanogap is calculated. The resulting spectral peaks exhibit clear anti-crossing behavior. The Rabi splitting energy reaches $\approx$ 0.5 meV for dipole moment $\approx$ 10 Debye of the two-level system, and is much larger than that for the two-level system with the same dipole moment embedded in a photonic slab cavity or micropillar cavity. This result shows that the proposed semiconductor nanogap cavity acts as an efficient cavity.

Contents

Chapter 1

Introduction

Resonant excitation of a surface plasmon in metallic nanostructures induces a very intense electromagnetic (EM) field, which is called a hotspot, in a nanometer-scale region. This interesting optical properties pave the way to a plasmonics. In the past decade, the plasmonics has been attracted much attention because of their potential applications, such as the biochemical sensing, surface-enhanced Raman spectroscopy (SERS) [21], the optical manipulations [31], the application to the antenna operated in the optical frequencies [20], and other various challenging applications. In particular, a nanogap constructed by metallic islands generates an extensively strong field at the gap region due to a so-called gap-mode plasmon, and the field strength is amplified by a factor of $10^4 \sim 10^6$ [32, 14].

The nanogap structures can be considered as a photonic cavity because of the strong light confinement. However, the relaxation time of plasmon modes is very fast ($10 \sim 100$ fs) due to the electron-electron scattering, and the fast relaxation time lowers the performance of the photonic cavity. In general, the efficiency of the photonic cavity is specified by a quality factor (Q factor), which is defined as the ratio between an energy loss and a stored energy. The Q factor of the metallic nanogap cavity is limited to $\approx 10^1$ [33] because of the short relaxation time of the plasmon.

In photonic cavities, a light-matter interaction becomes very strong, and thus, the interaction occurs at one-photon level. In this situation, light in the cavity should be treated as photons in the cavity quantum electrodynamics (cQED). One of the characteristic features of the cQED is the vacuum-field Rabi splitting of the two coupled states of material exciton and a cavity-mode photon (strong-coupling regime). Recently, the Rabi splitting of a quantum dot (QD) in photonic cavities has been observed [34, 25, 23]. The realization of the semiconductor-based Rabi splitting is desired in applications of a quantum information processing and quantum computation, for example, an efficient entangled photon generation in the strong-coupling regime is predicted [3].

The Rabi splitting energy becomes larger for smaller cavity-mode volume in addition to the larger oscillator strength of a matter. The spectral width corresponding to the coupled states becomes narrower with increase of the Q factor. Therefore, the small cavity-mode volume and large Q factor are necessary for photonic cavities to observe a clear Rabi splitting.

In previous experiments, the photonic crystal cavity [34], the micro-pillar cavity [25], and the micro-disk cavity [23] are utilized to observe the vacuum Rabi splitting. For conventional photonic cavities, however, the cavity-mode volume is restricted to the volume characterized by the light wavelength (diffraction limit). The cavity-mode volume of metallic nanogap cavities reaches the cube of subwavelength exceeding the diffraction limit.

Schlather *et. al.* [29] have reported the observation of a giant Rabi splitting of molecular excitons placed at the metallic nanogap cavity. Although the Rabi splitting is large, each spectral width of the two peaks is very broad and comparable to the splitting energy because of the large plasmon damping. However, a clear Rabi splitting is expected to be observed by constructing a nanogap structure using semiconductor having exciton resonance.

In this thesis, we propose and analyze a new type of the photonic cavity constructed by semiconductor nanostructures, in which resonant scattering by exciton causes a hotspot at the nanogap. The spectral width of the confined exciton is much smaller than that of the surface plasmon, and thus, the cavity Q factor is significantly improved. The semiconductor nanogap cavity has also small mode volume exceeding the diffraction limit. Consequently, a clear Rabi splitting of ≈ 0.5 meV is theoretically demonstrated for dipole moment of ≈ 10 Debye of a two-level system (a QD or molecules) placed at the nanogap. This splitting energy is much larger than that for the two-level system with the same dipole moment embedded in a photonic slab cavity or micropillar cavity.

For this purpose of the above-mentioned numerical simulations, I have developed a simulation method to calculate the EM field scattered by semiconductor nanostructure taking account of an exciton confined in arbitrary geometry. The general EM simulation methods such as a finite-difference time-domain (FDTD) method are usually employed to analyze the performance and determine the optimal design of various optical devices. However, the established simulation methods cannot be applied to semiconductor having exciton resonance because of the nonlocality of a dielectric function near the exciton resonance. The developed method overcomes this difficulty by added in an additional boundary condition to a finite-element method (FEM). To avoid spurious solutions and enhance the precision, I have also developed a hybrid edge-nodal element formulation in the FEM. The developed method is confirmed to be valid through a comparison with the scattering cross section of a spherical semiconductor calculated by Mie theory. This method provides well-resolved characteristic polarization patterns reflecting the size-quantized exciton. The developed method makes it possible to design the optical functions of semiconductor nanostructures such as semiconductor nanogap cavity for the first time.

This thesis is organized as follows. In Chap. 2, the general formalism of the FEM for EM simulations of dielectric material is described. The mathematical background of the FEM is also explained. Although these simulations are limited to dielectric material and metal, it is quite useful and effective in the fascinating research fields of plasmonics and metamaterials. In Chap. 3, I develop a new simulation method to calculate the EM field scattered by exciton confined in arbitrary geometry. In Chap. 4, I propose a semiconductor nanogap cavity. Toward to the optimal design of the semiconductor nanogap cavity, the angle dependence of the enhancement factor is studied for a bow-tie shaped structures. In Chap. 5, I theoretically demonstrate the vacuum-Rabi splitting of a two-level emitter placed at the gap region of the semiconductor nanogap cavity. Finally, I conclude the discussion of the main results of this thesis in Chap. 6.

Chapter 2

General Formalism of Finite Element Method

The present chapter overviews the general formalism of the finite element method (FEM) [17], which is employed to solve the Maxwell equations in this study. The FEM is known as a technique for solving the boundary-value problems of partial differential equations defined over the arbitrary shaped region. The boundary-value problems appear in many physical systems, and thus the numerical methods to solve those problems are quite useful. The FEM was originally developed for the problems of structural mechanics. Currently, the FEM has been applied to a wide range of physical problems, such as the fluid dynamics, thermodynamics, quantum mechanics and electromagnetic (EM) problems.

In the former part of this chapter, two major formalisms to treat the boundary-value problems are introduced: the Galerkin and Ritz methods. In the latter part, we discuss the computation of the Maxwell's wave equation, which governs the EM field in the media, for one-dimensional (1D), two-dimensional (2D) and three-dimensional(3D) systems.

At first, we consider a typical differential equation:

$$\hat{\mathcal{L}}\phi = f \ , \tag{2.1}$$

where $\hat{\mathcal{L}}$ is the differential operator, ϕ is the unknown function to be determined, and f is the forcing function corresponding to the source term such as a charge or current in the EM problems. We shall provide the numerical method to solve Eq. (2.1). In the numerical computations, the continuous function ϕ is approximated by the linear combination of a finite number of basis functions u_i as follows:

$$\tilde{\phi} = \sum_i c_i u_i \ , \tag{2.2}$$

where c_i is the unknown Expansion coefficient and $\tilde{\phi}$ is the approximated function called "trial function". There are two major approaches to determine the optimal c_i: weighted residual method (WRM) and Ritz method. Although the Ritz method, which is described later, is limited to the positive-definite Hermitian operator, the Galerkin method can be applied to a general problem.

2.1 Weighted residual method

2.1.1 Weighted residual

A residual is defined as the error caused by substituting the approximated solution into the differential equation. We define a residual of the trial function $\tilde{\phi}$ as follows:

$$r = \hat{\boldsymbol{\mathcal{L}}}\tilde{\phi} - f \ . \tag{2.3}$$

If the $\tilde{\phi}$ is the exact solution of Eq. (2.1), r becomes zero at every positions.

Taking a inner product with a weighting function ω_i, we get a weighted residual R_i:

$$R_i = (\omega_i, r) = (\omega_i, \hat{\boldsymbol{\mathcal{L}}}\tilde{\phi}) - (\omega_i, f) \ , \tag{2.4}$$

where (ω_i, r) represents the inner product defined as

$$(\omega_i, r) = \int \mathrm{d}\boldsymbol{\xi} \ \omega(\boldsymbol{\xi})^* r(\boldsymbol{\xi}) \ . \tag{2.5}$$

In the WRM, $\tilde{\phi}$ is determined such that the weighted residual becomes zero, and thus, $\tilde{\phi}$ is obtained by imposing

$$R_i = \sum_j (\omega_i, \hat{\mathcal{L}} u_j) c_j - (\omega_i, f) = 0 \ . \tag{2.6}$$

for all ω_i. This condition yields simultaneous linear equations:

$$\{L_{ij}\}\{c_j\} = \{f_i\} \ , \tag{2.7}$$

with

$$L_{ij} = (\omega_i, \hat{\mathcal{L}} u_j) \ , \tag{2.8}$$

$$f_i = (\omega_i, f) \ . \tag{2.9}$$

Note that the number of weighting functions should be equal to the number of the unknown variables c_j.

2.1.2 Weighting function

There are some kinds of the weighting functions ω_i. Here, we explain four popular methods: Galerkin method, point matching method, subdomain collocation method, and least square method

Galerkin method

The Galerkin method is known as the most popular formalism among the family of WRMs, and this method leads to the same simultaneous linear equations derived from the Ritz method.

In the Galerkin method, the basis function u_i in Eq. (2.2) is used as the weighting function ω_i, and L_{ij} and f_i in the simultaneous linear equations [Eq. (2.7)] are given by

$$L_{ij} = (u_i, \hat{\mathcal{L}} u_j) \ , \tag{2.10}$$

and

$$f_i = (u_i, f) \ , \tag{2.11}$$

respectively.

Point matching method

In the point matching method or the point-collocation method, we impose the trial function to satisfy Eq. (2.1) at specific points:

$$\hat{\mathcal{L}}\tilde{\phi}(\boldsymbol{\xi}_i) = f(\boldsymbol{\xi}_i). \tag{2.12}$$

This condition is equivalent to select the Dirac's delta function as the weighting function:

$$\omega_i(\boldsymbol{\xi}) = \delta(\boldsymbol{\xi} - \boldsymbol{\xi}_i) \ . \tag{2.13}$$

The resulting weighted residual is given by

$$R_i = \sum_j \hat{\mathcal{L}}\tilde{\phi}_j(\boldsymbol{\xi}_i)c_j - f(\boldsymbol{\xi}_i) \ . \tag{2.14}$$

Subdomain collocation method

In the Subdomain collocation method, we impose the average of the residuals to be zero in a specified area. We divide an entire domain Ω into a set of subdomains Ω_i:

$$\Omega = \Omega_1 \cup \Omega_2 \cup \cdots \cup \Omega_n \ . \tag{2.15}$$

The weighting function ω_i is defined to be a constant in the subdomain Ω_i and zero elsewhere:

$$\omega_i(\boldsymbol{\xi}) = \begin{cases} 1 & \boldsymbol{\xi} \in \Omega_i \\ 0 & \boldsymbol{\xi} \notin \Omega_i \end{cases} \tag{2.16}$$

The resulting weighted residual is given by

$$R_i = \sum_j c_j \int_{\Omega_i} \hat{\mathcal{L}} u_j(\boldsymbol{\xi}) d\boldsymbol{\xi} - \int_{\Omega_i} f(\boldsymbol{\xi}) d\boldsymbol{\xi} \ . \tag{2.17}$$

Least square method

In the least square method, we consider the square of residual:

$$I = \frac{1}{2} \int \left\| \hat{\mathcal{L}} \tilde{\phi} - f \right\|^2 \tag{2.18}$$

$$= \frac{1}{2} \int \sum_{ij} c_i^* c_j \left(\hat{\mathcal{L}} u_i, \hat{\mathcal{L}} u_j \right) - \sum_i c_i^* \left(\hat{\mathcal{L}} u_i, f \right) - \sum_j c_j \left(\hat{\mathcal{L}} f, u_j \right) + |f|^2 \tag{2.19}$$

The best approximated solution $\tilde{\phi}$ is obtained form the condition to minimize I with respect to c_i:

$$\frac{\partial I}{\partial c_i^*} = \int \left(\hat{\mathcal{L}} u_i \right) \left(\sum_j \hat{\mathcal{L}} c_j u_j - f \right) = 0 \ . \tag{2.20}$$

Comparing to Eq. (2.4), this condition is equivalent to the WRM with the weighting function ω_i defined by

$$\omega_i = \hat{\mathcal{L}} u_i . \tag{2.21}$$

2.2 Ritz method

The Ritz method is an approach based on a variational principle. In this method, one can obtain the optimal approximate solution by searching minimum of an appropriate functional leading to a governing equation. For example, let us consider a functional leading to Eq. (2.1):

$$\mathcal{F}[\phi] = \frac{1}{2} \left(\phi, \hat{\mathcal{L}} \phi \right) - \frac{1}{2} (\phi, f) - \frac{1}{2} (f, \phi) \ . \tag{2.22}$$

The stationary condition of the functional provides Eq. (2.1). Taking the variation of Eq. (2.22), we get

$$\begin{aligned}\delta\mathcal{F} &= \mathcal{F}[\phi+\delta\phi]-\mathcal{F}[\phi] \\ &=\frac{1}{2}\left(\delta\phi,\hat{\mathcal{L}}\phi\right)+\frac{1}{2}\left(\phi,\hat{\mathcal{L}}\delta\phi\right)-\frac{1}{2}(\delta\phi,f)-\frac{1}{2}(f,\delta\phi) \\ &=\frac{1}{2}\left(\delta\phi,\hat{\mathcal{L}}\phi-f\right)+\frac{1}{2}\left(\hat{\mathcal{L}}\phi-f,\delta\phi\right) , \end{aligned} \tag{2.23}$$

and the stationary condition is given by

$$\delta\mathcal{F}=\frac{1}{2}\left(\delta\phi,\hat{\mathcal{L}}\phi-f\right)+\frac{1}{2}\left(\delta\phi,\hat{\mathcal{L}}\phi-f\right)^{*}=0 ,$$

where we have used the definition of the self-adjoint operator $\mathcal{L}$:

$$\left(\phi,\hat{\mathcal{L}}\psi\right)=\left(\phi\hat{\mathcal{L}},\psi\right) . \tag{2.24}$$

Thus, the exact solution of Eq. (2.1) is derived from the stationary condition of the functional (2.22). Let us consider the second-order variational of $\mathcal{F}$:

$$\delta^2\mathcal{F}=\delta\mathcal{F}[\phi+\delta\phi]-\delta\mathcal{F}[\phi]=\left(\delta\phi,\hat{\mathcal{L}}\delta\phi\right) . \tag{2.25}$$

Because $\hat{\mathcal{L}}$ is a positive definite operator:

$$\left(\delta\phi,\hat{\mathcal{L}}\delta\phi\right)\geq 0 , \tag{2.26}$$

we have

$$\delta^2\mathcal{F}\geq 0 . \tag{2.27}$$

Therefore, the stationary point is the minimum of the functional, and the minimum condition of $\mathcal{F}$ provides the governing equation (2.1).

Similar to the case of WRM, we expand the $\tilde{\phi}$ by Eq. (2.2) and substitute it into Eq. (2.22).

$$F[c_i]=\frac{1}{2}\sum_{ij}c_i^{*}c_j\left(u_i,\hat{\mathcal{L}}u_j\right)-\frac{1}{2}\sum_{i}c_i^{*}(u_i,f)-\frac{1}{2}\sum_{j}c_j(f,u_j) . \tag{2.28}$$

Taking a partial derivative of c_i^*, we have

$$\frac{\partial F}{\partial c_i^*} = \frac{1}{2}\left[\sum_j \left(u_i, \hat{\mathcal{L}} u_j\right) c_j - (f, u_j)\right] . \tag{2.29}$$

Taking $\partial F/\partial c_i^* = 0$ for all the c_i, we get simultaneous linear equations. Note that the linear equations have the same form as Eq (2.7) with Eqs. (2.10) and (2.11) when $\hat{\mathcal{L}}$ is the positive-definite and self-adjoint operator. Namely, the Ritz method is equivalent to the Galerkin method.

2.3 Basis function

In the previous section, we have introduced formalisms to compute differential equations: the WRM and Ritz method. In both methods, the appropriate basis functions are necessary for the discretization in numerical computations. In this section, we describe several kinds of the basis functions: the nodal and edge basis.

In general, it is impossible to find analytic basis functions suitable for an arbitrary geometry. In the FEM, the entire computation domain is subdivided into the set of small subdomains so-called *volume elements* as shown in Fig. 2.1. All the volume elements are labeled by a set of integers $e = 1, 2, \cdots$, and the nodes of each element are labeled as $i = 1, 2, \cdots$. The ith node in the eth element is denoted by a local label $(e; i)$. The ith node in the eth volume element is denoted by a local label $(e; i)$. Any node can be indicated by multiple local labels because the node belongs to multiple volume elements. For one-to-one mapping between the nodes and integers, we create a global label $s(e; i) = 1, 2, \cdots$ for all nodes. The triangular element at the interface belonging to the eth volume element is denoted by f_e.

For a 1D model, the elements are usually short line segments. The points dividing the whole region (line) into the segments denote the nodes. For a 2D model, small triangles are usually adopted as the elements. The three vertexes of the triangles denote the nodes of the element.. For a 3D model, small tetrahedrons are usually adopted as the elements. The four vertexes of the tetrahedrons denote the nodes of the elements.

(a) One-dimensional problem

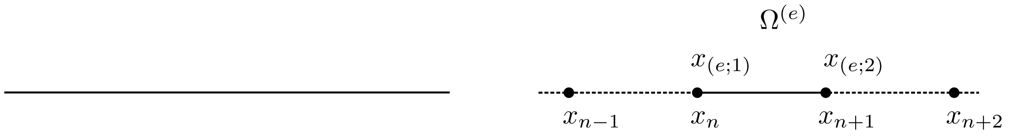

(b) two-dimensional problem

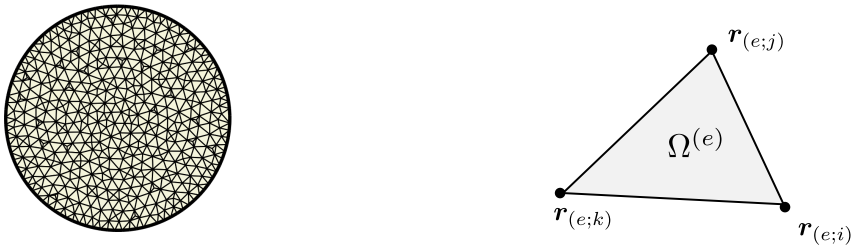

(c) three-dimensional problem

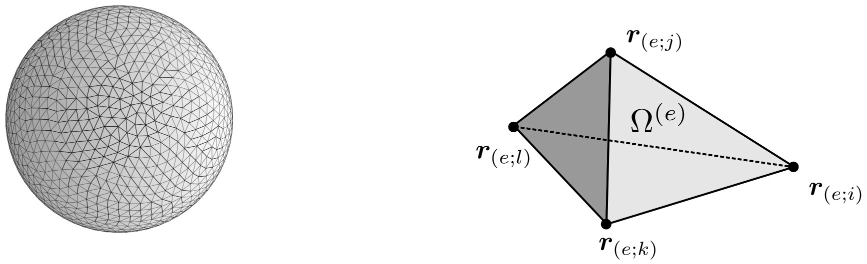

Figure 2.1: Basic finite elements. (a) One-dimensional element (line segment). (b) Two-dimensional element (triangle). (c) Three-dimensional element (tetrahedron)

For 1D case, the computation domain is expressed as a line bounded by

$$x_{\min} \le x \le x_{\max} \ . \tag{2.30}$$

In the discretization of the line domain, we consider the points dividing the line into several segments:

$$x_{\min} = x_1 < x_2 < \cdots < x_N = x_{\max} \tag{2.31}$$

where the dividing points $x_1, x_2, \cdots, x_N$ denote the nodes of the element represented by the global label, and the line segment $(x_i \le x \le x_{i+1})$ denotes the i-th elements as shown in Fig. 2.2]

The approximated basis function within a segment is obtained from a linear interpolation, and the resulting basis function is represented by

$$\tilde{\phi}(x) = \frac{x_{i+1} - x}{x_{i+1} - x_i}\phi_i + \frac{x - x_i}{x_{i+1} - x_i}\phi_{i+1}, \quad (x_i \le x < x_{1+1}) \ , \tag{2.32}$$

where $\phi_i = \phi(x_i)$ is given. In the local-label representation, thus, $\phi(x)$ in the whole region is given by

$$\tilde{\phi}(x) = \sum_e \sum_{i=1,2} \phi_{(e;i)} L_{(e;i)}(x) \tag{2.33}$$

with

$$L_{(e;i)}(x) = \begin{cases} \frac{x_{(e;i+1)} - x}{x_{(e;i+1)} - x_{(e;i)}} & (i = 1,\ x_{(e;i)} \le x < x_{(e;i+1)}) \\ \frac{x - x_{(e;i)}}{x_{(e;i+1)} - x_{(e;i)}} & (i = 1,\ x_{(e;i)} \le x < x_{(e;i+1)}) \\ 0 & (\text{Otherwise}) \end{cases} \ , \tag{2.34}$$

where e is the index of an element, $i = 1, 2$ is the local index of the two ends, and $(e; i)$ denotes the local label of a node i within element e. The function L is the interpolation function also known as the expansion or basis function. As shown in Eq. (2.34), $L_{(e;i)}(x)$ is non-zero linear function defined within the element e. Because of $L_{(e;i)}[x_{(e;i)}] = L_{(e;i)}[x_{(e;i+1)}] = 1$ the expansion coefficient $\phi_{(e;i)}$ agrees with the value of $\tilde{\phi}(x)$ at the node $x_{(e;i)}$. Therefore,

(a) Exact solution

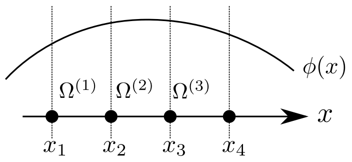

(b) Basis functions

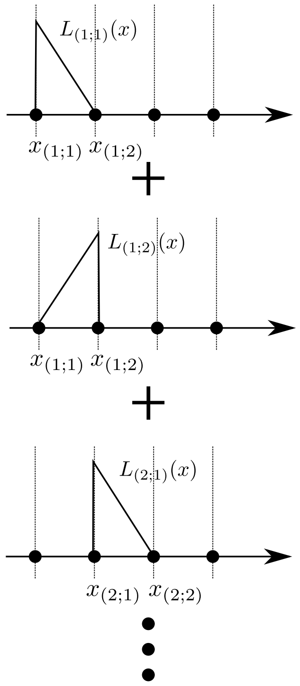

(c) Approximated solution

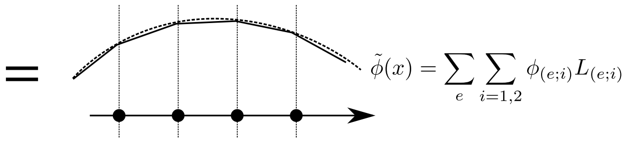

Figure 2.2: A schematic illustration of the linear interpolation and the basis.

this basis is called a *nodal basis.*

For the 2D case, triangles with three nodes are usually adopted as the geometry of the volume elements. The nodal basis function is written as

$$L_{(e;i)}(x,y)=\begin{cases} a_{i,x}^{(e)}x+a_{i,y}^{(e)}y+b_{i}^{(e)} & [(x,y)\in\Omega^{(e)}] \\ 0 & \text{Otherwise} \end{cases} , \tag{2.35}$$

where $a_{i,x}^{(e)}$, $a_{i,y}^{(e)}$ and $b_{i}^{(e)}$ are the linear coefficients determined by the condition:

$$L_{(e;i)}(x_j,y_j)=\delta_{i,j}\ , \tag{2.36}$$

where $x_{(e;j)}$ and $y_{(e;j)}$ are the positions of the j-th node of the volume element e, and $\delta_{i,j}$ is the Kronecker's delta. Equation (2.35) is explicitly written as

$$\begin{pmatrix} a_{1,x}^{(e)} & a_{1,y}^{(e)} & b_{1}^{(e)} \\ a_{2,x}^{(e)} & a_{2,y}^{(e)} & b_{2}^{(e)} \\ a_{3,x}^{(e)} & a_{3,y}^{(e)} & b_{3}^{(e)} \end{pmatrix}\begin{pmatrix} x_{1}^{(e)} & x_{2}^{(e)} & x_{3}^{(e)} \\ y_{1}^{(e)} & y_{2}^{(e)} & y_{3}^{(e)} \\ 1 & 1 & 1 \end{pmatrix}=\begin{pmatrix} 1 & 0 & 0 \\ 0 & 1 & 0 \\ 0 & 0 & 1 \end{pmatrix} . \tag{2.37}$$

The coefficients $a_{i,x}^{(e)}$, $a_{i,y}^{(e)}$ and $b_{i}^{(e)}$ are obtained from the inverse of the matrix composed by $x_{i}^{(e)}$, $y_{i}^{(e)}$, and $z_{i}^{(e)}$.

For the 3D case, tetrahedral structures with four nodes are usually adopted as the geometry of the volume elements, and the nodal basis are written as

$$L_{(e;i)}(x,y,z)=\begin{cases} a_{i,x}^{(e)}x+a_{i,y}^{(e)}y+a_{i,z}^{(e)}z+b_{i}^{(e)} & [(x,y,z)\in\Omega^{(e)}] \\ 0 & \text{Otherwise} \end{cases} . \tag{2.38}$$

In a similar manner to the 2D case, the coefficients $a_{i,x}^{(e)}$, $a_{i,y}^{(e)}$, and $a_{i,z}^{(e)}$ are determined by

$$L_{(e;i)}[x_{(e;j)},y_{(e;j)},z_{(e;j)}]=\delta_{i,j}\ . \tag{2.39}$$

The nodal basis is suitable to calculate scalar fields. In the conventional FEM formalism, scalar or vector fields are assigned at the nodes of the volume elements (node elements).

For transverse vector fields, however, a higher accuracy can be obtained if the fields are assigned at the edges of the volume elements (edge elements) [8, 7]. The vector fields are expressed by the edge-element basis $\mathbf{W}_{(e;ij)}(\boldsymbol{r})$ defined as

$$\boldsymbol{W}_{(e;ij)}(\boldsymbol{r}) = \frac{1}{l_{ij}} \left[L_{(e;i)}(\boldsymbol{r})\nabla L_{(e;j)}(\boldsymbol{r}) - L_{(e;j)}(\boldsymbol{r})\nabla L_{(e;i)}(\boldsymbol{r})\right] \ , \tag{2.40}$$

where l_{ij} is the length of the edge between nodes $(e;i)$ and $(e;j)$. The transverse vector fields can be approximated by a linear combination of basis functions as follows:

$$\tilde{\boldsymbol{E}}_{(e;ij)} = \sum_{e}\sum_{i\neq j} E_{(e;ij)}\boldsymbol{W}_{(e;ij)} \ , \tag{2.41}$$

The expansion coefficients $E_{(e;ij)}$ represent field amplitudes at specific points:

$$E_{(e;ij)} = \hat{t}_{(e;ij)} \cdot \boldsymbol{E}[\boldsymbol{r}_{(e;ij)}] \ , \tag{2.42}$$

where $\hat{t}_{(e;ij)}$ denotes a unit vector parallel to the edge between nodes $(e;i)$ and $(e;j)$.

Note that the edge-element basis $\mathbf{W}_{(e;ij)}(\mathbf{r})$ automatically satisfies the divergence-free condition $[\nabla \cdot \mathbf{W}_{(e;ij)} = 0]$ of transverse fields [7]. This feature is confirmed by taking the divergence of Eq. (2.41) as follows:

$$\begin{aligned} \nabla \cdot \left[\sum_{e}\sum_{i\neq j} E_{(e;ij)}\boldsymbol{W}_{(e;ij)}\right] &= \nabla \cdot \left[\sum_{e}\sum_{i\neq j} E_{(e;ij)} \left(L_{(e;i)}\nabla L_{(e;j)} - L_{(e;j)}\nabla L_{(e;i)}\right)\right] \\ &= \sum_{e}\sum_{i\neq j} E_{(e;ij)} \left(\nabla L_{(e;i)} \cdot \nabla L_{(e;j)} - \nabla L_{(e;j)} \cdot \nabla L_{(e;i)}\right) \\ &= 0 \ . \end{aligned} \tag{2.43}$$

Since the transverse character of $\tilde{\mathbf{E}}_{(e;ij)}$ is guaranteed, the edge elements avoid spurious solutions and provide more accurate transverse fields than those calculated using nodal elements. The schematic illustrations of the nodal basis and edge basis are depicted in Fig. 2.3.

2.4 Application to electromagnetic fields

In the previous section, we have described the general FEM to solve boundary-value problems. In this section, we focus on the Maxwell's equations which govern the electric and magnetic fields in dielectric media.

We consider the time-harmonic Maxwell's equations:

$$\begin{aligned} \text{div } \boldsymbol{E} =& 4\pi\rho \ , & (2.44) \\ \textbf{curl } \boldsymbol{E} =& \frac{i\omega}{c}\boldsymbol{H} \ , & (2.45) \\ \text{div } \boldsymbol{H} =& 0 \ , & (2.46) \\ \textbf{curl } \boldsymbol{H} =& -\frac{i\omega\varepsilon}{c}\boldsymbol{E} + \frac{4\pi}{c}\boldsymbol{j} \ , & (2.47) \end{aligned}$$

where $\boldsymbol{E}$ and $\boldsymbol{H}$ are the electric and magnetic fields, respectively, ρ is the macroscopic charge and $\boldsymbol{j}$ is the current density. From Eqs. (2.44) and (2.45) with $\boldsymbol{j} = 0, \rho = 0$, we get the Maxwell's wave equation:

$$\textbf{curl curl } \boldsymbol{E} - \varepsilon k_0^2 \boldsymbol{E} = 0 \ . \tag{2.48}$$

2.4.1 One-dimensional case

As a typical 1D case, we consider the light reflection by the film layer with the thickness of L. We take xy plane parallel to the film surface, and an x-polarized incident light is illuminated to the z direction. The illustration of this problem is depicted in Fig. 2.4. In this situation, the electric field is treated as scalar, and Eq. (2.48) is written as

$$\left[\frac{\partial^2}{\partial z^2} + \varepsilon(z)k^2\right] E_x(z) = 0 \ , \tag{2.49}$$

where $\varepsilon(z)$ is the relative permittivity at z, k is the wave number in the background media. Comparing the above equation with Eq. (2.1), we get

$$\hat{\mathcal{L}} = \frac{\partial}{\partial x^2} + k^2 \ . \tag{2.50}$$

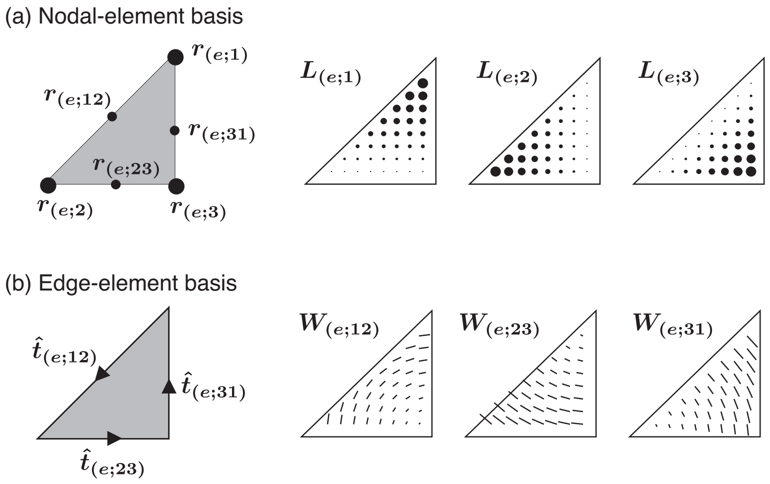

Figure 2.3: Schematic illustrations of the (a) nodal-element basis $L_{(e;i)}(\mathbf{r})$ and (b) edge-element basis $\mathbf{W}_{(e;ij)}(\mathbf{r})$.

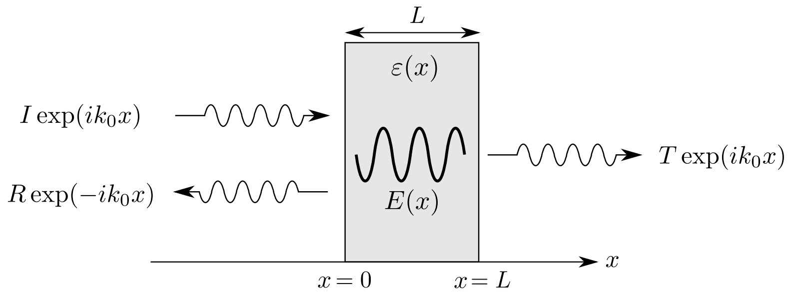

Figure 2.4: Schematic illustrations of the one-dimensional (thin-film) model

Substituting this $\hat{\mathcal{L}}$ into Eq. (2.22), the weak-form functional can be written as

$$\begin{aligned}\mathcal{F}[E_x] &= \int_0^L \mathrm{d}z\ E_x^* \left[\frac{\partial^2}{\partial^2 z} + \varepsilon(z)k^2\right] E_x \\ &= -\frac{1}{2}\int_0^L \mathrm{d}x\ \left\|\frac{\partial E_x}{\partial z}\right\|^2 - \varepsilon(z)k^2 \left\|E_x\right\|^2 + \frac{1}{2}\left[E_x^* \left(\frac{\partial E_x}{\partial z}\right)\right]_0^L \ . \qquad (2.51)\end{aligned}$$

The last term of RHS, which is originated from the partial integration, provides a Neumann type boundary condition.

As shown in Fig. 2.4, the electric field outside of the film is given by

$$E_x(z) = \begin{cases} I\exp(ikz) + R\exp(-ikz) & z < 0 \\ T\exp(ikz) & z > L \end{cases} , \qquad (2.52)$$

where I, R and T are the amplitudes of the incident, reflection and transition fields, respectively. The Maxwell's boundary conditions (MBCs) are written as

$$E_x(0) = I + R \ , \qquad (2.53)$$

$$\frac{\partial}{\partial z}E_x(0) = ikI - ikR \ , \qquad (2.54)$$

$$E_x(L) = T\exp(ikL) \ , \qquad (2.55)$$

$$\frac{\partial}{\partial z}E_x(L) = ikT\exp(ikL) \ . \qquad (2.56)$$

These conditions lead to the Neumann-type boundary conditions:

$$\frac{\partial}{\partial z}E_x(0) = -ikE_x(0) + 2ikI \ , \qquad (2.57)$$

$$\frac{\partial}{\partial z}E_x(L) = ikE_x(L) \ . \qquad (2.58)$$

Substituting Eqs. (2.57) and (2.58) into Eq. (2.51), we get

$$\begin{aligned}\mathcal{F}[E_z] =& -\frac{1}{2}\int_a^b \mathrm{d}x \, \left|\frac{\partial E_z}{\partial x}\right|^2 - k^2\|E_z\|^2 \\ &+ \frac{1}{2}E_x(L)^* ikE_x(L) - \frac{1}{2}E_x(0^* \left(-ikE_x(0) + 2ikI\right) \qquad (2.59)\end{aligned}$$

The obtained functional contains the boundary conditions implicitly.

2.4.2 Two-dimensional case

The EM-field scattering from Dielectric media with a column structure is governed by a 2D Maxwell's equations. We take xy plane parallel to the column axis, and an x-polarized incident light is illuminated to the z direction. In a similar manner to the 1D case, the electric field is treated as scalar and the Maxwell's wave equation is written as

$$\Delta E_z + \varepsilon(x,y)k^2 E_z = 0 \qquad (x,y) \in \Omega \qquad (2.60)$$

where Ω denotes the entire domain. The corresponding operator $\hat{\mathcal{L}}$ is given by

$$\hat{\mathcal{L}} = \Delta + \varepsilon(x,y)k^2 \ , \qquad (2.61)$$

and the weak-form functional is obtained as

$$\begin{aligned}\mathcal{F}[E_z] =& -\frac{1}{2}\iint_\Omega \mathrm{d}x\mathrm{d}y \; E_z^*(x,y)\left(\Delta + \varepsilon(x,y){k_0}^2\right)(x,y)E_z \\ =& -\frac{1}{2}\iint_\Omega \mathrm{d}x\mathrm{d}y \; \left(\nabla E_z(x,y)\right)^* \left(\nabla E_z(x,y)\right) + \varepsilon(x,y)k^2 E_z^*(x,y)E_z(x,y) \\ &+ \frac{1}{2}\oint_{\partial\Omega} \mathrm{d}s \; {E_z}^*(x,y)\left(\hat{n}\cdot \mathbf{grad}\; E_z(x,y)\right) \ , \qquad (2.62)\end{aligned}$$

where $\partial\Omega$ denotes the pathway around the Ω.

2.4.3 Three dimensional case

In the previous section, the electric field for the 1D and 2D cases can be treated as scalar because the electric field of the incident light is parallel to the dielectric surface. Here, we consider the general 3D case that electric fields should be treated as vector fields. The time-harmonic Maxwell's wave equation is written as

$$\left(\mathbf{curl}\,\mathbf{curl} - k^2\right) E_z(x) = 0 \ , \tag{2.63}$$

and the operator $\hat{\mathcal{L}}$ is given by $\hat{\mathcal{L}} = \mathbf{curl}\,\mathbf{curl} - \varepsilon(\boldsymbol{r})k^2$. Thus, the weak-form functional is obtained as

$$\begin{aligned}\mathcal{F}[\boldsymbol{E}] =& -\frac{1}{2}\iiint \mathrm{d}x\ \boldsymbol{E}^*(\boldsymbol{r})\left(\mathbf{curl}\,\mathbf{curl} - \varepsilon(\boldsymbol{r})k^2\right)\boldsymbol{E}(\boldsymbol{r}) \\ =& -\frac{1}{2}\iiint_\Omega \mathrm{d}\boldsymbol{r}\ \boldsymbol{E}^*(\boldsymbol{r})\left(\mathbf{curl}\ \boldsymbol{E}(\boldsymbol{r})^*\right)\cdot\left(\mathbf{curl}\ \boldsymbol{E}(\boldsymbol{r})\right) - \varepsilon(\boldsymbol{r})k^2\boldsymbol{E}(\boldsymbol{r})^*\boldsymbol{E}(\boldsymbol{r}) \\ &+\frac{1}{2}\iint_{\partial\Omega} \mathrm{d}\boldsymbol{r}\ \boldsymbol{E}^*(\boldsymbol{r})\cdot\left(\hat{n}\times\mathbf{curl}\ \boldsymbol{E}(\boldsymbol{r})\right) \ ,\end{aligned} \tag{2.64}$$

where we have used the relation

$$\mathrm{div}\ \boldsymbol{a}\times\boldsymbol{b} = (\mathbf{curl}\ \boldsymbol{a})\cdot\boldsymbol{b} - \boldsymbol{a}\cdot(\mathbf{curl}\ \boldsymbol{b}) \ . \tag{2.65}$$

Chapter 3

Finite element method including exciton effect

This chapter gives an overview of an new electromagnetic (EM) simulation method based on a finite-element method (FEM) for an exciton confined to a semiconductor nanostructure. The EM field inside the semiconductor excites two transverse exciton polariton and a single longitudinal exciton at a given frequency. Established EM simulation methods cannot be applied directly to semiconductor nanostructures because of this multimode excitation; however, the present method overcomes this difficulty by introducing an additional boundary condition. To avoid spurious solutions and enhance the precision, we propose a hybrid edgenodal element formulation in which edge and nodal elements are employed to represent the transverse and longitudinal polarizations, respectively. We apply the developed method to the EM-field scattering and distributions of exciton polarizations of spherical and hexagonal-disk quantum dots.

3.1 Exciton polariton

3.1.1 Linear response theory

For dielectric media, a dielectric function is represented by a local form $\varepsilon(\boldsymbol{r})$ while the dielectric function $\varepsilon(\boldsymbol{r}, \boldsymbol{r}')$ has non-locality, *i.e.*, an excitation position is apart from a response position for exciton active media. In this exciton active media, the exciton polarization $\boldsymbol{P}(\boldsymbol{r})$ is represented by

$$\boldsymbol{P}(\boldsymbol{r}) = \int \mathrm{d}\boldsymbol{r}' \, \chi(\boldsymbol{r}, \boldsymbol{r}'; \omega) \boldsymbol{E}(\boldsymbol{r}') \;, \tag{3.1}$$

where $\chi(\boldsymbol{r}, \boldsymbol{r}'; \omega)$ is the nonlocal susceptibility tensor. Let us derive the expression of the nonlocal susceptibility. In general, the Hamiltonian of a matter interacting with external light field is given by

$$\hat{\mathcal{H}} = \hat{\mathcal{H}}_0 + \hat{\mathcal{H}}^{(\mathrm{ext})} \;, \tag{3.2}$$

where $\hat{\mathcal{H}}_0$ denotes the no-perturbing matter Hamiltonian, and $\hat{\mathcal{H}}_{\mathrm{ex}}$ denotes the interaction of exciton and external electric field. The Hamiltonian $\hat{\mathcal{H}}_I(t)$ in the interaction picture is represented as

$$\hat{\mathcal{H}}_I(t) = \hat{\mathcal{H}}_0 + \hat{\mathcal{H}}_I^{(\mathrm{ext})}(t) \;, \tag{3.3}$$

where $\hat{\mathcal{H}}_I^{(\mathrm{ext})}(t)$ in the interaction picture is given by

$$\hat{\mathcal{H}}_I^{(\mathrm{ext})} = \exp\left(i \frac{\hat{\mathcal{H}}_0 t}{\hbar} \right) \hat{\mathcal{H}}^{\mathrm{ext}} \exp\left(-i \frac{\hat{\mathcal{H}}_0 t}{\hbar} \right) \;. \tag{3.4}$$

In the interaction picture, a matter state $|\Psi_I(t)\rangle$ is represented as

$$|\Psi_I(t)\rangle = \exp\left(i \frac{\hat{\mathcal{H}}_0 t}{\hbar} \right) |\Psi(t)\rangle \;, \tag{3.5}$$

where $|\Psi(t)\rangle$ is a matter state in the Schrödinger picture.

We introduce the density matrix given by

$$\hat{\rho}(t) = |\Psi_I(t)\rangle \langle \Psi_I(t)| \;. \tag{3.6}$$

The dense matrix consists of the non-perturbative term $\hat{\rho}_0 = |\Psi_0\rangle \langle \Psi_0|$ with $|\Psi_0\rangle$ being the ground state of $\hat{\mathcal{H}}_0$ and perturbative term $\hat{\rho}'(t)$:

$$\hat{\rho}(t) = \hat{\rho}_0 + \hat{\rho}'(t) \;. \tag{3.7}$$

The time evolution of the $\hat{\rho}'(t)$ is governed by the Von Neumann equation:

$$\frac{\partial \hat{\rho}'}{\partial t} = \frac{1}{i\hbar}[\hat{\mathcal{H}}_I^{(\mathrm{ext})}(t), \hat{\rho}(t)] \ . \tag{3.8}$$

By integrating over time t, we have

$$\hat{\rho}'(t) = \frac{1}{i\hbar}\int_{-\infty}^{t} \mathrm{d}t_1 \ [\hat{\mathcal{H}}_I^{(\mathrm{ext})}(t_1), \hat{\rho}_0 + \hat{\rho}'(t_1)] \ . \tag{3.9}$$

Substituting the above equation into $\hat{\rho}'(t_1)$ in the RHS, we get

$$\begin{aligned}\hat{\rho}'(t) =& \frac{1}{i\hbar}\int_{-\infty}^{t} \mathrm{d}t_1 \ [\hat{\mathcal{H}}_I^{(\mathrm{ext})}(t_1), \hat{\rho}_0] \\ &+ \frac{1}{(i\hbar)^2}\int_{-\infty}^{t} \mathrm{d}t_1 \ \int_{-\infty}^{t_1} \mathrm{d}t_2 [\hat{\mathcal{H}}_I^{(\mathrm{ext})}(t_1), [\hat{\mathcal{H}}_I^{(\mathrm{ext})}(t_2), \hat{\rho}_0]] \\ &+ \frac{1}{(i\hbar)^3}\int_{-\infty}^{t} \mathrm{d}t_1 \ \int_{-\infty}^{t_1} \mathrm{d}t_2 \int_{-\infty}^{t_2} \mathrm{d}t_3 [\hat{\mathcal{H}}_I^{(\mathrm{ext})}(t_1), [\hat{\mathcal{H}}_I^{(\mathrm{ext})}(t_2), [\hat{\mathcal{H}}_I^{(\mathrm{ext})}(t_3), \hat{\rho}_0]]] \\ &+ \cdots \ . \end{aligned} \tag{3.10}$$

The first term in the RHS provides a linear response, and the higher-order terms lead to non-linear effects, such as a second harmonic generation and four-wave mixing. We neglect the higher-order terms, and thus $\hat{\rho}'(t)$ is approximated as

$$\hat{\rho}'(t) \approx \frac{1}{i\hbar}\int_{-\infty}^{t} \mathrm{d}t_1 \ [\hat{\mathcal{H}}_I^{(\mathrm{ext})}(t_1), \hat{\rho}_0] \ . \tag{3.11}$$

Expectation values of an operator $\hat{\mathcal{O}}$ is given by

$$\langle \hat{\mathcal{O}}(t) \rangle = \mathrm{Tr}\left[\hat{\mathcal{O}}_{\mathrm{I}}(t)\rho\hat{(t)}\right] \ . \tag{3.12}$$

From Eq. (3.10), this equation can be written as

$$\begin{aligned}\langle\delta\hat{\mathcal{O}}(t)\rangle =&\mathrm{Tr}\left[\hat{\mathcal{O}}_{\mathrm{I}}(t)\hat{\rho}(t)]\right] - \mathrm{Tr}\left[\hat{\mathcal{O}}_{\mathrm{I}}(t)\hat{\rho}_0\right] &(3.13)\\ =&\mathrm{Tr}\left[\hat{\mathcal{O}}_{\mathrm{I}}(t)\hat{\rho}'(t)\right] &(3.14)\\ =&\frac{1}{i\hbar}\int_{-\infty}^{t}\mathrm{d}t_1\ \mathrm{Tr}\left\{\hat{\mathcal{O}}_{\mathrm{I}}(t)[\hat{\mathcal{H}}_I^{(\mathrm{ext})}(t_1),\hat{\rho}_0]\right\}\ . &(3.15)\end{aligned}$$

Note that the trace is invariant under cyclic permutations:

$$\begin{aligned}\mathrm{Tr}\left\{\hat{\mathcal{O}}_{\mathrm{I}}(t)[\hat{\mathcal{H}}_I^{(\mathrm{ext})}(t_1),\hat{\rho}_0]\right\} =&\mathrm{Tr}\left[\hat{\mathcal{O}}_{\mathrm{I}}(t)\hat{\mathcal{H}}_I^{(\mathrm{ext})}(t_1)\hat{\rho}_0 - \hat{\mathcal{O}}_{\mathrm{I}}(t)\hat{\rho}_0\hat{\mathcal{H}}_I^{(\mathrm{ext})}(t_1)\right]\\ &= \langle\hat{\mathcal{O}}_{\mathrm{I}}(t)[\hat{\mathcal{H}}_I^{(\mathrm{ext})}(t_1)]\rangle - \langle\hat{\mathcal{O}}_{\mathrm{I}}(t)[\hat{\mathcal{H}}_I^{(\mathrm{ext})}(t_1)]\rangle\ . \quad (3.16)\end{aligned}$$

Thus, we get

$$\langle\delta\hat{\mathcal{O}}(t)\rangle = \int_{-\infty}^{t}\mathrm{d}t_1\ \mathrm{Tr}\left\{\frac{1}{i\hbar}[\hat{\mathcal{O}}_{\mathrm{I}}(t),\hat{\mathcal{H}}_I^{(\mathrm{ext})}(t_1)]\rho_0\right\}\ . \quad (3.17)$$

3.1.2 Nonlocal susceptibility

By using the above formula, we derive the nonlocal susceptibility in a semiconductor originating from dispersive motion of an exciton. The interaction between exciton and an external electric field $\boldsymbol{E}(\boldsymbol{r})$ of light is considered as the perturbative term. The interaction Hamiltonian is written as

$$\hat{\mathcal{H}}^{(\mathrm{ext})}(t) = -\int \mathrm{d}\boldsymbol{r}\ \hat{\boldsymbol{P}}(\boldsymbol{r})\cdot\boldsymbol{E}(\boldsymbol{r},t)\ , \quad (3.18)$$

with

$$\hat{\boldsymbol{P}}(\boldsymbol{r}) =\sum_n \delta(\boldsymbol{r}-\boldsymbol{r}_n)\boldsymbol{r}q_n\ . \quad (3.19)$$

where $\hat{\boldsymbol{P}}$ is the polarization operator, and q_n and r_n are the charge and coordinate for the nth particle. For the interaction picture, it can be rewritten as $\hat{\boldsymbol{P}}_{\mathrm{I}}(t) = \exp(i\hat{\mathcal{H}}_0 t/\hbar)\hat{\boldsymbol{P}}\exp(-i\hat{\mathcal{H}}_0 t/\hbar)$.

Substituting Eq. (3.18) into Eq. (3.17), we get

$$\delta\boldsymbol{P}(\mathbf{r},t) = \int_{-\infty}^{t} \mathrm{d}t' \ \mathrm{Tr}\left(\frac{1}{i\hbar}\left[\hat{\boldsymbol{P}}_{\mathrm{I}}(\boldsymbol{r},t), \hat{\mathcal{H}}_{\mathrm{I}}^{(\mathrm{ext})}\right]\rho_0\right) \tag{3.20}$$

$$= \int_{\infty}^{t} \mathrm{d}t' \int \mathrm{d}\boldsymbol{r}' \left\langle \frac{1}{i\hbar}\left[\hat{\boldsymbol{P}}_{\mathrm{I}}(\boldsymbol{r},t), \hat{\boldsymbol{P}}_{\mathrm{I}}(\boldsymbol{r}',t')\right]\right\rangle . \tag{3.21}$$

From Eq. (3.21), the susceptibility takes the form

$$\begin{aligned}
\chi(\boldsymbol{r},\boldsymbol{r}';\boldsymbol{t},\boldsymbol{t}') =& \left\langle \frac{1}{i\hbar}\left[\hat{\boldsymbol{P}}_{\mathrm{I}}(\boldsymbol{r},t), \hat{\boldsymbol{P}}_{\mathrm{I}}(\boldsymbol{r}',t')\right]\right\rangle \\
=& \frac{1}{i\hbar}\left\langle\Psi_0\right| e^{i\hat{\mathcal{H}}_0 t/\hbar}\hat{\boldsymbol{P}}(\boldsymbol{r})e^{-i\hat{\mathcal{H}}_0 t/\hbar}\left(\sum_n \left|\Psi_n\right\rangle\left\langle\Psi_n\right|\right) e^{i\hat{\mathcal{H}}_0 t'/\hbar}\hat{\boldsymbol{P}}(\boldsymbol{r}')e^{-i\hat{\mathcal{H}}_0 t'/\hbar}\left|\Psi_0\right\rangle \\
&- \frac{1}{i\hbar}\left\langle\Psi_0\right| e^{i\hat{\mathcal{H}}_0 t'/\hbar}\hat{\boldsymbol{P}}(\boldsymbol{r}')e^{-i\hat{\mathcal{H}}_0 t'/\hbar}\left(\sum_n \left|\Psi_n\right\rangle\left\langle\Psi_n\right|\right) e^{i\hat{\mathcal{H}}_0 t/\hbar}\hat{\boldsymbol{P}}(\boldsymbol{r})e^{-i\hat{\mathcal{H}}_0 t/\hbar}\left|\Psi_0\right\rangle \\
=& \frac{1}{i\hbar}\sum_n \left\langle\Psi_0\right|\hat{\boldsymbol{P}}(\boldsymbol{r})\left|\Psi_n\right\rangle\left\langle\Psi_n\right|\hat{\boldsymbol{P}}(\boldsymbol{r}')\left|\Psi_0\right\rangle e^{i(E_n-E_0)t/\hbar} \\
&- \frac{1}{i\hbar}\sum_n \left\langle\Psi_0\right|\hat{\boldsymbol{P}}(\boldsymbol{r}')\left|\Psi_n\right\rangle\left\langle\Psi_n\right|\hat{\boldsymbol{P}}(\boldsymbol{r})\left|\Psi_0\right\rangle e^{-i(E_n-E_0)t/\hbar} ,
\end{aligned} \tag{3.22}$$

where Ψ_n is the nth excited state with the eigenenergy E_n. Because of the causality rule, we should introduce an additional term $\theta(t-t')$, which is expressed as

$$\theta(t-t') = \lim_{\gamma\to 0^+} -\frac{1}{2\pi i}\int_{-\infty}^{\infty}\mathrm{d}\omega' \ \frac{1}{\omega'+i\gamma}e^{-i\omega'(t-t')} . \tag{3.23}$$

Multiplying $\theta(t-t')$ by the first term of Eq. (3.28), we have

$$\begin{aligned}
&\frac{1}{i\hbar}\sum_n \left\langle\Psi_0\right|\hat{\boldsymbol{P}}(\boldsymbol{r})\left(\left|\Psi_n\right\rangle\left\langle\Psi_n\right|\right)\hat{\boldsymbol{P}}(\boldsymbol{r}')\left|\Psi_0\right\rangle e^{i(E_n-E_0)t/\hbar}\theta(t-t') \\
&= \lim_{\gamma\to 0^+} -\frac{1}{2\pi\hbar}\sum_n \int_{-\infty}^{\infty}\frac{\left\langle\Psi_0\right|\hat{\boldsymbol{P}}(\boldsymbol{r})\left(\left|\Psi_n\right\rangle\left\langle\Psi_n\right|\right)\hat{\boldsymbol{P}}(\boldsymbol{r}')\left|\Psi_0\right\rangle}{\omega'+i\gamma}e^{-i(\omega'+(E_n-E_0)/\hbar)t} \ \mathrm{d}\omega' \\
&= \lim_{\gamma\to 0^+} \frac{1}{2\pi}\sum_n \int_{-\infty}^{\infty}\frac{\left\langle\Psi_0\right|\hat{\boldsymbol{P}}(\boldsymbol{r})\left|\Psi_n\right\rangle\left\langle\Psi_n\right|\hat{\boldsymbol{P}}(\boldsymbol{r}')\left|\Psi_0\right\rangle}{\hbar\omega-(E_n-E_0)+i\hbar\gamma}e^{-i\omega t} \ \mathrm{d}\omega .
\end{aligned} \tag{3.24}$$

Therefore, the Fourier component of χ take the form

$$\chi(r, r'; \omega) = \sum_n \frac{\langle\Psi_0| \hat{\boldsymbol{P}}(\boldsymbol{r}) |\Psi_n\rangle \langle\Psi_n| \hat{\boldsymbol{P}}(\boldsymbol{r}') |\Psi_0\rangle}{(E_n - E_0) - \hbar\omega - i\hbar\gamma} \; . \tag{3.25}$$

3.1.3 Exciton polariton

In the case of the bulk semiconductor, the center-of-mass motion of the exciton is approximately represented by a plain wave [2], and the matrix element of the polarization operator is given by

$$\langle\Psi_0| \hat{\boldsymbol{P}}(\boldsymbol{r}) |\Psi_k\rangle = \frac{\boldsymbol{\mu}}{\sqrt{V}} \exp(i\boldsymbol{k} \cdot \boldsymbol{r}) \; , \tag{3.26}$$

where Ψ_k denotes the eigenstate with the wave vector $\boldsymbol{k}$, V is the volume of the bulk crystal, μ is the intensity of the induced polarization given as $\boldsymbol{\mu}^2 = \varepsilon_{\mathrm{bg}}\Delta_{\mathrm{LT}}/(4\pi)$, Δ_{LT} is the longitudinal–transverse splitting energy, and $\varepsilon_{\mathrm{bg}}$ is the background dielectric constant. Assuming the valence and conduction bands are parabolic with an effective mass of M, the excitation eigenenergy $E_k - E_0$ is approximated to be

$$E_{\boldsymbol{k}} - E_0 = E_{\mathrm{G}} + (\hbar^2/2M)\boldsymbol{k}^2 \; , \tag{3.27}$$

where E_{G} are the excitation energy at a band edge. Substituting Eqs. (3.26) and (3.27) into Eq. (3.25), The susceptibility tensor of the exciton-active media can be written as

$$\chi(\boldsymbol{r}, \boldsymbol{r}'; \omega) = \sum_{\boldsymbol{k}} \left(\frac{1}{4\pi} \frac{\varepsilon_{\mathrm{bg}}\Delta_{\mathrm{LT}}}{E_{\mathrm{G}} + (\hbar^2/2M)k^2 - \hbar\omega - i\hbar\gamma} \right) e^{i\boldsymbol{k}\cdot(\boldsymbol{r}-\boldsymbol{r}')} \tag{3.28}$$

For the reciprocal space, the above can be rewritten as

$$\chi(\boldsymbol{k}, \omega) = \frac{1}{4\pi} \frac{\varepsilon_{\mathrm{bg}}\Delta_{\mathrm{LT}}}{E_{\mathrm{G}} + (\hbar^2/2M)k^2 - \hbar\omega - i\hbar\gamma} \tag{3.29}$$

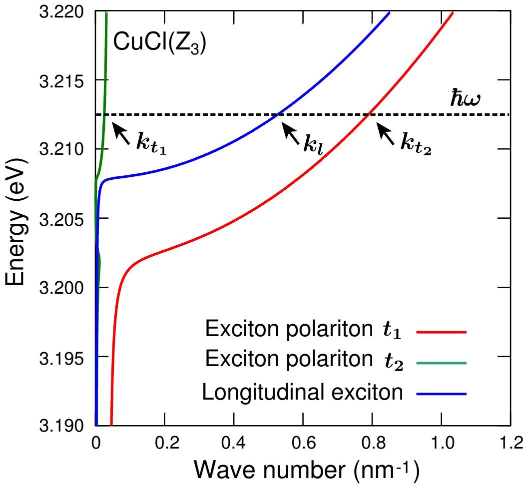

Figure 3.1: Dispersion curve of the transverse polariton and longitudinal exciton modes of the bulk CuCl. The parameter is depicted on Table 3.1

Table 3.1: Parameters of the Z_3 exciton of CuCl and $\Gamma_5(B)$ exciton of ZnO; m_e denotes the free electron mass.

QD	$\varepsilon_{\rm bg}$	M (units of m_e)	$E_{\rm G}$ (eV)	$\Delta_{\rm LT}$ (meV)
CuCl (Z_3) [9]	5.56	2.3	3.2022	5.65
ZnO [Γ_5 (B)] [19, 35]	8.86	0.97	3.3856	5.00

The dielectric function can be written as

$$\begin{aligned}\varepsilon(k,\omega) =&\varepsilon_{\rm bg} + 4\pi\chi(k,\omega)\\ =&\varepsilon_{\rm bg} + \frac{\varepsilon_{\rm bg}\Delta_{\rm LT}}{E_{\rm G} + (\hbar^2/2M)k^2 - \hbar\omega - i\hbar\gamma}\ .\end{aligned} \tag{3.30}$$

The k-dependence of the dielectric function in Eq. (3.30) comes from the kinetic energy of the exciton, which is responsible for the size quantization effect in the spectral peaks of semiconductor nanostructures. An interaction between a light and exciton produces the transverse modes, called the exciton polariton. The dispersion relations of the exciton polaritons in a bulk semiconductor are obtained from

$$\mathbf{k}^2 = \left(\frac{\omega}{c}\right)^2 \varepsilon(\mathbf{k},\omega)\ . \tag{3.31}$$

Substituting Eq.(3.30) into Eq.(3.31), this dispersion relation take the form

$$A(\omega)k^4 + B(\omega)k^2 + C(\omega) = 0 \tag{3.32}$$

with

$$\begin{aligned}A(\omega) =&\frac{\hbar^2}{2M}\\ B(\omega) =&E_{\rm G} - \hbar\omega\left(1 + \frac{\hbar\omega}{2Mc^2}\right) - i\hbar\gamma\\ C(\omega) =&\frac{\omega^2}{c^2}\left(E_{\rm G} - \hbar\omega - i\hbar\gamma + \varepsilon_{bg}\Delta_{\rm LT}\right)\ .\end{aligned}$$

Eq. (3.32) has four complex solutions, moreover the two of them k_{t1}, k_{t2} which have positive imaginary, are physically meaningful.

In addition to two transverse exciton polaritons, one longitudinal exciton mode appears whose dispersion is obtained from $\varepsilon(k_l,\omega) = 0$ with k_l being the wave vector of the longitudinal mode.

$$P(\omega)k^2 + Q(\omega) = 0 \tag{3.33}$$

with

$$
\begin{aligned}
P(\omega) =& \frac{\hbar^2}{2M} \\
Q(\omega) =& E_{\mathrm{G}} - \Delta_{\mathrm{LT}} - \hbar\omega - i\hbar\gamma \ .
\end{aligned}
$$

The Eq.(3.33) also has two complex roots. The dispersions of two exciton polariton modes and a longitudinal exciton mode are shown in Fig. 3.1. In such media, there are three propagating modes with the different wavenumber $\mathbf{k}_{t1}, \mathbf{k}_{t2}$ and $\mathbf{k}_l$ at a given frequency.

The electric fields $\mathbf{E}^{(t_1)}$ and $\mathbf{E}^{(t_2)}$ accompanied by two transverse modes are governed by wave equations:

$$
\begin{aligned}
\nabla \times \nabla \times \mathbf{E}^{(t_1)} - k_{t_1}^2 \mathbf{E}^{(t_1)} &= 0 &(3.34)\\
\nabla \times \nabla \times \mathbf{E}^{(t_2)} - k_{t_2}^2 \mathbf{E}^{(t_2)} &= 0 &(3.35)\\
\nabla^2 \Phi + k_l^2 \Phi &= 0 \ , &(3.36)
\end{aligned}
$$

and the scalar potential Φ providing the longitudinal field $\mathbf{E}^{(l)} = -\nabla\Phi$ satisfied the Poisson's equation.

3.1.4 Additional boundary condition

Let us consider the nanostructure consisting of the semiconducting and the classical dielectric media. [See Fig. 3.2] At the interface between two media, the following Maxwell's boundary conditions (MBC) are satisfied:

$$
\begin{aligned}
\mathbf{E}^{(0)} &= \mathbf{E}^{(1)} &(3.37)\\
\hat{n} \times \nabla \times \mathbf{E}^{(0)} &= \hat{n} \times \nabla \times \mathbf{E}^{(1)} \ , &(3.38)
\end{aligned}
$$

where $\mathbf{E}^{(1)} = \mathbf{E}^{(t_1)} + \mathbf{E}^{(t_2)} - \nabla\Phi$ is the total electric field in the semiconducting media.

When the material is dielectric or metal, the number of the wave mode is just one. Therefore, the EM field is uniquely determined by imposing only the MBCs. For semiconductor, however, there are three wave modes, *i.e.*, two transverse exciton polaritons and one longitudinal exciton. Therefore, three more boundary conditions are necessary to uniquely determine the EM fields. Several types of this additional boundary conditions (ABCs) have been considered [22, 13]. Here, we use the Pekar type ABC where exciton polarization $\mathbf{P}(\mathbf{r})$ vanishes at the interface of the semiconductor. Since the polarization is given by $\mathbf{P} = \chi(k,\omega)\mathbf{E}$ in terms of a susceptibility $\chi(k,\omega)$, the Pekar type ABC is expressed as

$$\chi(k_{t_1},\omega)\mathbf{E}^{(t_1)} + \chi(k_{t_2},\omega)\mathbf{E}^{(t_2)} + \chi(k_l,\omega)(-\nabla\Phi) = 0 \tag{3.39}$$

with

$$\chi(k,\omega) = \frac{1}{4\pi}\left(\varepsilon(k,\omega) - 1\right) \ . \tag{3.40}$$

The EM field and polarization field is obtained from the variational problem of $\delta\mathcal{F} = 0$ under the constraint of Eq.(3.39).

3.2 One-dimensional case

3.2.1 Finite element analysis

Here, we calculate the transmission and the reflection coefficients of the semiconducting quantum well (QW) by using the one-dimensional FEM. The established model is depicted in Fig. 3.2, where the z-polarized light incident upon the QW of the thickness L. When the polarization of the electric field is parallel to the surface (s-polarized light), only two transverse-polariton modes are excited and the contributions from the longitudinal mode is negligible. Thus the governing equation of the polariton modes are expressed as

$$\frac{\partial^2 E_z^{(t1)}}{\partial x^2} + k_1^2 E_z^{(t1)} = 0 \tag{3.41}$$

$$\frac{\partial^2 E_z^{(t2)}}{\partial x^2} + k_1^2 E_z^{(t2)} = 0 \ , \tag{3.42}$$

where $E_z^{(t1)}$ and $E_z^{(t2)}$ denote the electric field of the polaritons at the wavenumber k_{t1} and k_{t2}, respectively. Similar manner to Eq. (2.51), the weak-form functional can be written as

$$\mathcal{F}[\boldsymbol{E}_z^{(t1)}, \boldsymbol{E}_z^{(t2)}] = -\frac{1}{2}\sum_\alpha \int_0^L \left(\frac{\partial E_z^{(t\alpha)}}{\partial x}\right)^* \left(\frac{\partial E_z^{(t\alpha)}}{\partial x}\right) - k_{t\alpha}^2 E_z^{(t\alpha)*} E_z^{(t\alpha)}\,\mathrm{d}x$$
$$+\frac{1}{2}\sum_\alpha \left[E_z^{(t\alpha)*}\frac{\partial E_z^{(t\alpha)}}{\partial x}\right]_0^L . \tag{3.43}$$

The total electric and polarization field amplitude inside the media are given as

$$\sum_\alpha E_z^{(t\alpha)}(x) , \tag{3.44}$$

and

$$\sum_\alpha \chi(k_{t\alpha}, \omega) E_z^{(t\alpha)}(x) . \tag{3.45}$$

At the two ends ($x = 0, L$), the MBCs (2.57) and (2.58) are expressed as

$$\begin{cases} \sum_\alpha E_z^{(t\alpha)}(0) & = I + R \\ \frac{\partial}{\partial x}\sum_\alpha E_z^{(t\alpha)}(0) & = ik_0(I - R) \end{cases} , \tag{3.46}$$

and

$$\begin{cases} \sum_\alpha E_z^{(t\alpha)}(L) & = T \\ \frac{\partial}{\partial x}\sum_\alpha E_z^{(t\alpha)}(L) & = ik_0 T \end{cases} . \tag{3.47}$$

Similar manner to Eqs. (2.57)–(2.58), the Eqs. (3.46)- (3.47) can be reduced to:

$$\frac{\partial}{\partial x}\sum_\alpha E_z^{(t\alpha)}(0) = -\,ik_0 \sum_\alpha E_z^{(t\alpha)}(0) + 2ik_0 I \tag{3.48}$$
$$\frac{\partial}{\partial x}\sum_\alpha E_z^{(t\alpha)}(L) = ik_0 \sum_\alpha E_z^{(t\alpha)}(L) . \tag{3.49}$$

Thus our problem is solving $\delta\mathcal{F} = 0$ under Eqs. (3.49)–(3.49).

Next, let we consider the discretization by FEM. As shown in the chapter 2, the electric field is approximated to be the linear combination of the basis function:

$$\tilde{E}_z^{(t\alpha)} = \sum_e \sum_{i=1,2} E_{s(e;i)}^{(t\alpha)} L_{(e;i)}(x) \ , \tag{3.50}$$

where e is the index of the element, i is the local index of the node, the abbreviation $s(e;i)$ stands for the global index of a node corresponding to the local index (e,i). The $E_{s(e;i)}^{(t\alpha)}$ denote the expansion coefficients and $L_{(e;i)}(x)$ denote the one-dimensional nodal basis defined in Eq. (2.34).

Substituting Eq. (3.50) into Eq. (3.50), we get

$$\begin{aligned} F[E_{z;s(e;i)}^{(t\alpha)}] = & -\frac{1}{2} \sum_\alpha \sum_e \sum_{i,j} K_{ij}^{(e)}(k_{t\alpha}) E_{s(e;i)}^{(t\alpha)*} E_{s(e;j)}^{(t\alpha)} \\ & + \frac{1}{2} \sum_\alpha \left(E_N^{(t\alpha)*} \frac{\partial \tilde{E}(L)}{\partial x} - E_0^{(t\alpha)*} \frac{\partial \tilde{E}(0)}{\partial x} \right) \end{aligned} \tag{3.51}$$

with

$$K_{ij}^{(e)}(k_{t\alpha}) = \sum_\alpha \int_0^L \left(\frac{\partial L_{(e;i)}}{\partial x} \right)^* \left(\frac{\partial L_{(e;j)}}{\partial x} \right) - k_{t\alpha}^2 L_{(e;i)} L_{(e;j)} \ \mathrm{d}x \tag{3.52}$$

According to the Ritz method, the solution is obtained from

$$\frac{\partial F}{\partial E_n^{(t\alpha)*}} = 0 \ . \tag{3.53}$$

From Eq. (3.51), the above derivative can be written as

$$\frac{\partial F}{\partial E_n^{(t\alpha)*}} = \begin{cases} -\frac{1}{2}\left(K_{t\alpha;11}^{(1)} E_0 + K_{t\alpha;12}^{(1)} E_1 \right) - \frac{1}{2} \frac{\partial E^{(t\alpha)}(0)}{\partial x} & n = 1 \\ -\frac{1}{2}\left(K_{t\alpha;11}^{(N)} E_{N-1} + K_{t\alpha;12}^{(N)} E_N \right) + \frac{1}{2} \frac{\partial E^{(t\alpha)}(L)}{\partial x} & n = N \\ -\frac{1}{2}\left(K_{t\alpha;21}^{(n)} E_{n-1} + (K_{t\alpha;22}^{(n-1)} + K_{t\alpha;11}^{(n)}) E_n + K_{t\alpha;12}^{(n)} E_{n+1} \right) & \text{otherwise} \end{cases} . \tag{3.54}$$

The condition (3.53) leads the system of equations, which is also called as the finite element matrix:

$$\begin{pmatrix} K^{(1)}_{t_1;11} & K^{(1)}_{t_1;12} & 0 & \cdots & 0 \\ K^{(1)}_{t_1;12} & K^{(1)}_{t_1;22}+K^{(2)}_{t_1;11} & K^{(2)}_{t_1;12} & & \\ 0 & K^{(2)}_{t_1;12} & K^{(2)}_{t_1;22}+K^{(3)}_{t_1;11} & & \\ \vdots & & & \ddots & \\ 0 & & & & K^{(N)}_{t_1;22} \end{pmatrix} \begin{pmatrix} E^{(t_1)}_0 \\ E^{(t_1)}_1 \\ E^{(t_1)}_2 \\ \vdots \\ E^{(t_1)}_N \end{pmatrix} = \begin{pmatrix} -\partial E^{(t_1)}(0)/\partial x \\ 0 \\ 0 \\ \vdots \\ \partial E^{(t_1)}(L)/\partial x \end{pmatrix} \tag{3.55}$$

$$\begin{pmatrix} K^{(1)}_{t_2;11} & K^{(1)}_{t_2;12} & 0 & \cdots & 0 \\ K^{(1)}_{t_2;12} & K^{(1)}_{t_2;22}+K^{(2)}_{t_2;11} & K^{(2)}_{t_2;12} & & \\ 0 & K^{(2)}_{t_2;12} & K^{(2)}_{t_2;22}+K^{(3)}_{t_2;11} & & \\ \vdots & & & \ddots & \\ 0 & & & & K^{(N)}_{t_2;22} \end{pmatrix} \begin{pmatrix} E^{(t_2)}_0 \\ E^{(t_2)}_1 \\ E^{(t_2)}_2 \\ \vdots \\ E^{(t_2)}_N \end{pmatrix} = \begin{pmatrix} -\partial E^{(t_2)}(0)/\partial x \\ 0 \\ 0 \\ \vdots \\ \partial E^{(t_2)}(L)/\partial x \end{pmatrix} , \tag{3.56}$$

At the ends $n = 0, N$, the above equation incorporates a derivative term $\partial E^{(t\alpha)}/\partial x$, which also appears in the MBCs. However, the MBCs (3.46)–(3.47) are defined for the total electric field $E^{(t1)} + E^{(t2)}$. Therefore, we use another condition for both ends ($n = 0, N$):

$$\sum_\alpha \frac{\partial F}{\partial E^{(t\alpha)*}_n} = 0 \, . \tag{3.57}$$

At the left end ($n = 0$), Eq. (3.57) is expressed as

$$\begin{aligned} 0 =& \sum_\alpha \frac{\partial F}{\partial E^{(t\alpha)*}_0} \\ =& -\frac{1}{2}\sum_\alpha \left(K^{(1)}_{t\alpha;11}E_0 + K^{(1)}_{t\alpha;12}E_1\right) - \frac{1}{2}\sum_\alpha \frac{\partial E^{(t1)}(0)}{\partial x} \\ =& -\frac{1}{2}\sum_\alpha \left(K^{(1)}_{t\alpha;11}E_0 + K^{(1)}_{t\alpha;12}E_1\right) - \frac{1}{2}\left(-ik_0 \sum_\alpha E^{(t\alpha)}_z(0) + 2ik_0 I\right) \, . \end{aligned} \tag{3.58}$$

In above, we substitute Eq. (3.46) into the second term.

In similar, at the right end ($n = N$), we have

$$0 = -\frac{1}{2}\left(K^{(N)}_{t\alpha;11}E_{N-1} + K^{(N)}_{t\alpha;12}E_N\right) + \frac{1}{2}\left(ik_0\sum_{\alpha} E_z^{(t\alpha)}(L)\right) \ . \tag{3.59}$$

It is obvious that Eqs. (3.58)–(3.59) include the MBCs explicitly. Thus, for $n = 0, N$, we use Eqs. (3.58)–(3.59) instead of Eq. (3.53).

At the same time, the ABCs can be written as

$$\chi(k_{t1},\omega)E_0^{(t1)} + \chi(k_{t2},\omega)E_0^{(t2)} = 0 \tag{3.60}$$

$$\chi(k_{t1},\omega)E_N^{(t1)} + \chi(k_{t2},\omega)E_N^{(t2)} = 0 \tag{3.61}$$

Considering Eq. (3.57) for $n = 2\cdots N-1$, and Eqs. (3.58)–(3.61), we have $2N$ linear equations for $2N$ unknown variables. When the variables $E_n^{(t\alpha)}$ are uniquely determined, the transmission and reflection coefficients can be obtained from the field amplitude at the ends. We have

$$\begin{aligned} R &= \left|E_z^{(t_1)}(0) + E_z^{(t_2)}(0) - I\right| \\ &= \left|E_0^{(t_1)} + E_0^{(t_2)} - I\right| \end{aligned} \tag{3.62}$$

$$\begin{aligned} T &= \left|E_z^{(t_1)}(L) + E_z^{(t_2)}(L)\right| \\ &= \left|E_N^{(t_1)} + E_N^{(t_2)}\right| \ . \end{aligned} \tag{3.63}$$

3.2.2 Conventional method

In this one-dimensional problem, since the spatial symmetry, there is an analytical solution which is available for comparison with our FEM calculation. Since the one-dimensional Helmholtz equation (3.41) and (3.42) have the general solution.

$$E_z^{(t_1)}(x) = A_1 e^{ik_1 x} + B_1 e^{-ik_1 x} \tag{3.64}$$

$$E_z^{(t_2)}(x) = A_2 e^{ik_2 x} + B_2 e^{-ik_2 x} \ , \tag{3.65}$$

where A_1, A_2, B_1 and B_2 are the field amplitudes of the two polariton modes. The boundary conditions (3.58)–(3.59) and (3.60)–(3.61) yield

$$\begin{aligned} A_1 + B_1 + A_2 + B_2 &= E_0 + RE_0 \\ ik_1(A_1 - B_1) + ik_2(A_2 - B_2) &= ik_0(E_0 - RE_0) \\ A_1 e^{ik_1 L} + B_1 e^{-ik_1 L} + A_2 e^{ik_2 L} + B_2 e^{-ik_2 L} &= TE_0 e^{ik_0 L} \\ ik_1(A_1 e^{ik_1 L} - B_1 e^{-ik_1 L}) + ik_2(A_2 e^{ik_2 L} - B_2 e^{-ik_2 L}) &= ik_0(TE_0 e^{ik_0 L}) \ , \end{aligned}$$

and

$$\begin{aligned} \chi_1(A_1 + B_1) + \chi_2(A_2 + B_2) &= 0 \\ \chi_1(A_1 e^{ik_1 L} - B_1 e^{-ik_1 L}) + \chi_2(A_2 e^{ik_2 L} - B_2 e^{-ik_2 L}) &= 0 \ . \end{aligned}$$

The unknowns variables A_1, B_1, A_2, B_2, R, T are uniquely determined by this system of equations.

3.2.3 Numerical results

To demonstrate, we calculate the transmission and reflection coefficients of the QD of the thickness L. We employ the physical parameter of the bulk CuCl, which is written on Table 3.1. The damping constant γ is set to be 100μeV. Fig. 3.3–3.5 show the spectra of the transmitted and reflected lights of the different thickness $L = 10, 15, 20$nm. The FEM results shows good agreement with the analytical solutions. Due to the exciton mode, the characteristic resonant peaks appear in the spectra. By increasing the thickness L, the position of the peaks are red-shifted by the quantum size effect. Compared to the experiments, the resonance structures of the observed spectra are well reproduced by our calculations.

3.3 Three-dimensional case

For three-dimensional case, we consider the light scattering problem by the semiconductor nanostructure of arbitraly geometry.

We consider a situation in which an incident field $E^{(\text{inc})}$ irradiates a semi-

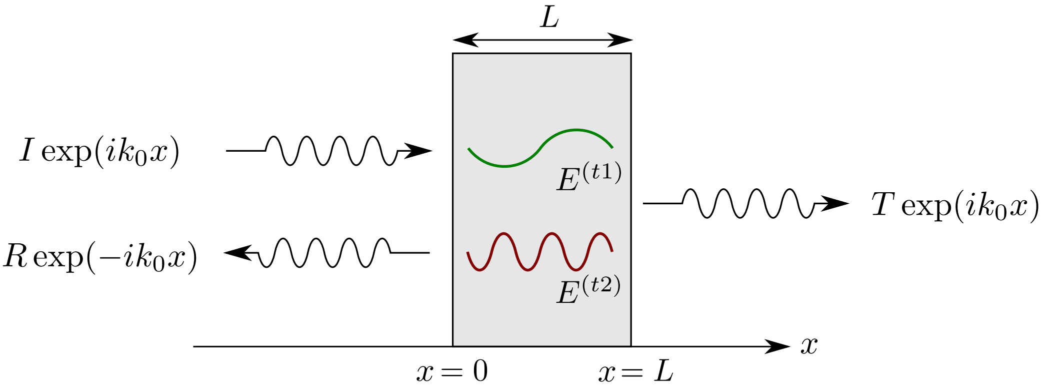

Figure 3.2: A exciton confined in thin CuCl layer of the thickness L

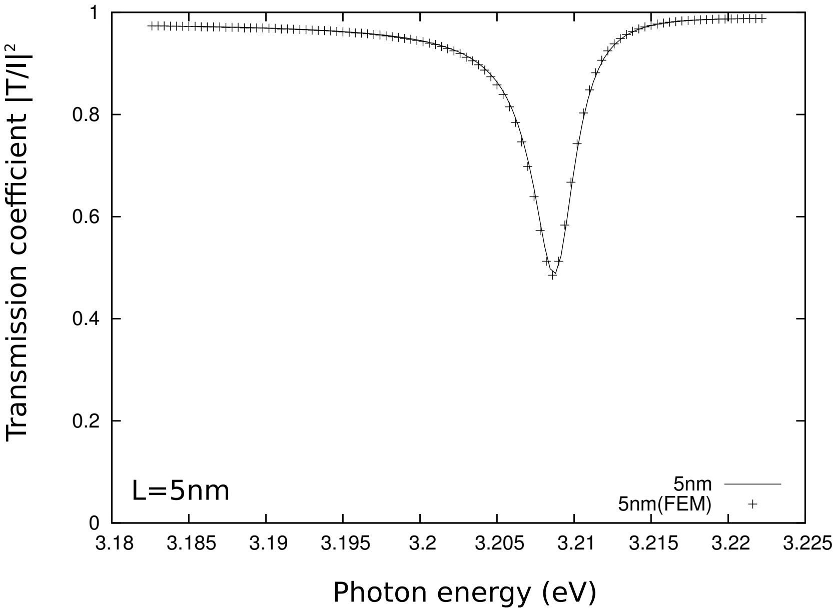

Figure 3.3: (a) The transmission coefficient of the CuCl slab with the thickness of $L = 5$ nm. The exact solution (solid line) and the FEM result (dotted line).

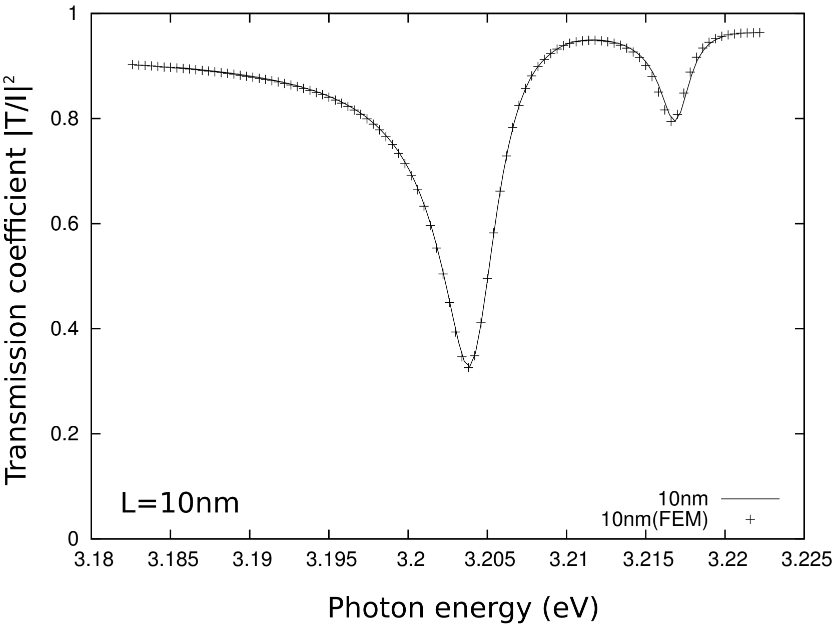

Figure 3.4: (a) The transmission coefficient of the CuCl slab with the thickness of $L = 10$ nm. The exact solution (solid line) and the FEM result (dotted line).

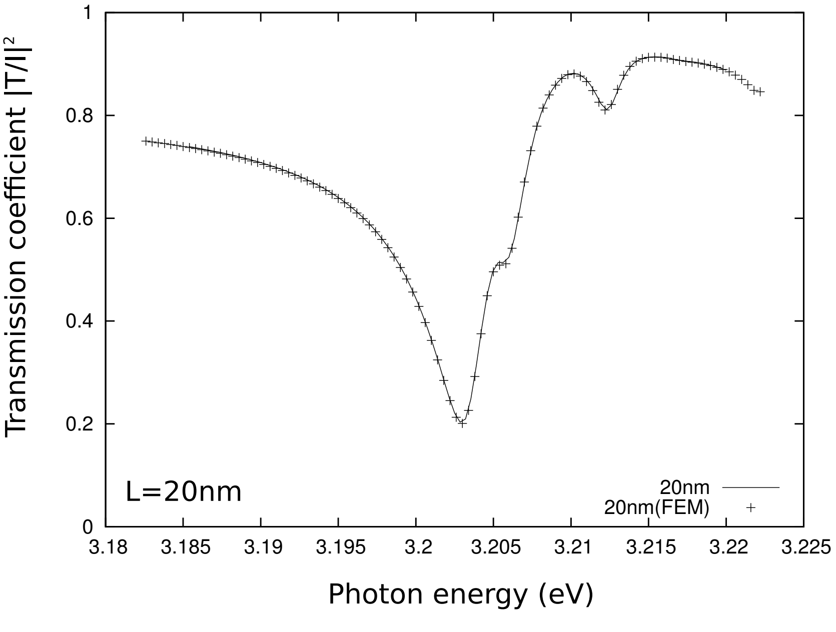

Figure 3.5: (a) The transmission coefficient of the CuCl slab with the thickness of $L = 20$ nm. The exact solution (solid line) and the FEM result (dotted line).

conductor nanostructure (region Ω_1) surrounded by a dielectric material with a dielectric constant of ε, as illustrated schematically in Fig. 3.6 (a). The surface of region Ω_1 is denoted by Γ_1. In an open-region scattering problem, the scattered field propagates to infinity, but to restrict the computational region, we introduce an artificial interface Γ_0 within which the EM fields are numerically calculated by subdividing the region into small volume elements. The dielectric area between Γ_0 and Γ_1, denoted by Ω_0, and the exterior (far-field) region, denoted by Ω_∞, have dielectric constants of ϵ, and thus there is no reflection or refraction at Γ_0.

3.3.1 Functionals

Electromagnetic field modes

The total electric field $\mathbf{E}^{(1)}$ in region Ω_1 is obtained as

$$\mathbf{E}^{(1)} = \sum_{\mu=1}^{2} \mathbf{E}^{(t_\mu)} - \nabla\Phi, \tag{3.66}$$

while the electric field in region Ω_0, denoted by $\mathbf{E}^{(0)}$, consists of the incident field and the scattered fields from the semiconductor nanostructure. In region Ω_∞, the electric field $\mathbf{E}^{(\infty)}$ is given by

$$\mathbf{E}^{(\infty)} = \mathbf{E}^{(\mathrm{inc})} + \mathbf{E}_\infty^{(\mathrm{scat})}, \tag{3.67}$$

where $\mathbf{E}_\infty^{(\mathrm{scat})}$ is the scattered field in region Ω_∞. When we assume a spherical geometry for Γ_0, as illustrated in Fig. 3.6, it is convenient to expand $\mathbf{E}_\infty^{(\mathrm{scat})}$ in terms of vector spherical waves as follows:

$$\mathbf{E}_\infty^{(\mathrm{scat})}(\mathbf{r}) = \sum_{n=1}^{N_c} \sum_{m=-n}^{n} \Big[a_{mn}\mathbf{M}_{mn}(\mathbf{r}) + b_{mn}\mathbf{N}_{mn}(\mathbf{r}) \Big], \tag{3.68}$$

where the integer N_c is the cut-off angular momentum, a_{mn} and b_{mn} are expansion coefficients, and $\mathbf{N}_{mn}$ and $\mathbf{M}_{mn}$ are vector spherical harmonics (defined in the Appendix A).

We consider a plane-wave incident field given by $\mathbf{E}^{(\mathrm{inc})}(\mathbf{r}) = \mathbf{I}_0 \exp(ikz)$

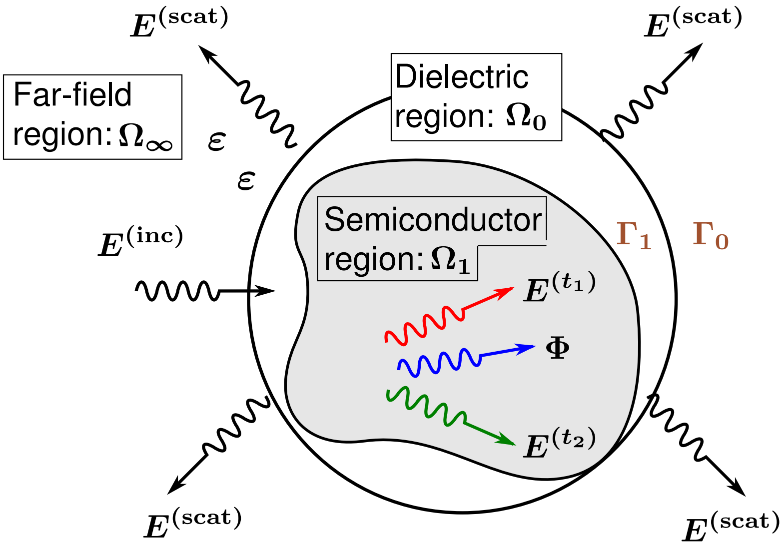

$$\boldsymbol{E}^{(\infty)} = \boldsymbol{E}^{(\mathrm{inc})} + \boldsymbol{E}_{\infty}^{(\mathrm{scat})}$$

Figure 3.6: (a) Schematic illustration of a semiconductor nanostructure (region Ω_1) surrounded by a dielectric (regions Ω_0 and Ω_∞). The interface between the semiconductor nanostructure and dielectric is denoted by Γ_1, and an artificial spherical surface, denoted by Γ_0, is introduced within which the region is subdivided into small volume elements for the numerical computation. Various wave modes are also depicted. (b) The dispersion relations of two transverse exciton polaritons and one longitudinal exciton in bulk CuCl (the CuCl parameters for the calculation are summarized in Table 3.1).

with $\mathbf{I}_0$ being polarized in the x-direction. The incident field can be expanded as

$$\mathbf{E}^{(\mathrm{inc})} = I_0 \sum_{n=1}^{N_c} \sum_{m=\pm 1} \Big[p_{mn}\mathbf{M}_{mn}(\mathbf{r}) + q_{mn}\mathbf{N}_{mn}(\mathbf{r}) \Big], \tag{3.69}$$

with

$$p_{1n} = -q_{1n} = i^{n+1}\frac{2n+1}{2n(n+1)}, \tag{3.70}$$

and

$$p_{-1n} = -q_{-1n} = i^{n+1}\Big(n+\frac{1}{2}\Big). \tag{3.71}$$

The value of N_c will depend on the distance between Γ_0 and Γ_1. As evanescent waves with a higher angular momentum decay more rapidly from Γ_1, we can take a smaller N_c for the larger distance between Γ_0 and Γ_1. Conversely, the volume of region Ω_0 can be reduced by taking a large N_c value, which reduces computational time and memory storage.

Boundary conditions

At the interface Γ_1, the following Maxwell's boundary conditions (MBCs) are satisfied:

$$\hat{n}_1 \times \mathbf{E}^{(0)} = \hat{n}_1 \times \mathbf{E}^{(1)}, \tag{3.72}$$

$$\hat{n}_1 \times \nabla \times \mathbf{E}^{(0)} = \hat{n}_1 \times \nabla \times \mathbf{E}^{(1)} = \sum_{\mu=1}^{2} \hat{n}_1 \times \nabla \times \mathbf{E}^{(t_\mu)}, \tag{3.73}$$

where $\hat{n}_1$ is a unit vector on Γ_1 directed outward from Ω_1 and normal to Γ_1. When the material is a dielectric or metal, there is only one wave mode, and so the EM field is uniquely determined by imposing only the MBCs. For a semiconductor, however, there are three wave modes, *i.e.*, two transverse exciton polaritons and one longitudinal exciton. Therefore, three more boundary conditions are necessary to determine the EM fields. Several types of ABCs have been proposed [22, 6, 1, 11, 13, 10], and here, we use the Pekar-type ABC [22] for which the exciton polarization $\mathbf{P}(\mathbf{r})$ vanishes at the surface of the semiconductor. Since the polarization is given by $\mathbf{P} = \chi(k,\omega)\mathbf{E}$ with $\chi(k,\omega) = (1/4\pi)[\varepsilon(k,\omega) - 1]$ being the susceptibility, the Pekar-type ABC at Γ_1 is expressed as

$$\sum_{\mu=1}^{2} \chi(k_{t_\mu}, \omega)\mathbf{E}^{(t_\mu)} + \chi(k_l, \omega)(-\nabla\Phi) = 0. \tag{3.74}$$

The normal component of the ABC (3.74) is given by

$$\hat{n}_1 \cdot \nabla\Phi = \sum_{\mu=1}^{2} \frac{\chi(k_{t_\mu}, \omega)}{\chi(k_l, \omega)} \hat{n}_1 \cdot \mathbf{E}^{(t_\mu)}, \tag{3.75}$$

and the tangential component is given by

$$\chi(k_l, \omega)\hat{n}_1 \times \nabla\Phi = \sum_{\mu=1}^{2} \chi(k_{t_\mu}, \omega)\hat{n}_1 \times \mathbf{E}^{(t_\mu)}. \tag{3.76}$$

At the artificial interface Γ_0, the MBCs are given by

$$\hat{n}_0 \times \mathbf{E}^{(0)} = \hat{n}_0 \times \mathbf{E}^{(\infty)}, \tag{3.77}$$

$$\begin{aligned} \hat{n}_0 \times \nabla \times \mathbf{E}^{(0)} &= \hat{n}_0 \times \nabla \times \mathbf{E}^{(\infty)} \\ &= k \sum_{n=1}^{N_c} \sum_{m=-n}^{n} \Big[(I_0 p_{mn} \delta_{m,\pm 1} + a_{mn}) \hat{n}_0 \times \mathbf{N}_{mn}(\mathbf{r}) \\ &\qquad + (I_0 q_{mn} \delta_{m,\pm 1} + b_{mn}) \hat{n}_0 \times \mathbf{M}_{mn}(\mathbf{r}) \Big], \end{aligned} \tag{3.78}$$

where $\hat{n}_0$ is a unit vector on Γ_0 directed outward from Ω_0 and normal to Γ_0. In Eq. (3.78), we use Eqs. (3.67)–(3.69) and the relations $\nabla \times \mathbf{N}_{mn} = k\mathbf{M}_{mn}$ and $\nabla \times \mathbf{M}_{mn} = k\mathbf{N}_{mn}$. Because the dielectric constants in regions Ω_0 and Ω_∞ are the same, the following relation should be imposed as a boundary condition at Γ_0:

$$\mathbf{E}^{(\infty)} = \mathbf{E}^{(0)}. \tag{3.79}$$

Functionals

The electric field $\mathbf{E}^{(0)}$ in region Ω_0 obeys the following Maxwell's wave equation:

$$\nabla \times \nabla \times \mathbf{E}^{(0)} - k^2\mathbf{E}^{(0)} = 0\ , \tag{3.80}$$

with $k = \varepsilon(\omega/c)^2$ and ω being the frequency of $\mathbf{E}^{(0)}$. According to the general variation principle, a weak-form functional leading to Eq. (3.80) can be obtained as

$$\begin{aligned}\mathcal{F}_0[\mathbf{E}^{(0)}] = &-\frac{1}{2}\iiint_{\Omega_0} \mathrm{d}^3\mathbf{r}\,\left\{[\nabla\times\mathbf{E}^{(0)*}]\cdot[\nabla\times\mathbf{E}^{(0)}] - k^2\mathbf{E}^{(0)*}\cdot\mathbf{E}^{(0)}\right\}\\ &+\frac{1}{2}\iint_{\partial\Omega_0} \mathrm{d}^2\mathbf{r}\,\mathbf{E}^{(0)*}\cdot[\hat{n}_0\times\nabla\times\mathbf{E}^{(0)}]\,,\end{aligned}\tag{3.81}$$

where $\partial\Omega_0$, containing Γ_0 and Γ_1, represents the surface area surrounding the region Ω_0. The MBC [Eq. (3.78)] can be added to $\mathcal{F}_0$ by replacing $[\hat{n}_0\times\nabla\times\mathbf{E}^{(0)}]$ in Eq. (3.81) with the expression in Eq. (3.78).

In region Ω_1,the electric-field components $\mathbf{E}^{(t_1)}$ and $\mathbf{E}^{(t_2)}$ of the two exciton polaritons are governed by the Maxwell's wave equation

$$\nabla\times\nabla\times\mathbf{E}^{(t_\mu)} - k_{t_\mu}^2\mathbf{E}^{(t_\mu)} = 0,\tag{3.82}$$

whereas for the longitudinal field $\mathbf{E}^{(l)} = -\nabla\Phi$, the potential Φ satisfies Poisson's equation:

$$\nabla^2\Phi + k_l^2\Phi = 0.\tag{3.83}$$

A weak-form functional leading to Eqs. (3.82) and (3.83) is given by

$$\begin{aligned}\mathcal{F}_1[\mathbf{E}^{(t_1)},\mathbf{E}^{(t_2)},\Phi] = &-\frac{1}{2}\sum_{\mu=1}^{2}\iiint_{\Omega_1}\mathrm{d}^3\mathbf{r}\,\left\{[\nabla\times\mathbf{E}^{(t_\mu)*}]\cdot[\nabla\times\mathbf{E}^{(t_\mu)}] - k_{t_\mu}^2\mathbf{E}^{(t_\mu)*}\cdot\mathbf{E}^{(t_\mu)}\right\}\\ &+\frac{1}{2}\sum_{\mu=1}^{2}\iint_{\partial\Omega_1}\mathrm{d}^2\mathbf{r}\,\mathbf{E}^{(t_\mu)*}\cdot[\hat{n}_1\times\nabla\times\mathbf{E}^{(t_\mu)}]\\ &-\frac{1}{2}\iiint_{\Omega_1}\mathrm{d}^3\mathbf{r}\,\left[(\nabla\Phi^*)\cdot(\nabla\Phi) - k_l^2\Phi^*\cdot\Phi\right]\\ &+\frac{1}{2}\iint_{\partial\Omega_1}\mathrm{d}^2\mathbf{r}\,\Phi^*\left(\hat{n}_1\cdot\nabla\Phi\right),\end{aligned}\tag{3.84}$$

where $\partial\Omega_1$ represents the surface area surrounding the region Ω_1. The ABC [Eq. (3.75)] can be added to $\mathcal{F}_1$ by substituting Eq. (3.75) into Eq. (3.84).

3.3.2 Finite element analysis

To numerically calculate the solutions of the boundary-value problem, the computational region is subdivided into small volume elements. As we choose a tetrahedral geometry for the volume elements, the interface is subdivided into triangular elements. All the volume elements are labeled by a set of integers $e = 1, 2, \cdots$, and the nodes of each volume element are labeled as $i = 1, 2, 3, 4$. The ith node in the eth volume element is denoted by a local label $(e; i)$. Any node can be indicated by multiple local labels because the node belongs to multiple volume elements. For one-to-one mapping between the nodes and integers, we create a global label $s(e; i) = 1, 2, \cdots$ for all nodes. The triangular element at the interface belonging to the eth volume element is denoted by f_e.

Basis functions

In the conventional FEM formalism, scalar or vector fields are assigned at the nodes of the volume elements, referred to as nodal elements. For transverse vector fields, however, a higher accuracy can be obtained if the fields are assigned at the edges of the volume elements (edge elements) [8, 7]. Here, we develop a hybrid method, *i.e.*, the scalar field Φ is represented by nodal elements and the transverse vector fields $\mathbf{E}^{(0)}$, $\mathbf{E}^{(t_1)}$, and $\mathbf{E}^{(t_2)}$ are represented by edge elements.

Scalar fields in the tetrahedral element are expressed by the nodal-element basis $L_{(e;i)}(\mathbf{r})$ defined as

$$L_{(e;i)}(\mathbf{r}) = a^x_{(e;i)} x + a^y_{(e;i)} y + a^z_{(e;i)} z + b_{(e;i)} \ , \tag{3.85}$$

where the coefficients $a^x_{(e;i)}$, $a^y_{(e;i)}$, $a^z_{(e;i)}$, and $b_{(e;i)}$ are obtained from the condition $L_{(e;i)}[\mathbf{r}_{(e;j)}] = \delta_{ij}$, with $\mathbf{r}_{(e;i)}$ being the position of node $(e; i)$.

In contrast, the vector fields are expressed by the edge-element basis $\mathbf{W}_{(e;ij)}(\mathbf{r})$ defined as

$$\mathbf{W}_{(e;ij)}(\mathbf{r}) = \frac{1}{l_{ij}} \left[L_{(e;i)}(\mathbf{r}) \nabla L_{(e;j)}(\mathbf{r}) - L_{(e;j)}(\mathbf{r}) \nabla L_{(e;i)}(\mathbf{r}) \right] \ , \tag{3.86}$$

where l_{ij} is the length of the edge between nodes $(e;i)$ and $(e;j)$. Figure shows the fields of the nodal- and edge-element bases. By using these basis functions, the EM fields can be approximated by a linear combination of basis functions as follows:

$$\mathbf{E}^{(0)}(\mathbf{r}) = \sum_{e\in\Omega_0}\sum_{ij=1}^{4} E^{(0)}_{s(e;i)s(e;j)}\mathbf{W}_{(e;ij)}(\mathbf{r}), \tag{3.87}$$

$$\mathbf{E}^{(t_\mu)}(\mathbf{r}) = \sum_{e\in\Omega_1}\sum_{ij=1}^{4} E^{(t_\mu)}_{s(e;i)s(e;j)}\mathbf{W}_{(e;ij)}(\mathbf{r}), \tag{3.88}$$

$$\Phi(\mathbf{r}) = \sum_{e\in\Omega_1}\sum_{i=1}^{4} \Phi_{s(e;i)}L_{(e;i)}(\mathbf{r}). \tag{3.89}$$

The expansion coefficients $E^{(\alpha)}_{s(e;i)s(e;j)}$ with $\alpha = \{0,\ t_1,\ t_2\}$ and $\Phi_{s(e;i)}$ represent field amplitudes at specific points:

$$E^{(\alpha)}_{s(e;i)s(e;j)} = \hat{t}_{(e;ij)} \cdot \mathbf{E}^{(\alpha)}[\mathbf{r}_{(e;ij)}], \tag{3.90}$$

$$\Phi_{s(e;i)} = \Phi[\mathbf{r}_{(e;i)}]\ , \tag{3.91}$$

where $\hat{t}_{(e;ij)}$ denotes a unit vector parallel to the edge between nodes $(e;i)$ and $(e;j)$, and $\mathbf{r}_{(e;ij)} = [\mathbf{r}_{(e;i)} + \mathbf{r}_{(e;j)}]/2$. Note that the edge-element basis $\mathbf{W}_{(e;ij)}(\mathbf{r})$ automatically satisfies the divergence-free condition $[\nabla\cdot\mathbf{W}_{(e;ij)} = 0]$ of transverse fields [7], and thus, the transverse character of $\mathbf{E}^{(\alpha)}$ is guaranteed. This is why edge elements avoid spurious solutions and provide more accurate transverse fields than those calculated using nodal elements.

Functionals

The functional $\mathcal{F}_0$ in the FEM is obtained by substituting Eq. (3.78) into Eq. (3.81) and using Eq. (3.87) as follows:

$$
\begin{aligned}
\mathcal{F}_0 = &-\frac{1}{2}\sum_{e\in\Omega_0}\sum_{ijkl=1}^{4} K^{(e)}_{ijkl}(k)E^{(0)*}_{s(e;i)s(e;j)}E^{(0)}_{s(e;k)s(e;l)} \\
&+\frac{k}{2}\sum_{e;f_e\in\Gamma_0}\sum_{ij=1}^{4}\sum_{n=1}^{N_c}\sum_{m=-n}^{n} E^{(0)*}_{s(e;i)s(e;j)} \\
&\qquad\times\Big\{(I_0 p_{mn}\delta_{m,\pm 1}+a_{mn})\iint_{\Gamma^{(f_e)}}\mathrm{d}^2\mathbf{r}\,\mathbf{W}_{(e;ij)}\cdot[\hat{n}_0\times\mathbf{N}_{mn}(\mathbf{r})]_{f_e} \\
&\qquad\quad+(I_0 q_{mn}\delta_{m,\pm 1}+b_{mn})\iint_{\Gamma^{(f_e)}}\mathrm{d}^2\mathbf{r}\,\mathbf{W}_{(e;ij)}\cdot[\hat{n}_0\times\mathbf{M}_{mn}(\mathbf{r})]_{f_e}\Big\} \\
&+\frac{1}{2}\sum_{e;f_e\in\Gamma_1}\sum_{ij=1}^{4} E^{(0)*}_{s(e;i)s(e;j)}\iint_{\Gamma^{(f_e)}}\mathrm{d}^2\mathbf{r}\,\mathbf{W}_{(e;ij)}\cdot[\hat{n}_0\times\nabla\times\mathbf{E}^{(0)}]_{f_e},
\end{aligned}
\tag{3.92}
$$

with

$$
K^{(e)}_{ijkl}(k) = \iiint_{\Omega^{(e)}}\mathrm{d}^3\mathbf{r}\,\Big\{[\nabla\times\mathbf{W}_{(e;ij)}]\cdot[\nabla\times\mathbf{W}_{(e;kl)}] - k^2\mathbf{W}_{(e;ij)}\cdot\mathbf{W}_{(e;kl)}\Big\}\,, \tag{3.93}
$$

where $\Omega^{(e)}$ is the region of the eth volume element, $\Gamma^{(f_e)}$ is the area of the interface f_e, and $\sum_{e;f_e\in\Gamma_0(\Gamma_1)}$ denotes the summation over the volume elements e that have one triangular surface f_e belonging to Γ_0 (Γ_1).

The other functional $\mathcal{F}_1$ is obtained by substituting Eq. (3.75) into Eq. (3.84) and using Eqs. (3.88) and (3.89) as follows:

$$\begin{aligned}\mathcal{F}_1 =& -\frac{1}{2}\sum_{\mu=1}^{2}\sum_{e\in\Omega_1}\sum_{ijkl=1}^{4} K_{ijkl}^{(e)}(k_{t_\mu})E_{s(e;i)s(e;j)}^{(t_\mu)*}E_{s(e;k)s(e;l)}^{(t_\mu)}\\ &+\frac{1}{2}\sum_{\mu=1}^{2}\sum_{e;f_e\in\Gamma_1}\sum_{ij=1}^{4} E_{s(e;i)s(e;j)}^{(t_\mu)*}\iint_{\Gamma^{(f_e)}}\mathrm{d}^2\mathbf{r}\ \mathbf{W}_{(e;ij)}\cdot[\hat{n}_1\times\nabla\times\mathbf{E}^{(t_\mu)}]_{f_e}\\ &-\frac{1}{2}\sum_{e\in\Omega_1}\sum_{ij=1}^{4} J_{ij}^{(e)}(k_l)\Phi_{s(e;i)}^{*}\Phi_{s(e;j)}\\ &+\frac{1}{2}\sum_{\mu=1}^{2}\sum_{e;f_e\in\Gamma_1}\sum_{ij=1}^{4}\frac{\chi(k_{t_\mu},\omega)}{\chi(k_l,\omega)}\Phi_{s(e;i)}^{*}E_{s(e;i)s(e;j)}^{(t_\mu)}\iint_{\Gamma^{(f_e)}}\mathrm{d}^2\mathbf{r}\ L_{(e;i)}\ [\hat{n}_1\cdot\mathbf{W}_{(e;ij)}]_{f_e},\end{aligned} \tag{3.94}$$

with

$$J_{ij}^{(e)}(k_l) = \iiint_{\Omega^{(e)}}\mathrm{d}^3\mathbf{r}\ \Big\{\big[\nabla L_{(e;i)}\big]\cdot\big[\nabla L_{(e;j)}\big] - k_l^2 L_{(e;i)}L_{(e;j)}\Big\}. \tag{3.95}$$

The total functional $\mathcal{F}$ is then given by

$$\mathcal{F} = \mathcal{F}_0 + \mathcal{F}_1. \tag{3.96}$$

Maxwell's wave equations can be derived from the stationary condition $\delta\mathcal{F} = 0$ with respect to $E_{s(e;i)s(e;j)}^{(\alpha)}$ and $\Phi_{s(e;i)}$. To include the MBC [Eq. (3.73)] in the derived Maxwell's wave equations, we find a stationary condition

$$\sum_{\alpha=\{0,t_1,t_2\}}\frac{\delta\mathcal{F}}{\delta E_{s(e;i)s(e;j)}^{(\alpha)}} = 0. \qquad [\text{for}\ \ s(e;i),s(e;j)\in\Gamma_1] \tag{3.97}$$

In conjunction with Eq. (3.73), the stationary condition eliminates the contributions from the surface-integration terms including $[\hat{n}_0\times\nabla\times\mathbf{E}^{(0)}]$ and $[\hat{n}_1\times\nabla\times\mathbf{E}^{(t_\mu)}]$ at Γ_1, thus including the MBC [Eq. (3.73)].

The other stationary conditions are given by

$$\frac{\delta \mathcal{F}}{\delta E^{(\alpha)}_{s(e;i)s(e;j)}} = 0, \quad [\text{for} \;\; s(e;i), s(e;j) \notin \Gamma_1] \tag{3.98}$$

$$\frac{\delta \mathcal{F}}{\delta \Phi_{s(e;i)}} = 0. \tag{3.99}$$

Under these three stationary conditions, the Maxwell's wave equations are represented by linear equations with respect to $E^{(\alpha)}_{s(e;i)s(e;j)}$ and $\Phi_{s(e;i)}$. Because the procedure to obtain the linear equations is straightforward [16] and the resulting equations are complicated, the specific linear equations are not presented in this paper.

Explicit boundary conditions

Unlike the boundary conditions in Sec. 3.3.2, the remaining boundary conditions, Eqs. (3.72), (3.76), and (3.79), are imposed explicitly. Note that the MBC [Eq. (3.72)] between different dielectrics or between a dielectric and metal is automatically satisfied for edge elements because the tangential electric field at the interface expresses common fields that belong to the different regions of the interface. However, this is not the case for the interface Γ_1 between the dielectric and semiconductor because the electric field in a semiconductor area consists of $\mathbf{E}^{(t_1)}$, $\mathbf{E}^{(t_2)}$, and $(-\nabla\Phi)$. Therefore, we set the three variables $E^{(t_1)}_{s(e;i)s(e;j)}$, $E^{(t_2)}_{s(e;i)s(e;j)}$, and $E^{(0)}_{s(e;i)s(e;j)}$ at each edge element on the interface Γ_1 and explicitly impose the MBC [Eq. (3.72)]. The discretized forms of the explicit boundary conditions, Eqs. (3.72) and (3.76), are

$$E^{(t_1)}_{s(e;i)s(e;j)} + E^{(t_2)}_{s(e;i)s(e:j)} - \frac{\Phi_{s(e;j)} - \Phi_{s(e;i)}}{l_{ij}} = E^{(0)}_{s(e;i)s(e;j)}, \quad [s(e,i), s(e,j) \in \Gamma_1] \tag{3.100}$$

$$\chi(k_{t_1},\omega) E^{(t_1)}_{s(e;i)s(e;j)} + \chi(k_{t_2},\omega) E^{(t_2)}_{s(e;i)s(e;j)} - \chi(k_l,\omega) \frac{\Phi_{s(e;j)} - \Phi_{s(e;i)}}{l_{ij}} = 0. \quad [s(e,i), s(e,j) \in \Gamma_1] \tag{3.101}$$

The explicit boundary condition in Eq. (3.79) is rewritten by taking the inner product of Eq. (3.79) with $\mathbf{M}^*_{uv}$ and integrating over the interface Γ_0 as follows:

$$(I_0 p_{uv}\delta_{u,\pm 1} + a_{uv})S^{(M)}_{uv} = \sum_{e;f_e\in\Gamma_0}\sum_{ij=1}^{4} E^{(0)}_{s(e;i)s(e;j)} \iint_{\Gamma^{(f_e)}} d^2\mathbf{r}\mathbf{M}^*_{uv}\cdot\mathbf{W}_{(e;ij)}, \tag{3.102}$$

where $S^{(M)}_{uv}$ is defined in the Appendix. In a similar manner, we take the inner product of Eq. (3.79) with $\mathbf{N}^*_{uv}$ and integrate over the interface Γ_0:

$$(I_0 q_{uv}\delta_{u,\pm 1} + b_{uv})S^{(N)}_{uv} = \sum_{e;f_e\in\Gamma_0}\sum_{ij=1}^{4} E^{(0)}_{s(e;i)s(e;j)} \iint_{\Gamma^{(f_e)}} d^2\mathbf{r}\mathbf{N}^*_{uv}\cdot\mathbf{W}_{(e;ij)}, \tag{3.103}$$

where $S^{(N)}_{uv}$ is defined in the Appendix.

Let us check that the number of variables is equal to the number of equations. The numbers of equations defined by Eqs. (3.102) and (3.103) are equal to the numbers of variables a_{mn} and b_{mn}, respectively, and the numbers of equations defined by Eqs. (3.98) and (3.99) are equals to the numbers of variables $E^{(\alpha)}_{s(e;i)s(e;j)}$ $[s(e;i), s(e;j) \notin \Gamma_1]$ and $\Phi_{s(e;i)}$, respectively. The remaining variables are $E^{(\alpha)}_{s(e;i)s(e;j)}$ $[s(e;i), s(e;j) \in \Gamma_1]$, and the number of these variables is $3M$, where M is the number of edges on Γ_1. The remaining equations are explicit boundary conditions [Eqs. (3.100) and (3.101)] and the stationary condition [Eq. (3.97)], each of which provides M equations, and thus there are a total of $3M$ equations. Therefore, $E^{(\alpha)}_{s(e;i)s(e;j)}$ and $\Phi_{s(n;i)}$ can be uniquely determined.

Mie theory

To begin, we calculate the scattering cross section of a spherical QD. The scattering cross section for this geometry has also been calculated using Mie theory, in which the EM fields inside and outside the sphere are expanded by vector spherical harmonics and the expansion coefficients are determined from the MBCs and Pekar-type ABC [26]. The validity of the present FEM is confirmed by a comparison of the cross section with that calculated by Mie theory.

For the Mie theory, the electric fields in the spherical particle are expanded as

$$\mathbf{E}^{(0)}(\mathbf{r}) = \sum_{n=0}^{\infty}\sum_{m=-n}^{n} a_{mn}\mathbf{M}_{mn}(k_0 r,\theta,\phi) + b_{mn}\mathbf{N}_{mn}(k_0 r,\theta,\phi) + \mathbf{E}^{(inc)}(\mathbf{r})\ , \tag{3.104}$$

and

$$\mathbf{E}^{(t_1)}(\mathbf{r}) = \sum_{n=0}^{\infty}\sum_{m=-n}^{n} c_{mn}^{(t_1)}\mathbf{M}_{mn}^{(1)}(k_{t_1} r,\theta,\phi) + d_{mn}^{(t_1)}\mathbf{N}_{mn}^{(1)}(k_{t_1} r,\theta,\phi) \tag{3.105}$$

$$\mathbf{E}^{(t_2)}(\mathbf{r}) = \sum_{n=0}^{\infty}\sum_{m=-n}^{n} c_{mn}^{(t_2)}\mathbf{M}_{mn}^{(1)}(k_{t_2} r,\theta,\phi) + d_{mn}^{(t_2)}\mathbf{N}_{mn}^{(1)}(k_{t_2} r,\theta,\phi) \tag{3.106}$$

$$\Phi^{(l)}(\mathbf{r}) = \sum_{n=0}^{\infty}\sum_{m=-n}^{n} e_{mn}\Psi_{mn}^{(1)}(k_l r,\theta,\phi)\ , \tag{3.107}$$

where a_{mn}, b_{mn}, $c_{mn}^{(t_1)}$, $c_{mn}^{(t_2)}$, $d_{mn}^{(t_1)}$, $d_{mn}^{(t_2)}$, and e_{mn} are the unknown coefficients, and $\mathbf{E}^{(inc)}$ is the plane wave. Moreover, $\mathbf{N}$, $\mathbf{M}$, Ψ are the vector spherical harmonics. Note that we define $\mathbf{N}^{(1)}$, $\mathbf{M}^{(1)}$, $\Psi^{(1)}$, and $\xi^{(1)}$ which use the spherical bessel function $j_n(kr)$ instead of $h_n(kr)$., and we denote the original functions in Eq. (2) and (3) as $\mathbf{N}^{(0)}$, and $\mathbf{M}^{(0)}$, because the spherical hankel function has a singularity at the origin point ($r = 0$).

Considering the MBCs at $r = R$, we have

$$h_n(k_0R)a_{mn} + I_0 h_n(k_0R)p_{mn} = j_n(k_{t_1}R)c_{mn}^{(t_1)} + j_n(k_{t_2}R)c_{mn}^{(t_2)} \tag{3.108}$$

$$\xi_n^{(0)'}(k_0R)a_{mn} + I_0\xi_n^{(0)'}(k_0R)p_{mn} = \xi_n^{(1)'}(k_{t_1}R)c_{mn}^{(t_1)} + \xi_n^{(1)'}(k_{t_2}R)c_{mn}^{(t_2)} \tag{3.109}$$

$$\frac{\xi_n^{(0)'}(k_0R)}{k_0R}b_{mn} + I_0\frac{\xi_n^{(0)'}(k_0R)}{k_0R}q_{mn} = \frac{\xi_n^{(1)'}(k_{t_1}R)}{k_{t_1}R}d_{mn}^{(t_1)} + \frac{\xi_n^{(1)'}(k_{t_2}R)}{k_{t_2}R}d_{mn}^{(t_2)} \tag{3.110}$$

$$k_0 h_n(k_0R)b_{mn} + k_0 h_n(k_0R)I_0 q_{mn} = k_{t_1} j_n(k_{t_1}R)d_{mn}^{(t_1)} + k_{t_2} j_n(k_{t_2}R)d_{mn}^{(t_2)}\ . \tag{3.111}$$

where $p_m n$ and $q_m n$ are the expansion coefficients of the plain wave, which is defined in the previous section.

In similar manner, the ABCs is also written as

$$\chi(k_{t_1},\omega)j_n(k_{t_1}R)c_{mn}^{(t_1)} + \chi(k_{t_2},\omega)j_n(k_{t_2}R)c_{mn}^{(t_2)} = 0 \tag{3.112}$$

$$\chi(k_{t_1},\omega)\frac{\xi_n^{(1)'}(k_{t_1}R)}{k_{t_1}R}c_{mn}^{(t_1)} + \chi(k_{t_2},\omega)\frac{\xi_n^{(1)'}(k_{t_2}R)}{k_{t_2}R}c_{mn}^{(t_2)} - \chi(k_l,\omega)\frac{j_n(k_lR)}{k_lR}e_{mn} = 0 \tag{3.113}$$

$$\begin{aligned} n(n+1)\chi(k_{t_1},\omega)\frac{j_n(k_{t_1}R)}{k_{t_1}R}c_{mn}^{(t_1)} + n(n+1)\chi(k_{t_1},\omega)\frac{j_n(k_{t_2}R)}{k_{t_2}R}c_{mn}^{(t_2)} & \\ -\chi(k_l,\omega)j_n'(k_lR)e_{mn} &= 0\,. \end{aligned} \tag{3.114}$$

The unknowns are uniquely determined by Eq. (3.108)-(3.114).

3.3.3 Numerical results

We apply the present FEM to light scattering problems in semiconductor nanostructures. The scattering cross section σ_s is calculated using the expansion coefficients a_{mn} and b_{mn} of $\mathbf{E}_\infty^{(\mathrm{scat})}(\mathbf{r})$ as follows:

$$\sigma_s = \frac{1}{k^2}\sum_{n=1}^{N_c}\sum_{m=-n}^{n}\mathcal{N}_{mn}(|a_{mn}|^2 + |b_{mn}|^2), \tag{3.115}$$

where $\mathcal{N}_{mn}$ is defined in the Appendix A.

Spherical QD

We consider a spherical QD of CuCl with a 10-nm diameter. Spherical QDs can be synthesized in a glass matrix [12], and recently, spherical CuCl QDs have been fabricated from a bulk sample using laser ablation in superfluid helium; size selective transportation of the QDs has also been reported [15]. The lowest exciton of CuCl, known as the Z_3 exciton, has a simple electronic structure and a Bohr radius of 0.7 nm. Since the exciton Bohr radius is sufficiently smaller than the QD diameter, we can use the bulk exciton parameters. We take the Z_3 exciton into account in the following calculations

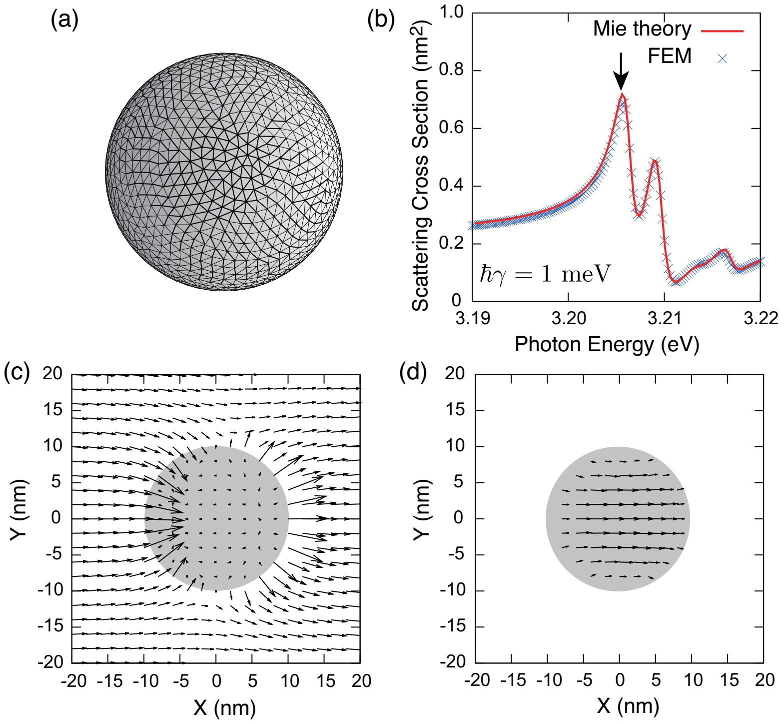

Figure 3.7: (a) Volume element mesh for a spherical QD. (b) Scattering cross section of a spherical QD of CuCl with a 10-nm diameter calculated by the present FEM (crosses) and by Mie theory (solid line). (c) Vector plots of the calculated electric field at the resonant photon energy indicated by the arrow in (b). (d) Vector plots of the calculated exciton polarization at the resonant photon energy indicated by the arrow in (b).

using the parameters listed in Table 3.1.

Figure 3.7 (a) shows the volume element mesh in the QD region. A total of 6609 nodes and 35429 elements were used in the calculation. Figure 3.7 (b) shows the calculated scattering cross sections for an incident plane wave polarized in the x-direction using the present FEM (crosses) and Mie theory (solid line); the exciton damping energy was set to $\hbar\gamma = 1$ meV. The FEM results exhibit excellent agreement with those of Mie theory, which confirms the validity of the present FEM. Figures 3.7 (c) and (d) show the distributions of the electric field and exciton polarization under the resonant photon energy of 3.206 eV, respectively. A strong enhanced field appears around the edge of the QD, as shown in Fig. 3.7 (c). This enhanced-field distribution appears in metallic nanostructures because of the surface-plasmon resonant scattering, whereas in semiconductor nanostructures, it originates from the exciton resonance. The profile of the polarization field in Fig. 3.7 (d) indicates that the excited state is a 1s-like nodeless exciton.

Hexagonal-disk QD

To demonstrate the advantages of the present FEM, we consider a hexagonal-disk QD. In contrast to the spherical geometry, there are no suitable vector basis functions. Furthermore, other established numerical techniques cannot include the exciton effect for nanostructures with an arbitrary geometry. However, we show here that the present FEM is capable of calculating the light scattering from a hexagonal-disk QD of ZnO. The exciton of ZnO has a large binding energy of 60 meV, and by virtue of this fact, room-temperature laser emission from excitons in ZnO microcrystallite thin films has been realized; the hexagonal ZnO QDs were grown by laser molecular beam epitaxy [30].

Figure 3.8 (a) shows the volume element mesh in the QD region, and in this case, 12947 nodes and 72169 elements were used. Figure 3.8 (b) shows the calculated scattering cross section for an incident plane wave propagating in the z-direction and polarized in the x-direction; the exciton damping energy was set to $\hbar\gamma = 1$ meV. The electric field distributions at the resonant photon energies, indicated by the left and right arrows, are mapped in Fig. 3.8 (c) and

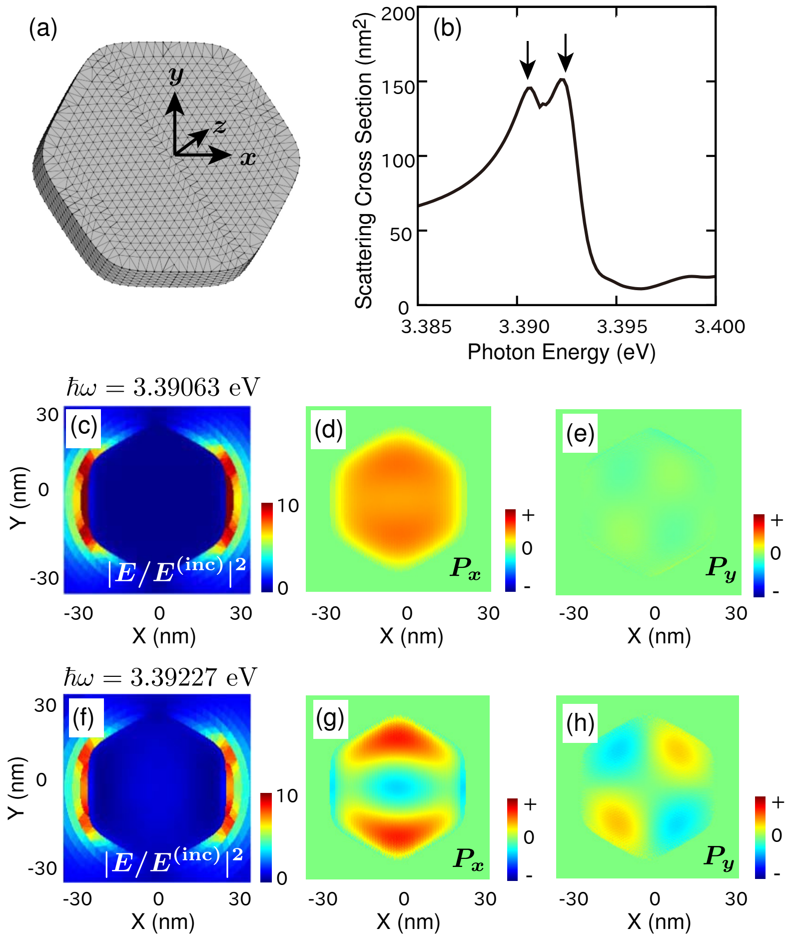

Figure 3.8: (a) Volume element mesh for a hexagonal-disk QD. (b) Scattering cross section calculated by the present FEM of a hexagonal-disk QD of ZnO with a length of 30 nm and a height of 10 nm. At the resonant photon energy of 3.39063 eV indicated by the left arrow in (b), (c) the magnitudes of the electric fields and the (d) x- and (e) y-components of the exciton polarization are plotted in the x–y plane of the top surface of the QD. At the resonant photon energy of 3.39227 eV indicated by the right arrow in (b), (f) the magnitudes of the electric fields and the (g) x- and (h) y-components of the exciton polarization are plotted in the same plane.

Fig. 3.8 (f), respectively. The magnitudes of the field have been normalized to the magnitude of the incident field. Both scattered fields are enhanced by a factor of 10 at the edges of the hexagonal-disk QD near the x-axis. Although these field distributions are similar, the exciton polarization patterns are quite different, as can be seen in Fig. 3.8 (d) and (g) (x-component) and Fig. 3.8 (e) and (h) (y-component). These plots indicate that $1s$-like and $2p$-like excitons are excited at resonant photon energies of 3.39063 eV and 3.39227 eV, respectively. Thus, the present FEM is capable of resolving the excited modes of the excitons.

3.4 Conclusion

We have developed an FEM-based EM simulation method for semiconductor nanostructures with arbitrary geometries. The EM field in a semiconductor propagates as an exciton polariton with a transverse character. At a given frequency, there are at most two exciton-polariton and one longitudinal-exciton modes in the semiconductor, and thus, an ABC is necessary in addition to the MBCs for determining the EM fields. To represent the weak-form functional in terms of variables defined in subdivided volume elements, we have developed a hybrid edge–node-element method to improve the accuracy. The transverse fields and the scalar field providing the longitudinal are represented by edge and node elements, respectively. We have found the stationary condition [Eq. (3.97)] from which the MBC [Eq. (3.73)] can be added to the derived linear equations. EM fields have been obtained by solving the equations derived from the stationary conditions [Eqs. (3.97)–(3.99)] and the equations of the explicit boundary conditions [Eqs. (3.100)–(3.103)].

The present method has been confirmed to be valid through a comparison with the scattering cross section of a spherical semiconductor calculated by Mie theory. Furthermore, we have applied the present FEM to the calculation of the electric-field and exciton-polarization distributions of a hexagonal-disk QD of ZnO. At each resonant photon energy, the characteristic polarization patterns reflecting the size-quantized exciton are well resolved by the calculations. We expect that the developed FEM will be a powerful tool for designing and analyzing semiconductor optical devices utilizing exciton resonance.

Chapter 4

Electric field enhancement at semiconductor nanogap

The localized surface plasmon resonance (LSPR) of metal provides the antenna effect which aggregates light into nano-scale area (known as hotspot). The hotspot can be considered as a photonic cavity, various types of the metallic structures has been investigated. The metallic islands with nanogap structure are one of the most popular designs of the plasmon cavity. However its quality factor is limited ($Q < 100$) by large scattering loss of the plasma oscillation.

In the previous chapter, we have beem studied the light scattering by the exciton resonance confined in arbitrary shape. As well as the LSPR, the strong enhancement of EM field appears around the edge due to the exciton resonance. In this study, we propose a new nanogap cavity utilizing exciton resonance of semiconductor. The spectral width of the confined exciton is much smaller than that of the surface plasmon. Therefore, a large improvement in the Q factor is expected in the proposed system. This high-Q factor would enable to achieve the strong-coupling regime more easily. The computation is performed by the FEM technique proposed in the previous chapter.

4.1 Model

First, we consider two CuCl disks forming a nanogap (nanodimer) as shown in Fig. 4.1(a), where the thickness $W = 5$ nm, the diameter $L = 30$ nm, and the gap width $G = 5$ nm. Let us consider a z-directed incident beam illuminates the nanodimer. The incident plain wave is linearly polarized, we assume two cases of the polarization direction: the x-direction (the electric field is parallel to the gap) and the y-direction (the electric field is perpendicular to the gap). The electric field calculations are performed based on FEM technique proposed in the previous chapter. In this work, we systematically study the geometry dependence of the enhancement factor and Q factor. We also consider the ring [Fig. 4.1(b)] and the bow-tie nanogap model [Fig. 4.6]. The result of the calculations are discussed in the following section.

4.2 Results

4.2.1 Field profile

Fig. 4.2.1 plots the electric field distribution on $z = 0$ plane at the resonant condition. (The amplitude of the incident plane wave is set to be $|\boldsymbol{E}^{(\mathrm{inc})}|^2 = 1$). For the $x-$polarized incident field, a hotspot with the enhanced electric field appears at the gap region. The arrows represent the direction of the polarization induced by the incident field. Due to dipole-dipole interactions between two nanodisks, the individual excited states hybridize and form two splitting modes: a bonding and anti-bonding combinations. The schematic diagram of the hybridization energy is illustrated in Fig. 4.3. For the x-polarized incident field, the orientation of the induced dipole moment is parallel to the gap structure. In this case, the bonding state corresponds to the mode in which the dipole moments of two nanodisks oscillate in phase with each other. Thus, only the bonding state is appeared in the optical spectra (bright mode). On the other hand, due to the optical selection rules, the anti-bonding state corresponding to the out-of-phase oscillation is not easily excited by light (dark mode). For the y-polarized incident field, the orientation of the dipole moments are perpendicular to the gap structure.

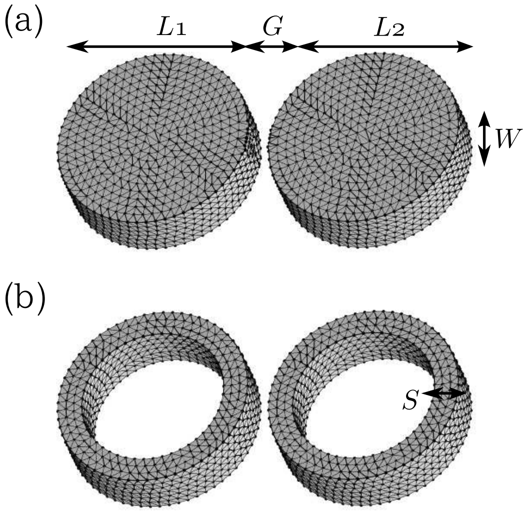

Figure 4.1: Schematic illustration of the nanogap structure and parameters definitions. (a) a dimer of nanodisk and (b) nanoring.

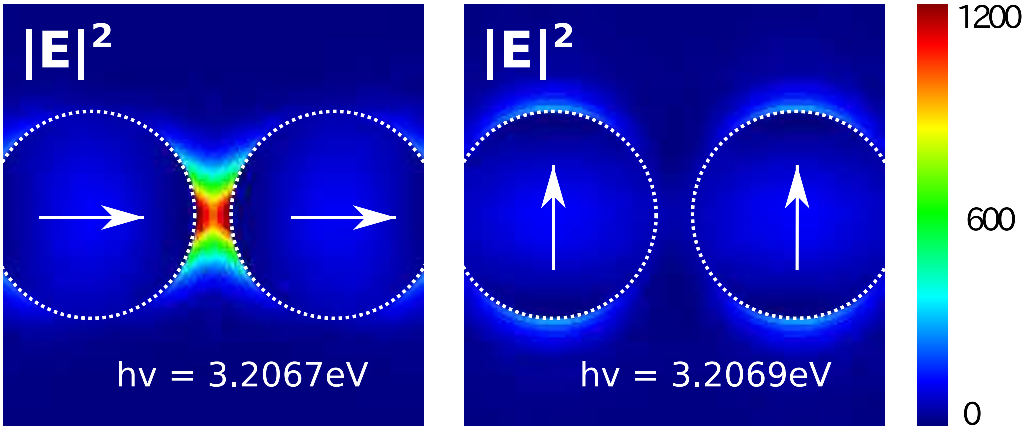

Figure 4.2: Intensity profiles of (a) the x-polarized incident and (b) the x-polarized incident. The color scale gives the strongly enhanced electric field (hotspot) appears on the gap, and the incident field is amplified by about 10^3 times stronger at this point.

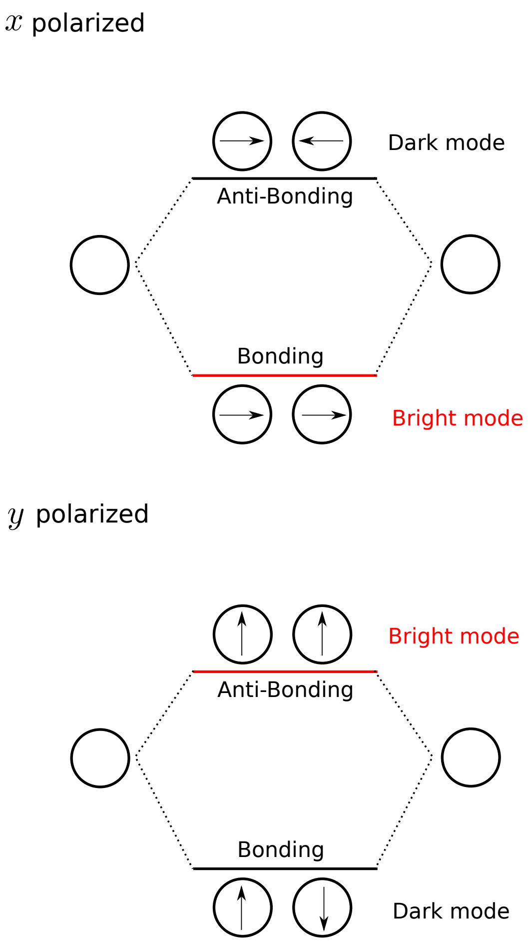

Figure 4.3: Hybridization energy diagram of the dimer nanodisk. The dipole-dipole interaction between the nanodimer results in the two hybrid states, *i.e.*, the bonding and the anti-bonding combinations.

In contrast to the previous case, the in-phase and the out-of-phase oscillation correspond, respectively, to the anti-bonding and the bonding state. Thus, in this case, only the anti-bonding state becomes the bright mode; it is easily excited by the input light. Between the x- and the y-polarized incident directions, the resonant energy shifts about 0.3 meV corresponding to the bonding and anti-bonding energy.

4.2.2 Field enhancement factor

We estimate the field enhancement factor by averaging of the intensity $\|E\|^2$ over the 4nm × 4nm square around the hotspot.

$$\frac{1}{l^2}\int_{-\frac{l}{2}}^{\frac{l}{2}} \mathrm{d}x \int_{-\frac{l}{2}}^{\frac{l}{2}} \mathrm{d}y \|\boldsymbol{E}(x, y, z=0)\|^2 \tag{4.1}$$

The spectrum of the intensity enhancements is plotted in Fig. 4.4(a). As shown in the figure, the intensity enhancement of the x-polarization incident is larger than that of y-polarization. At the resonant condition ($\hbar\omega = 3.2067$ eV), the maximum enhancement factor is estimated to be $\|E\|^2 \sim 10^3$.

Next, we estimate the Q factor of the nanogap. The Q factor can be expressed as the ratio between the resonant frequency and the full-width of half-maximum (FWHM):

$$Q = \frac{\omega_{\mathrm{L}}}{2\gamma_{\mathrm{L}}} , \tag{4.2}$$

where ω_{L} and γ_{L} are determined by the Lorentizan curve fitting:

$$L(\omega) = A_0 + \frac{A}{(\omega - \omega_{\mathrm{L}})^2 + \gamma_{\mathrm{L}}^2} . \tag{4.3}$$

Here, by fitting Eq. (4.3) into the peak at $\hbar\omega = 3.2067$ eV, the Q factor reaches about $\sim$ 12000. Therefore, due to the large Q factor, this new nanogap can be considered as a photonic cavity.

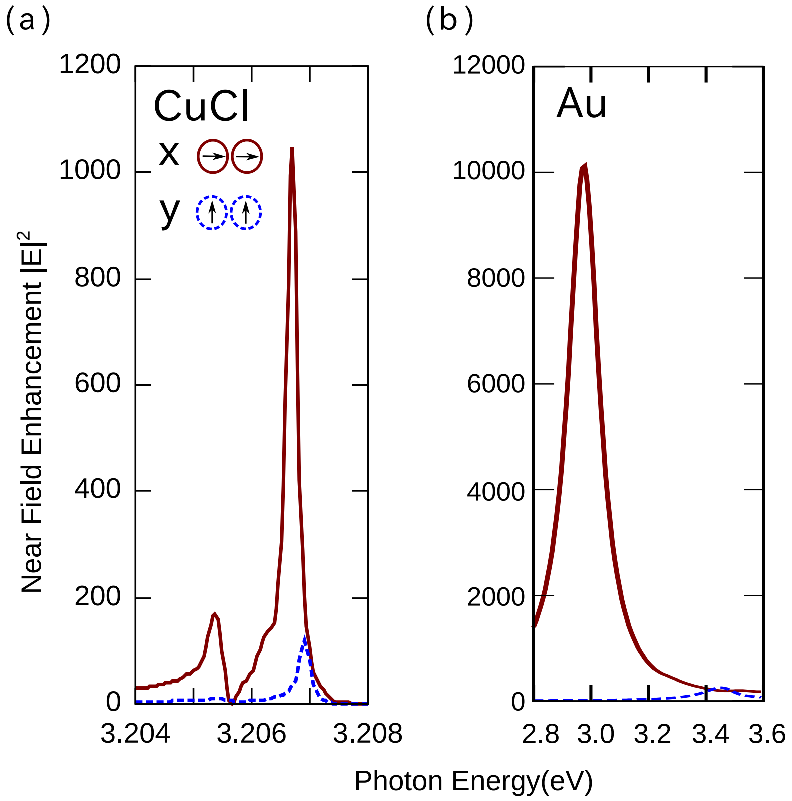

Figure 4.4: Spectral intensity enhancement at the hotspot of the dimer nanodisk consists of (a) the CuCl and (b) the gold. The red (solid) line denotes x-polarized incident and the blue (dashed) line denotes y-polarized incident.

4.2.3 Spectral properties; semiconductor vs metallic nanogap

We also calculate the field enhancement factor of a gold- disk nanogap with the same structure. To describe the gold permittivity, we use a Debye model:

$$\varepsilon_{\mathrm{p}}(\omega) = \varepsilon_0 \left[1 - \frac{(\hbar\omega_p)^2}{(\hbar\omega)^2 + i(\hbar\omega)(\hbar\gamma)} \right] , \tag{4.4}$$

where $\hbar\omega_p$ is the plasma frequency and $\hbar\gamma$ is the damping constant. For gold, we employ the parameter: $\hbar\omega_p = 8.9$ meV and $\hbar\gamma = 50$ meV, which agrees well with experimental data at $T = 40°\mathrm{K}$. Fig. 4.4(b) shows the spectrum of the intensity enhancements of the gold nanogap. Similar to the semiconductor, there is the larger enhancement factor for the x-polarized incident field. The maximum enhancement factor reaches to $\sim 10^4$ order at the resonant condition ($\hbar\omega = 3.0$ eV). It is about 10 times larger than that of the semiconductor. On the other hand, due to the large losses of the plasma oscillation, the Q factor (≈ 30) is much smaller than that of the semiconductor.

Next, we perform the EM simulation of the dimer of the ring depicted in Fig. 4.1(b). Fig. 4.5 shows the resonant energy and the maximum enhancement as a function of the ring width S. As the ring width decreases, the resonant energy is blue-shifted due to the quantum confinement effect, and the enhancement factor is suppressed linearly. This behaviour originates from that the absorbing cross section of the nanogap is also proportional to the ring width S. As shown in here, it is obvious that a field at the hotspot strongly depends on the shape and size of the nanostructure. In particular, the cross-section area is expected to be the dominant for the enhancement factor. In the following section, we discuss the dependency of the geometrical parameters.

4.2.4 Dependencies of the geometrical shape

Next, we investigate a dimer of triangular prism-shaped block which tips directed each other. This structure, often known as the bow-tie nanogap, is one of the most popular design in the plasmonics.

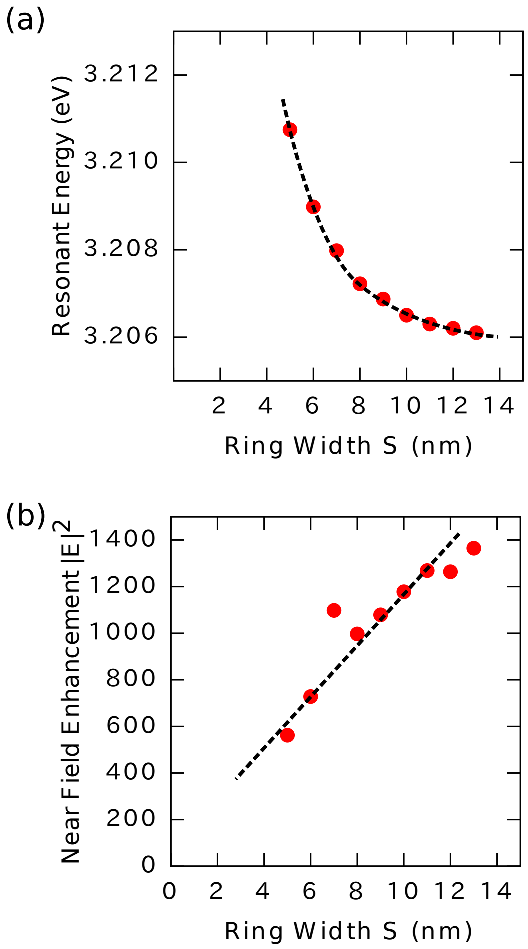

Figure 4.5: (a) Resonant energies of the ring-shaped nanodimer as a function of the ring width S. (b) Maximal enhancement in the hotspot at the resonant condition.

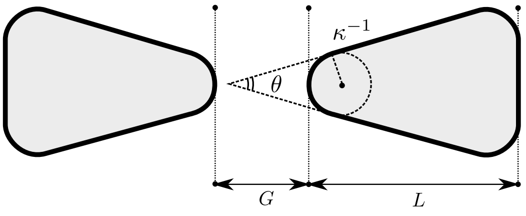

Figure 4.6: Schematic model of the bow-tie structure with the tip angle θ and the curvature radius κ^{-1}.

A schematic illustration of the nanogap structure and parameters definitions are depicted in Fig. 4.6. In the previous section, we show that the field enhancement is very sensitive to the shape of nanoblocks. Here we investigate the influence of the curvature radius κ^{-1} and the tip angle θ. For convenience, we fix the gap spacing width as (G = 5 nm), the thickness (h = 10 nm), and the volume ($V = 7000\text{nm}^3$). The polarization direction of the incident light is assumed to be parallel to the gap. We calculate the field enhancement of the semiconductor (CuCl) and metallic (Au) nanogap with the same structure. Fig. 4.7(a) shows the spectral intensity enhancement of the semiconductor one. For the metallic nanogap, only one resonant peak appears in the spectra and its maximum enhancement factor is suppressed with increasing the angle θ. On the other hand, for the semiconductor nanogap (CuCl), there are three peaks corresponding the exciton states. In contrast to the metallic nanogap, the θ dependence of the intensity enhancement is not straightforward. For the low θ, the intensity enhancement increase with θ. Fig. 4.8 shows θ-dependence with the three different curvature.

Fig. 4.9(b) and Fig. 4.10(b) show the maximum enhancement factor as a function of the curvature radius for the metallic and semiconductor nanogaps, respectively.

For the plasmonic nanostructure, it is well known that the sharp edge and the small curvature of the corner are suitable for the strong intensity enhancement. However, for the semiconducting nanostructure, the large curvature radius and the blunt edge is preferable. This behavior is originating from the wavefunction of the confined exciton. For the sharp edge, the excitons wave function can not reach to the tip part. This effect weakens the electric field at the gap region. In similar manner, the field enhancement decreases with increase of the curvature radius. extends near the edge for blunt geometry [See Fig. 4.10]

4.3 Conclusion

In this study, we propose a new nano-gap cavity utilizing exciton resonance of semiconductor. We considered the semiconductor nano-gap which consists of a dimer of CuCl nano-blocks. This CuCl nano-gap has a strong hot spot

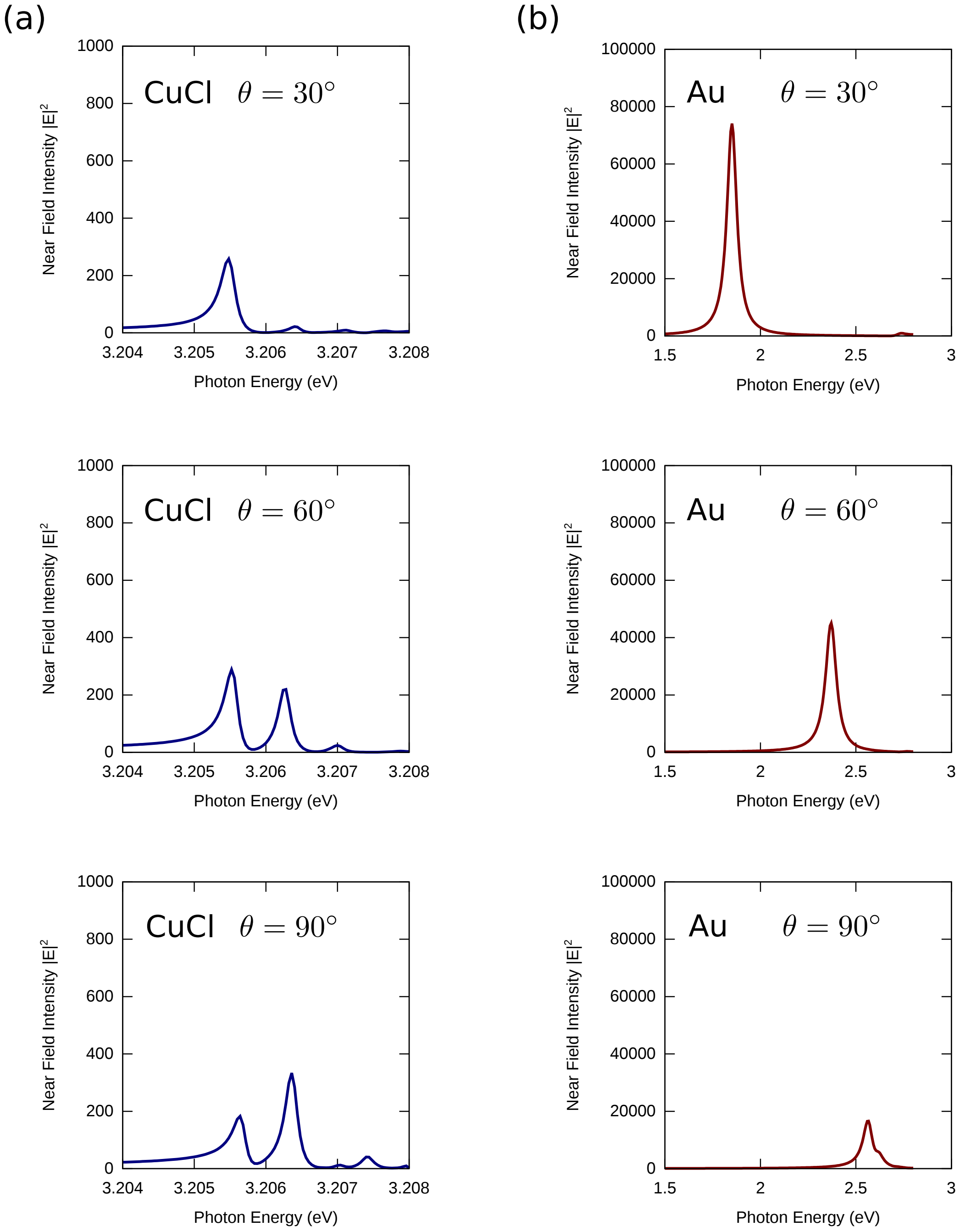

Figure 4.7: Spectral intensity enhancement at the center of the bow-tie nanogap consists of (a) CuCl and (b) Au(gold). The calculation is performed for $theta = 30, 60$ and 90 with the curvature radius $\kappa^{-1} = 1.0$ nm

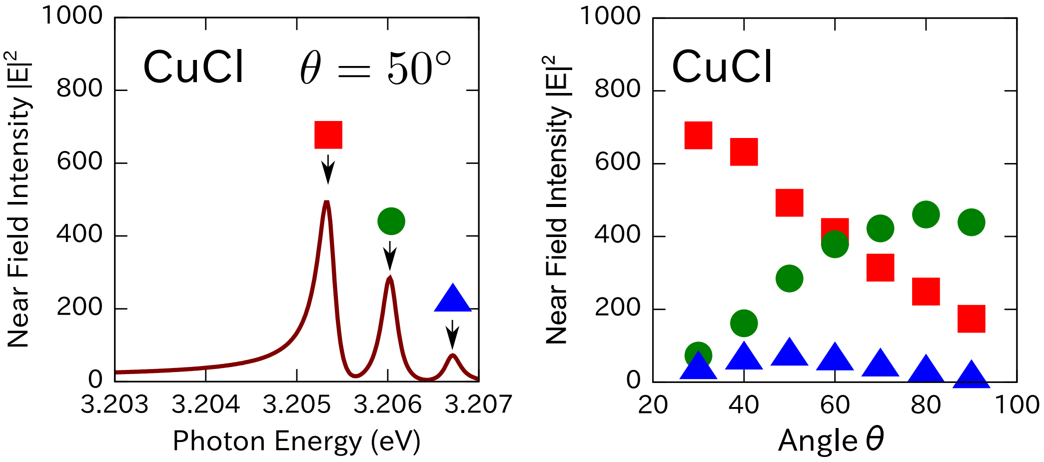

Figure 4.8: (a) Spectral intensity enhancement of the bow-tie nanogap and $\theta = 50°$. (b) Maximum enhancement factor as a function of the angle θ. The curvature radius κ^{-1} is fix to 3 nm. The red squares, the blue circles and the green triangles represent the first three resonant peaks

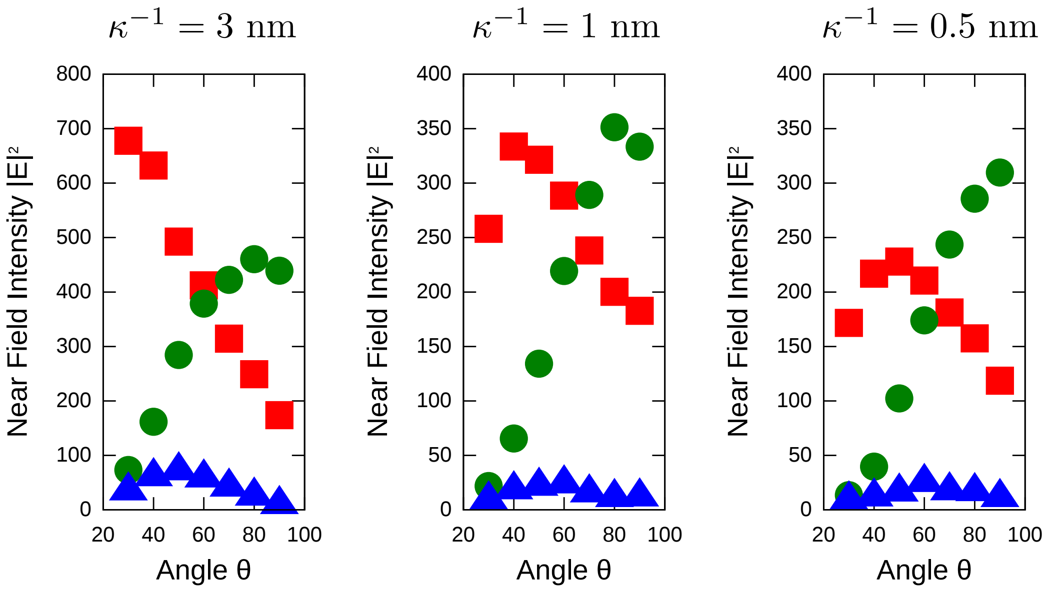

Figure 4.9: Maximum enhancement factor of the semiconductor nanogap for the various curvature radius κ^{-1}: 2.0, 3.0, 4.0 and 5.0 nm

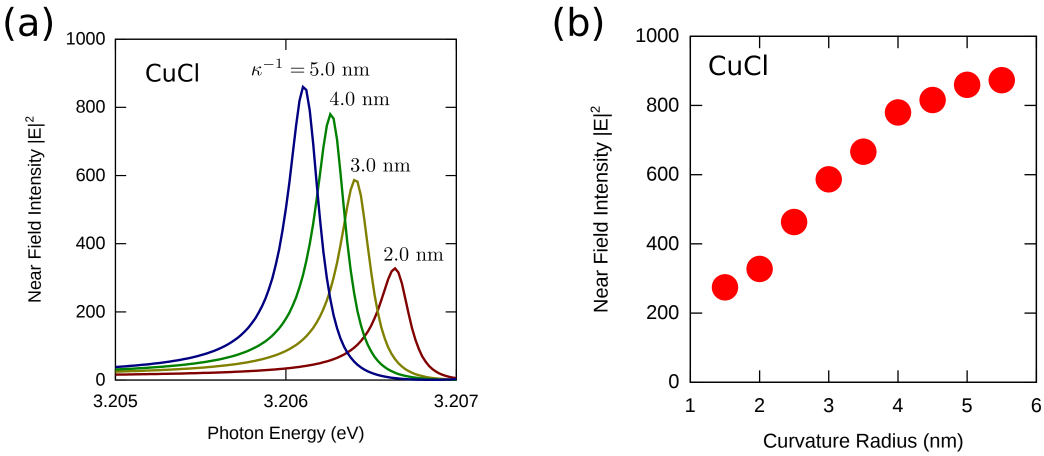

Figure 4.10: Maximum enhancement factor of the metallic nanogap for the various curvature radius κ^{-1}: 2.0, 3.0, 4.0 and 5.0 nm

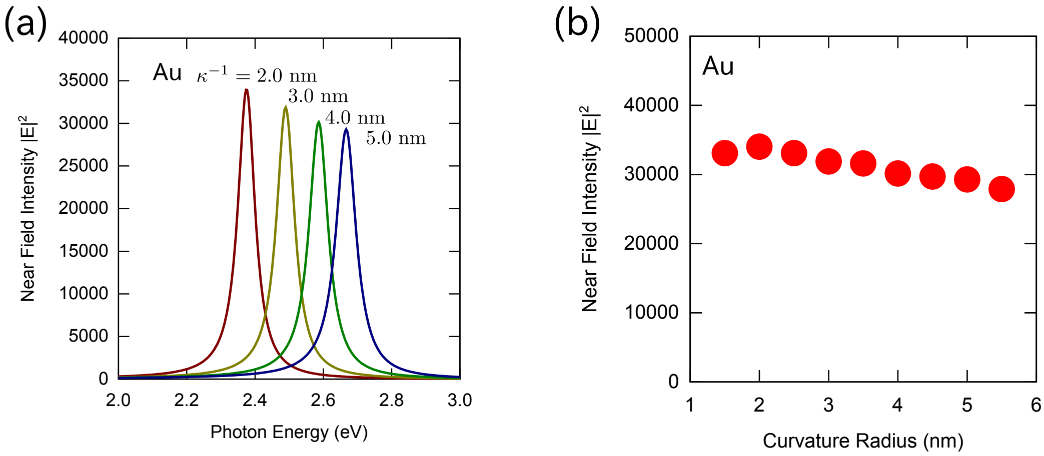

Figure 4.11: The spectral intensity enhancement of the metallic nanogap for the various curvature radius κ^{-1}: 2.0, 3.0, 4.0 and 5.0 nm

with large enhancement factor ($\approx 10^3$) at $T = 40$ K. This enhancement factor of CuCl is about 10 times smaller than the factors of metallic antennas. However, the hotspot of the semiconducting antenna exhibits much higher Q factor ($\approx 10^4$) which exceeds the limitation of plasmon resonators. Our result suggests the semiconducting antenna would function as a new type of photonic cavity. The calculation method is based on a finite element method which can take into account exciton resonance. We also systematically study the geometry dependence of the enhancement factor and Q factor. In contrast to metallic antenna, blunt edges of semiconducting islands at the gap are preferable in order to achieve high enhancement factor. This is because of the fact that exciton wave function extends near the edge for blunt geometry.

Chapter 5

Vacuum Rabi splitting at semiconductor nanogap

In the past decade, the observation of the cQED (cavity quantum electrodynamics) effects are realized by utilizing quantum dots and microscopic photonic cavities [34, 25, 23]. These solid-state cQEDs enable a mount of applications, such as the single quantum dot lasers, the high-gain parametric amplifications [27], the high-efficiency entangled photon generation [3], and the various quantum infomation devices [5]. The strength of the light-matter interaction is characterized by the coupling constant g and the decay constant γ, and the phenomenon are divided into two regions, *i.e.*, a weak and a strong coupling regime. In the weak coupling regime ($2g \ll \gamma/2$), the radiative decay time of material excitation is considerably reduced (Purcell effect) [24]. In the strong coupling regime ($2g \gg \gamma/2$), the light-matter interaction results in the two coupled states exhibiting an anticrossing behaviour (Rabi splitting) [18]. The minimun energy difference of the splitting, which corresponds to the coupling constant $2\hbar g$, is also denoted as $\hbar\Omega_{\mathrm{R}}$ (Rabi splitting energy). This value can be written as $2\mu\sqrt{\hbar\omega/2\varepsilon_0 V_{\mathrm{mode}}}$, where V_{mode} is the cavity mode-volume, and $\hbar\omega$, μ are the excitation energy and transition dipole moment of a matter, respectively. Therefore, the Rabi splitting energy becomes larger for smaller V_{mode} in addition to the larger μ. The spectral width corresponding to the coupled states becomes narrower with increase of the quality (Q) factor. Therefore, the small mode-volume and large Q factor are necessary for photonic cavities to observe a clear Rabi splitting.

In the previous experiments, the photonic crystal cavity [34], the micropillar cavity [25], and the micro-disk cavity [23] are utilized to observe the vacuum Rabi splitting. However, for conventional photonic cavities , the cavity-mode volume is restricted to the volume characterized by the light wavelength (diffraction limit). The light confinement becomes a key issue to realize the cQEDs.

A localized surface plasmon resonance (LSPR) of metallic nanostrucrures makes possible to reduce the mode-volume beyond this limitation. For example, the dimer of the metallic particles with nanogap structure provides very intense electric field, which is called as a hotspot at the gap region [32]. The cavity mode-volume of metallic nanogap cavities reaches the cube of subwavelength exceeding the diffraction limit. By using such plasmonic nanogap, the weak coupling by the hotspot has been achieved. Akimov *et al.* [4] has estimated the Purcell factor of order $F = 10^3$. For the strong coupling, Schlather *et al.* [29] have reported the observation of a giant Rabi splitting of molecular excitons placed at the metallic nanogap cavity. Although the giant splitting energy, each spectral width of the two peaks is very broad and comparable to the splitting energy because of the large plasmon decay. Generally, $\hbar\Omega_{\mathrm{R}} \gg \hbar\gamma/2$ should be satisfied to reach for the strong coupling regime. However, for the plasmonic nanogap, the decay is not small enough for this criterion. Such a situation is transitional from the Rabi splitting to the Fano-like behavior [28].

In this work, we propose and analyze a new type of the photonic cavity constructed by semiconductor nanostructures, in which resonant scattering by exciton causes a hotspot at the nanogap. The spectral width of the confined exciton is much smaller than that of the surface plasmon, and thus, the cavity Q factor is significantly improved. The semiconductor nanogap cavity has also small mode volume exceeding the diffraction limit. We theoretically demonstrate the vacuum-Rabi splitting of a two-level emitter placed on the gap region. The classical electromagnetic (EM) method can not treat the effect of the confined exciton. Therefore, we have developed an new finite element method (FEM) based simulation method.

In this chapter, We theoretically demonstrate the vacuum-Rabi splitting of a two-level emitter placed on the gap region.

5.1 Model

In this work, we consider a nanogap consisting of a dimer of the spherical semiconductor particle of $L = 7$ nm radius, these two particles are separated by $G = 8$ nm. The schematic picture is illustrated in Fig. 5.1(a). In this case, we compute the light scattering by the nanogap structure. The incident light is assumed to be a plane wave, which is linearly polarized with the electric vector parallel to the gap structure. The electric field calculations are performed based on a finite element method (FEM) technique which takes account into the exciton effects. The electric field calculations are performed based on FEM technique which takes account into the exciton effects. We use the parameter of CuCl (c.f. Table 3.1). As shown in the previous section, such semiconductor nanogap structure can be considered as the photonic cavity.

In addition, we investigate the strong coupling between the cavity mode and the matter. In this case, we consider a two-level emitter, which represents a quantum dot (QD) or a cluster of aggregated dye molecules, placed in the gap region. [See Fig. 5.1(b)] The emitter is assumed to be a spherical particle of $R = 2$ nm radius. We use the dielectric function of a Lorentz oscillator model:

$$\varepsilon(\omega) = \varepsilon_0 \left(1 - \frac{A}{(\hbar\omega)^2 - (\hbar\omega_0)^2 + i(\hbar\omega)(\hbar\gamma_0)}\right) ,$$

where ω_0 and γ_0 are the resonant frequency and the non-radiative decay constant of the oscillator, respectively. The parameter A is defined as

$$A = \frac{e^2}{m_\mathrm{e}\varepsilon_0 V_\mathrm{emit}} f \tag{5.1}$$

with

$$f = \frac{2\omega_0 m_\mathrm{e}}{\hbar e^2}\mu^2 , \tag{5.2}$$

(a) Empty nanogap cavity

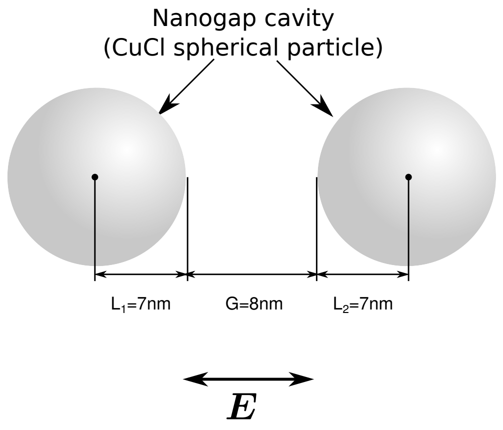

(b) Emitter-cavity coupled system

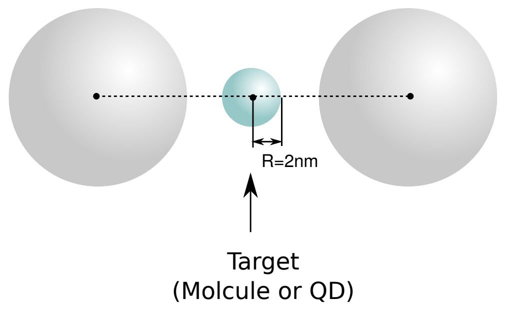

Figure 5.1: Schematic picture and the parameter definitions of (a) the empty nanogap cavity and (b) the cavity-emitter coupled system. We assume that the polarization direction of the incident light is parallel to the gap structure.

where e and m_e are the charge and mass of the electron, respectively, f is the oscillator strength, and μ is the transitional dipole moment. V_emit denotes the volume of the emitter, which can be written as $4\pi R^3/3$. Fig. 5.2(a) shows the scattering spectra of the single emitter for the transitional dipole moment of $\mu = 8 \sim 12$ D. As increasing the transition dipole moment, the resonant peak of the single emitter is blue-shifted from the exact resonant frequency of the Lorentz oscillator ω_0 (radiation shift). Therefore, for convenience, we denoted the peak position by the excitation energy $\hbar\omega_\mathrm{ex}$, which can be expressed as

$$\hbar\omega_\mathrm{ex} = \hbar\omega_0 + \Delta\hbar\omega_\mathrm{shift} \ . \tag{5.3}$$

Fig. 5.2(b) shows the radiation shifts as a function of the transitional dipole moment. In the following section, we calculate the optical spectra of the cavity-emitter coupled system with varying the parameters of $\hbar\omega_\mathrm{ex}$ and μ.

5.2 Results

The calculated scattering sperctra of the empty nanogap cavity is depicted in Fig. 5.1(b). A sharp peak appears at $\hbar\omega_\mathrm{cav} = 3.2085$eV representing an eigenstate of the confined exciton. The decay constant, which is obtained from the full-width at half-maximum (FWHM) of the resonant peak, is estimated to be $\hbar\gamma_\mathrm{cav} = 227\mu$eV. This value is about two times larger than that of the bulk exciton $\hbar\gamma_\mathrm{CuCl} = 100\ \mu$eV due to the radiation decay from the nanogap. The corresponding Q factor is $Q \sim 1.3 \times 10^4$, which easily exceeds the limitation of that of the plasmonic cavity ($Q < 10^2$).

For the cavity-emitter coupled system, the calculated scattering spectra is plotted as the solid blue line in Fig. 5.4. The excitation energy of the bared emitter is fixed to be same as that of the nanogap cavity ($\hbar\omega_\mathrm{ex} = \hbar\omega_\mathrm{cav} = 3.2085$ eV). The transition dipole moment is assumed to be $\mu = 10$ Debyes, which is as small as the dye molecules. When the emitter is inserted into the gap region, the calculated spectra exhibits two peaks separated by 0.6 meV: the upper and the lower levels ($\hbar\omega_- = 3.2082$ eV and $\hbar\omega_+ = 3.2088$ eV). We assume the excitation energy of the bared emitter is same as the cavity

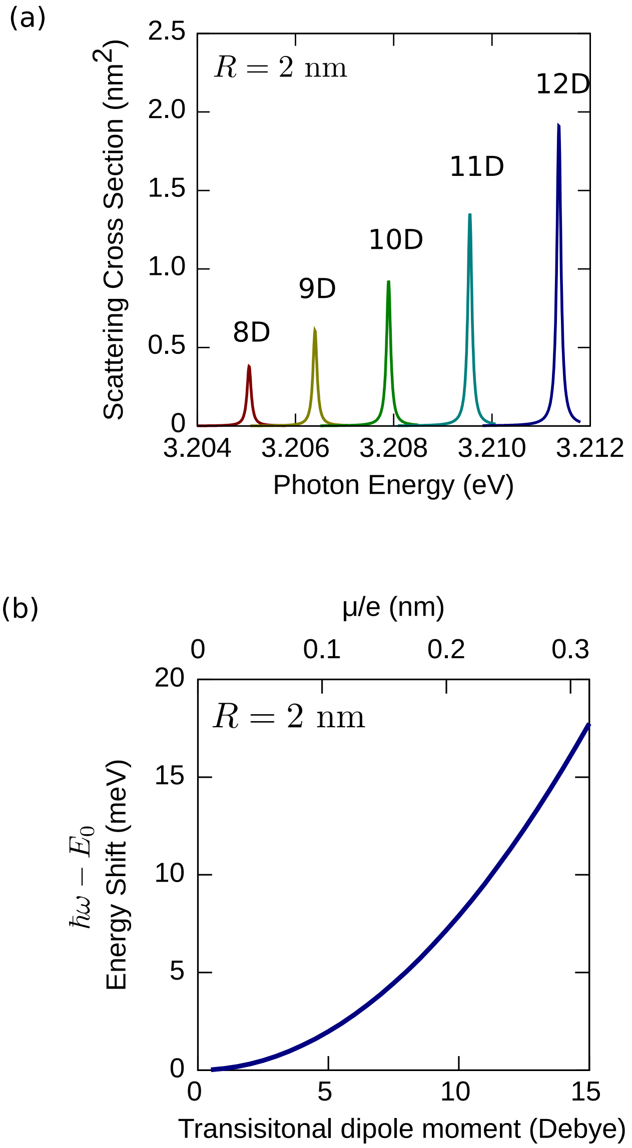

Figure 5.2: (a) Scattering spectra of the spherical particle of $R = 2$. The position of the peak is blue-shifted with increasing the dipole moment. (b) Energy shifts of the resonant peak as a function of the dipole moment.

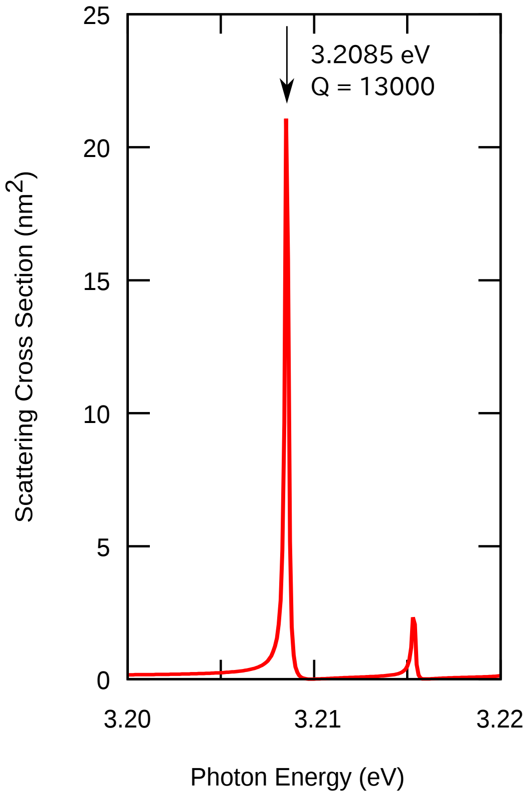

Figure 5.3: Scattering spectra of the empty nanogap cavity. A sharp resonant peak appears at $\hbar\omega_{\mathrm{cav}} = 3.2085$ eV; the Q factor is estimated to be $\approx 1.2\times10^4$.

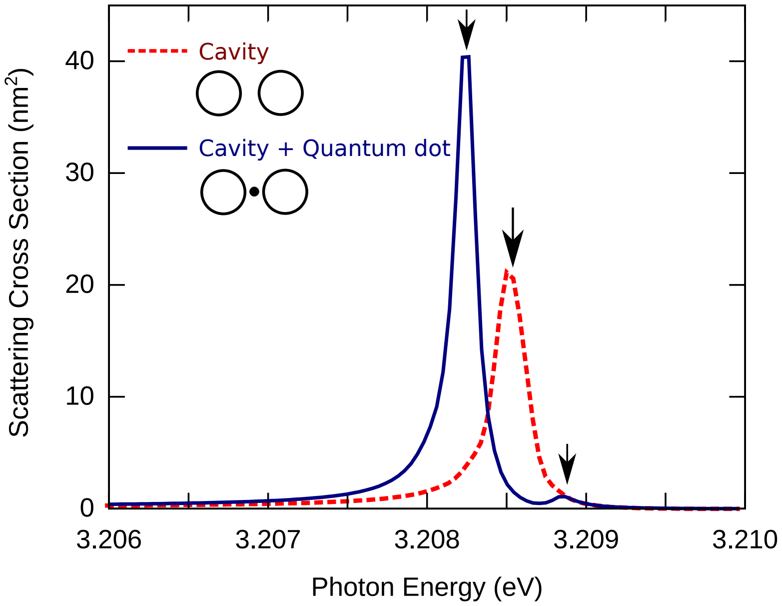

Figure 5.4: Scattering spectra of the empty cavity (dashed line) and the cavity-emitter coupled system (solid line). The excitation energy of the emitter is assumed to be same as that of the cavity mode ($\hbar\omega_{\text{cav}} = \hbar\omega_{\text{ex}} = 3.2085$ eV) and the transition dipole moment is set to be $\mu = 10$ D. For the coupled system, a single overlapped peak splits into two Rabi peaks.

resonant energy ($\hbar\omega_{\mathrm{ex}} = \hbar\omega_{\mathrm{ex}} = 3.2085$ eV). The transition dipole moment is set to be $\mu = 10$ D, which is as small as the dye molecules. When the emitter is inserted into the gap region, the calculated spectra exhibits two peaks separated by 0.5 meV: the upper and the lower branches. This peak splitting is a result of the strong coupling in the nanogap cavity.

Fig. 5.5 plots the electric field distribution on $z = 0$ plane at the resonant condition. This profile shows a hotspot appears in the gap regions; the incident light is aggregated into this point and amplified about 10^3 times stronger.

Next, we calculate the optical spectra with varying the excitation energy $\hbar\omega_{\mathrm{ex}}$. It is obvious that the peak position of the bared emitter is progressively red-shifted with decreasing $\hbar\omega_{\mathrm{ex}}$. [See Fig. 5.6(a)] In experiments, the modification of the excitation energy can be accomplished by controlling the temperature of the system [34, 25, 23]. The spectra of the cavity-emitter coupled system is depicted in the Fig. 5.6(b). A significant anti-crossing behaviour by the vacuum Rabi splitting appears.

As shown in the previous section, the hybridization of individual excited states result in the bonding and the antibonding states. In this case, the bonding state, which corresponds to the in-phase oscillation of the dipole moments, is allowed to be excited (bright mode). An interaction between the bright mode and the two-level emitter forms the two state: the upper and lower branches. The schematic diagram of the hybridization energy is illustrated in Fig. 5.7. In this case, the bonding state corresponds to the mode in which the dipole moments of two particles oscillate in phase with each other. This state is appeared in the optical spectra (bright mode) and becomes the cavity mode $\hbar\omega_{\mathrm{cav}}$. On the other hand, due to the optical selection rules, the anti-bonding state corresponding to the out-of-phase oscillation is not easily excited by light (dark mode). The interaction between the bright mode and the emitter forms the two state: the upper and lower states.

These states are given by the Jaynes-Cummings model, which is written as

$$\hat{\mathcal{H}}_{JC} = \hbar\omega_{\mathrm{cav}}\hat{a}^\dagger\hat{a} + \frac{\hbar\omega_{\mathrm{ex}}}{2}\hat{\sigma}_z + \frac{\hbar\Omega_{\mathrm{R}}}{2}\left(\hat{a}^\dagger\hat{\sigma}_- + \hat{a}\hat{\sigma}_+\right) ,$$

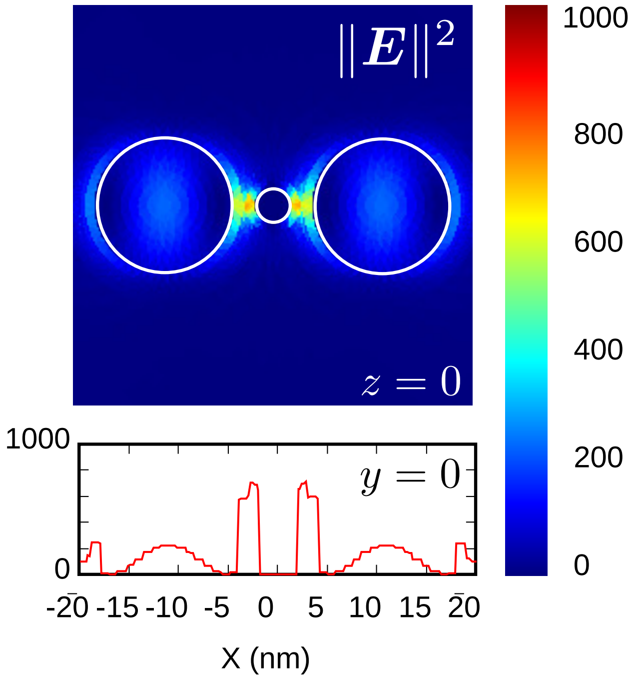

Figure 5.5: Electric field distributions of the cavity-emitter coupled system at the resonant condition ($\hbar\omega = 3.20824$ eV). (a) Top of view and the field intensity as a function of x and y at $z = 0$. (b) Field intensity as a function of the x at $y = z = 0$. The intensity is normalized to the incident field ($\|\boldsymbol{E}^{(\mathrm{inc})}\|^2 = 1$).

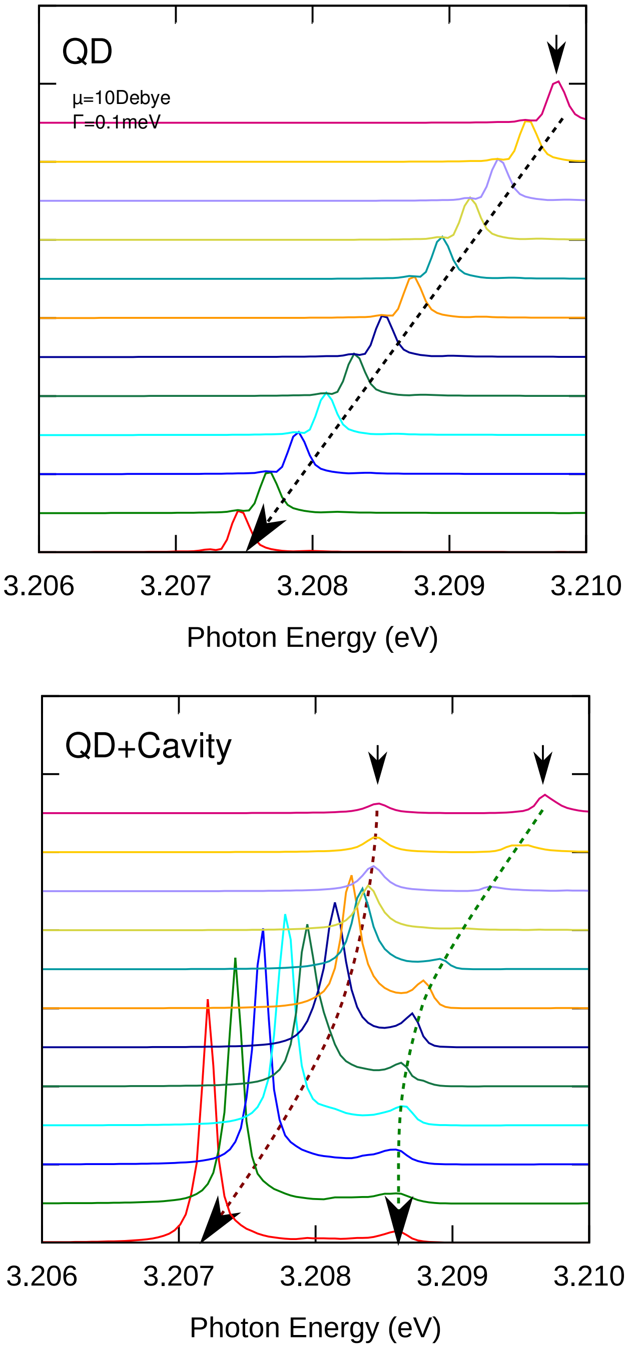

Figure 5.6: Spectral intensity enhancement at the center of the gap with various excitation energy $\hbar\omega_{\mathrm{ex}}$. (a) Calculated spectra of the bared emitter. (b) Calculated spectra of the cavity-emitter coupled system. This spectra exhibits an anti-crossing behavior originates from the vacuum Rabi splitting.

where $\hat{a}^\dagger$ and $\hat{a}$ are the creation and destruction operators for the cavity mode, and $\hat{\sigma}_z$, $\hat{\sigma}_\pm$ are the pseudospin operators for the two-level emitter. The eigenenergies of the upper and lower levels take the form

$$\hbar\omega_\pm = \frac{(\hbar\omega_{\mathrm{cav}} + \hbar\omega_{\mathrm{ex}}) \pm \sqrt{(\hbar\omega_{\mathrm{cav}} - \hbar\omega_{\mathrm{ex}})^2 + (\hbar\Omega_{\mathrm{R}})^2}}{2} \ . \tag{5.4}$$

By fitting Eq. (5.4) into the calculated peak positions, the Rabi splitting energy is estimated to be $\hbar\Omega_{\mathrm{R}} = 580$ μeV (for $\mu = 10$ Debyes).

The Rabi splitting energy is determined by fit Eq. (5.4) into the obtained peak positions. Fig. 5.2(a)-(e) shows the dispersion curves for various transision dipole moment. The horizontal axis is the deference between the cavity resonant energy and the peak position of the emitter; $\hbar\omega_{\mathrm{cav}} - \hbar\omega_{\mathrm{ex}}$ (detuning). The plotted points denote the obtained upper and lower peak positions, and the blue line is the fitting function (5.4).

Fig. 5.2(f) shows the Rabi splitting energy as a function of the transitional dipole moment. Generally, the Rabi splitting energy can be expressed as

$$\hbar\Omega_{\mathrm{R}} = 2\mu\sqrt{\frac{\hbar\omega_{\mathrm{cav}}}{2\varepsilon V_{\mathrm{mode}}}} \ . \tag{5.5}$$

As shown as the above, the Rabi splitting energy is expected to be proportional to the dipole moment μ. Therefore, the mode volume can be determined by the fitting parameter. The mode volume of this nanogap is estimated to be $V_{\mathrm{mode}} = 1.2 \times 10^{-2}$ μm^3, which is about ten times smaller than the limitation of the ordinary photonic cavities [34, 25, 23]

It is well known that the LSPR of the metallic nanogap can also produce a hotspot at the center of the gap region. Recently, a giant Rabi splitting energy ($\hbar\Omega_{\mathrm{R}} \approx 200$ meV) has beem reported for the molecular excitons in the metallic nanogap [29]. The corresponding cavity mode-volume is estimated to be $10^1 \sim 10^2$ nm^3 order, which is incredibly smaller than that of the ordinarily photonic cavities. However, the large losses of the plasma oscillation prevents the observation of the clear Rabi splitting.

In general, $\hbar\Omega_{\mathrm{R}} \gg (\hbar\gamma_{\mathrm{cav}} - \hbar\gamma_{\mathrm{ex}})/2$ is should be satisfied. For the metallic nanogap, the decay constant reaches $\hbar\gamma_{\mathrm{cav}} > 100$ meV. The $\hbar\Omega_{\mathrm{R}}$ is at most comparable to the decay constant. For a small dipole moment, a fano-like dip appears instead of the Rabi splitting.

For the semiconductor nanogap, our results show $\hbar\gamma_{\text{cav}} \approx 200$ μeV and $\hbar\gamma_{\text{ex}} \approx 100$ μeV. Thus, it is obviously that the Rabi splitting appears at small dipole moment of a few Debyes. [See Fig. 5.2(f)] We believe the semiconductor nanogap enables the observation of the clearer peak splitting.

5.3 Conclusion

In this paper, we have proposed a new nanogap structure consisting of a semiconductor dimer, and computed the vacuum-Rabi splitting of a two-level system placed at the nanogap. The results show that the splitting energy reaches ≈ 0.5 meV for dipole moment ≈ 10 Debyes of the two-level system. The corresponding mode volume $10^{-2}\mu\text{m}^3$ is much smaller than that of a photonic slab cavity.

In principle, the small cavity-mode volume and large Q factor are necessary for photonic cavities to observe a clear Rabi splitting. In the previous experiments, two major types of the photonic cavities have been utilized. The first type is the nanostructure consisting of the non-resonating semiconductor, (*i.e.*, the conventional photonic cavities such as the photonic crystals). For such structure, the high-Q factor can be achieved, on the other hand, the mode-volume is restricted by the diffraction limit. The second type is the nanostructure consisting of the metal (*i.e.*, the plasmonic cavities). The LSPR provides the subwavelength mode-volume, on the other hand, the Q factor is strongly diminished. The crucial point of this study is a new photonic cavity consisting of the resonating semicondutor. This new structure has two remarkable merits: (i) the mode-volume is smaller than the conventional photonic cavity. (ii) the Q factor is larger than the plasmonic cavity. The above properties provide a significant advantage for the ordinary designes, and they are suited for the cQED applications. We believe the semiconducting nanostructure becomes the powerful tool for the nanophotonics.

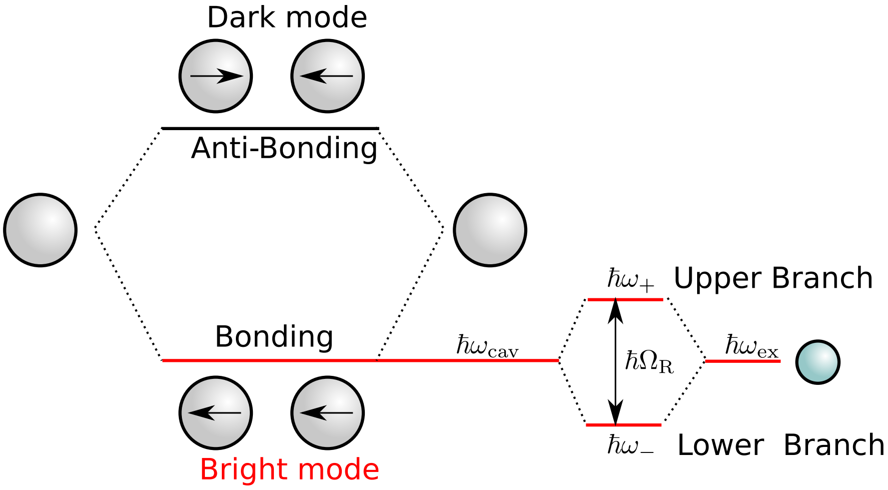

Figure 5.7: Hybridization energy diagram of the cavity-emitter coupled system; The interaction between the emitter and the bright mode of the nanogap results in the two coupled state separated by $\hbar\Omega_{\mathrm{R}}$

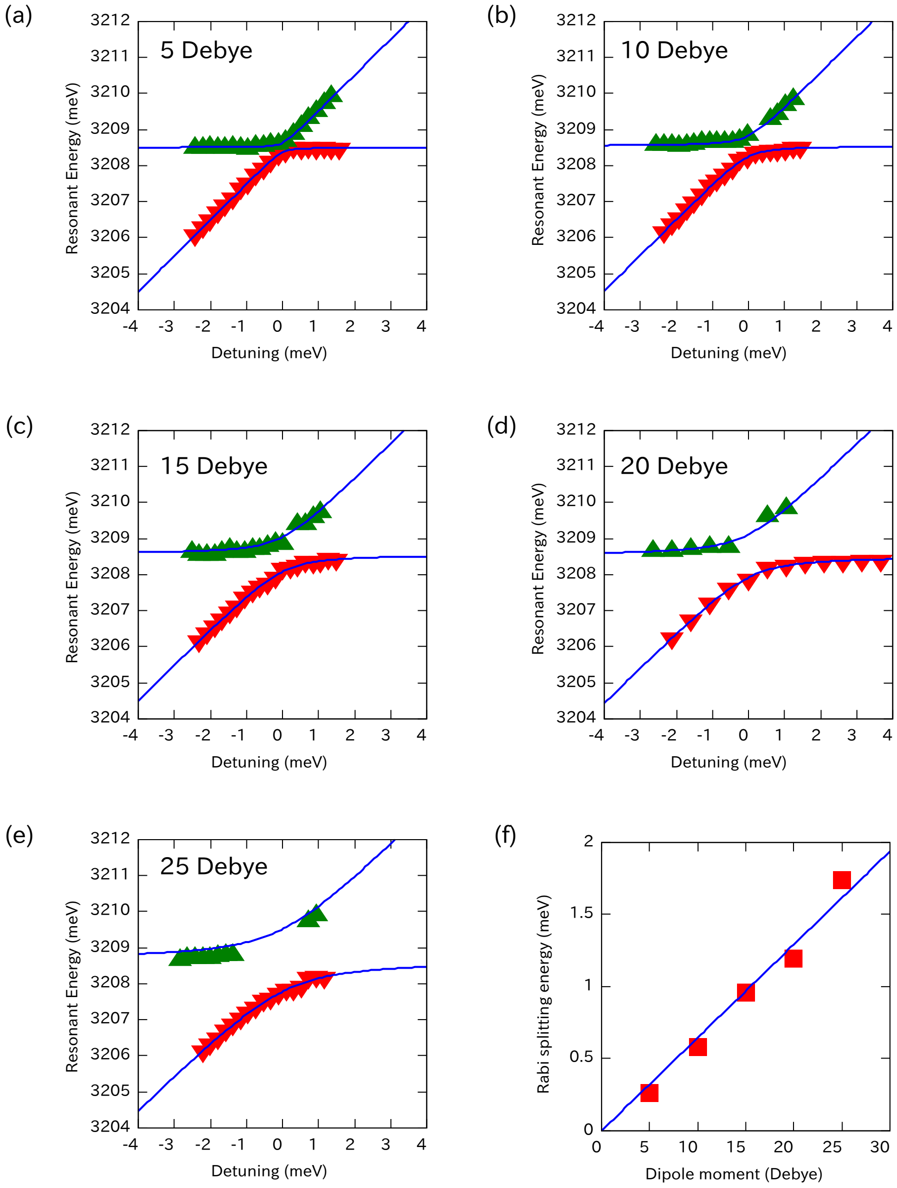

Figure 5.8: Dispersion curve; the dependence of the peak positions on the excitation energy of the emitter. The horizontal axis is the energy deference between the emitter and the cavity mode $\hbar\omega_{\mathrm{ex}} - \hbar\omega_{\mathrm{cav}}$. (a)-(e) The dispersion curves for various transision dipole moment of $\mu = 5, 10, 15, 20$, and 25 Debye. The green and red triangles represents the upper- and the lower- branch of the coupled state. The blue line is the calculated from the Eq. (5.4) (e) The Rabi splitting energy vs the transition dipole moment.

Chapter 6

Conclusion

In this thesis, we have developed a new EM simulation method applicable to the exciton resonance confined in arbitrary shape. Our method is expected to be powerful tool for structure-based design of the hotspot assisted by the exciton resonances.

For this application, we have proposed a new semiconductor-based nanogap structure utilizing exciton resonances. The result of the numerical simulation shows that this nanogap produces the localized electric field at the hotspot and acts as the high-Q photonic cavity. The obtained Q factor reaches to the order of 10^5 which easily exceeds the limitation of the plasmonic resonators ($Q < 10^2$). As well as the plasmonics, the optical properties of the nanogap are strongly depend on the geometrical parameters such as its shape, width, thickness and curvature. For example, in the case of the metal, the hotspot is localized on the edge of the nanostructure, and its the field intensity is enhanced by the edge sharpness. In contrast to the metallic nanostructures, the enhancement factor increases for flatter angle because flatter angle allows the exciton wavefunction to approach the edges near the nanogap. This is also the characteristic feature of the exciton induced hotspot.

We also theoretically demonstrated the vacuum-Rabi splitting of a two-level emitter placed on the gap region. The resulting spectra peaks exhibit, a clear anti-crossing behavior appears in the dispersion relations. The splitting energy reaches ≈ 0.5 meV for dipole moment ≈ 10D of the two-level emitter. The corresponding mode volume $\approx 10^{-2}\mu\text{m}^3$, which is 10 times smaller than that of the ordinary photonic cavity.

The significance of this study is in (i) developing the an electromagnetic (EM) simulation method based on a finite-element method (FEM) for an exciton-active media, (ii) reviewing the semiconductor-based nanogap structure as the microcavity, and (iii) demonstrating the vacuum Rabi splitting at the semiconductor nanogap. There results suggests that the semiconductor nanostructure opens a new research field in nano-optics.

In this work, we have accomplished the theoretical calculations of the proposed nanostructures. However, it has not been checked by the experiments yet. Therefore, Verification experiment is highly desirable.

Bibliography

[1] Vladimir Moiseevich Agranovich and Vitaliĭ Lazarevich Ginzburg. *Crystal optics with spatial dispersion, and excitons.* Springer-Verlag, Berlin-Heidelberg, 1984.

[2] Hiroshi Ajiki and Kikuo Cho. Longitudinal and transverse components of excitons in a spherical quantum dot. *Phys. Rev. B*, 62(11):7402–7412, 2000.

[3] Hiroshi Ajiki and Hajime Ishihara. Entangledphoton generation from a quantum dot in cavity QED. *physica status solidi (c)*, 6(1):276–279, January 2009.

[4] AV Akimov, A Mukherjee, CL Yu, and DE Chang. Generation of single optical plasmons in metallic nanowires coupled to quantum dots. *Nature*, 450(7168):402–6, November 2007.

[5] PR Berman. Cavity quantum electrodynamics. *Reports on Progress in Physics*, 69:1325–1382, 1994.

[6] JL Birman, EI Rashba, and MD Sturge. *Excitons.* North-Holland, Amsterdam, 1982.

[7] A. Bossavit. Solving maxwell equations in a closed cavity, and the question of ‘spurious modes’. *Magnetics, IEEE Transactions on*, 26(2):702–705, 1990.

[8] Alain Bossavit. A rationale for ‘edge-elements’ in 3-d fields computations. *Magnetics, IEEE Transactions on*, 24(1):74–79, 1988.

[9] Kikuo Cho and Hajime Ishihara. ABC-theory of an exciton-polariton in a slab. *J. Phys. Soc. Jpn.*, 59(2):754–764, 1990.

[10] Kikuo Cho and Masaru Kawata. Theoretical analysis of polariton interference in a thin platelet of CuCl. I. additional boundary condition. *J. Phys. Soc. Jpn.*, 54:4431–4443, 1985.

[11] A d'Andrea and R Del Sole. Wannier-mott excitons in semi-infinite crystals: Wave functions and normal-incidence reflectivity. *Phys. Rev. B*, 25(6):3714, 1982.

[12] AI Ekimov, Al L Efros, and AA Onushchenko. Quantum size effect in semiconductor microcrystals. *Sol. Stat. Commun.*, 56(11):921–924, 1985.

[13] P Halevi and R Fuchs. Generalised additional boundary condition for non-local dielectrics. I. reflectivity. *J. Phys. C: Sol. Stat. Phys.*, 17(21):3869–3888, 1984.

[14] Encai Hao and George C Schatz. Electromagnetic fields around silver nanoparticles and dimers. *The Journal of chemical physics*, 120(1):357–66, January 2004.

[15] K Inaba, K Imaizumi, K Katayama, M Ichimiya, M Ashida, T Iida, H Ishihara, and T Itoh. Optical manipulation of cucl nanoparticles under an excitonic resonance condition in superfluid helium. *Phys. Stat. solidi (b)*, 243(14):3829–3833, 2006.

[16] Jian-Ming Jin. *The Finite Element Method in Electromagnetics*. Wiley-IEEE Press, New York, 2002.

[17] Jian-Ming Jin, Jiamming Jin, and Jian-Ming Jin. *The finite element method in electromagnetics*. Wiley New York, 2002.

[18] G Khitrova, HM Gibbs, M Kira, SW Koch, and A Scherer. Vacuum Rabi splitting in semiconductors. *Nature Physics*, pages 81–90, 2006.

[19] J Lagois. Depth-dependent eigenenergies and damping of excitonic polaritons near a semiconductor surface. *Phys. Rev. B*, 23(10):5511, 1981.

[20] P Mühlschlegel, H-J Eisler, O J F Martin, B Hecht, and D W Pohl. Resonant optical antennas. *Science (New York, N.Y.)*, 308(5728):1607–9, June 2005.

[21] Shuming Nie and Steven R Emory. Probing single molecules and single nanoparticles by surface-enhanced raman scattering. *science*, 275(5303):1102–1106, 1997.

[22] S. I. Pekar. The theory of electromagnetic waves in a crystal in which excitons are produced. *Sov. Phys. JETP*, 6:785–796, 1958.

[23] E. Peter, P. Senellart, D. Martrou, a. Lemaître, J. Hours, J. Gérard, and J. Bloch. Exciton-Photon Strong-Coupling Regime for a Single Quantum Dot Embedded in a Microcavity. *Physical Review Letters*, 95(6):067401, August 2005.

[24] E. M Purcell. Spontaneous emission probabilities at radio frequencies. *Physical Review*, 69:681–681, 1946.

[25] J P Reithmaier, G Sek, A Löffler, C Hofmann, S Kuhn, S Reitzenstein, L V Keldysh, V D Kulakovskii, T L Reinecke, and A Forchel. Strong coupling in a single quantum dot-semiconductor microcavity system. *Nature*, 432(7014):197–200, November 2004.

[26] R Ruppin. Optical absorption by excitons in microcrystals. *J. Phys. Chem. Solids*, 50(9):877–882, January 1989.

[27] M Saba, C Ciuti, J Bloch, and R Andre. High-temperature ultrafast polariton parametric amplification in semiconductor microcavities. *Nature*, 414:731–735, 2001.

[28] Salvatore Savasta, Rosalba Saija, Alessandro Ridolfo, and Omar Di Stefano. Nanopolaritons: vacuum rabi splitting with a single quantum dot in the center of a dimer nanoantenna. *ACS ...*, 4(11):6369–6376, 2010.

[29] Andrea E Schlather, Nicolas Large, Alexander S Urban, Peter Nordlander, and Naomi J Halas. Near-Field Mediated Plexcitonic Coupling and Giant Rabi Splitting in Individual Metallic Dimers. *Nano letters*, 13:3281–3286, June 2013.

[30] ZK Tang, George KL Wong, P Yu, M Kawasaki, A Ohtomo, H Koinuma, and Y Segawa. Room-temperature ultraviolet laser emission from self-assembled zno microcrystallite thin films. *Appl. Phys. Lett.*, 72:3270, 1998.

[31] Yasuyuki Tsuboi, Tatsuya Shoji, Noboru Kitamura, Mai Takase, Kei Murakoshi, Yoshihiko Mizumoto, and Hajime Ishihara. Optical Trapping of Quantum Dots Based on Gap-Mode-Excitation of Localized Surface Plasmon. *The Journal of Physical Chemistry Letters*, 1(15):2327–2333, August 2010.

[32] Kosei Ueno, Saulius Juodkazis, and Toshiyuki Shibuya. Nanoparticle plasmon-assisted two-photon polymerization induced by incoherent excitation source. *Journal of the Americal Chemical Society*, 130:6928–6929, 2008.

[33] Feng Wang and Y Ron Shen. General properties of local plasmons in metal nanostructures. *Physical review letters*, 97(20):206806, 2006.

[34] T Yoshie, A Scherer, and J Hendrickson. Vacuum Rabi splitting with a single quantum dot in a photonic crystal nanocavity. *Nature*, 432(November):9–12, 2004.

[35] Marian Zamfirescu, Alexey Kavokin, Bernard Gil, Guillaume Malpuech, and Mikhail Kaliteevski. ZnO as a material mostly adapted for the realization of room-temperature polariton lasers. *Phys. Rev. B*, 65(16):161205, 2002.

Appendix

Vector spherical harmonics

In spherical polar coordinate, the scalar solution of the Helmholtz equation is given as

$$\Psi_{nm}(kr,\theta,\phi) \quad = \quad h_n(kr)P_n^{|m|}(\cos\theta)e^{im\phi} \tag{1}$$

where k is a wave number,h_n is the n-th order spherical Hankel function, $P_n^{|m|}$ is the Legendre polygonal. Hence, the integer n, m are limited at $0 \leq |m| \leq n$.

Consider the vector spherical harmonics:

$$\begin{aligned}
\mathbf{M}_{mn}(kr,\theta,\phi) =& i\frac{m}{\sin\theta}h_n(kr)P_n^m(\cos\theta)e^{im\phi}\hat{\theta} \\
& - h_n(kr)\frac{\partial P_n^m(\cos\theta)}{\partial\theta}e^{im\phi}\hat{\phi} \qquad (2) \\
\mathbf{N}_{mn}(kr,\theta,\phi) =& \frac{n(n+1)}{kr}h_n(kr)P_n^m(\cos\theta)e^{im\phi}\hat{r} \\
& + \frac{1}{kr}\xi_n'(kr)\frac{\partial P_n^m(\cos\theta)}{\partial\theta}e^{im\phi}\hat{\theta} \\
& + i\frac{1}{kr}\frac{m}{\sin\theta}\xi_n'(kr)P_n^m(\cos\theta)e^{im\phi}\hat{\phi}\ , \qquad (3)
\end{aligned}$$

where m is a integer limited for $-n \leq m \leq n$. Orthogonality of M and N are shown as follows:

$$\begin{aligned}
&\iint_{\Gamma(r)} \mathrm{d}S\boldsymbol{M}^*_{mn}\cdot\boldsymbol{M}_{m'n'}\\
&\quad=\iint \left[\left(i\frac{m}{\sin\theta}h_n(kr)P_n^m(\cos\theta)e^{im\phi}\right)^*\left(i\frac{m'}{\sin\theta}h_{n'}(kr)P_{n'}^{m'}(\cos\theta)e^{im'\phi}\right)\right.\\
&\qquad\left.+\left(-h_n(kr)\frac{\partial P_n^m(\cos\theta)}{\partial\theta}e^{im\phi}\right)^*\left(-h_{n'}(kr)\frac{\partial P_{n'}^{m'}(\cos\theta)}{\partial\theta}e^{im'\phi}\right)\right]\ r^2\sin\theta\mathrm{d}\theta\mathrm{d}\phi\\
&\quad=r^2h_n^*(kr)h_{n'}(kr)\iint \mathrm{d}\theta\mathrm{d}\phi\ \left(\frac{mm'}{\sin\theta}P_n^mP_{n'}^{m'}+\sin\theta\frac{\partial P_n^m}{\partial\theta}\frac{\partial P_{n'}^{m'}}{\partial\theta}\right)\ e^{i(m-m')\theta}\\
&\quad=4\pi r^2|h_n|^2\frac{n(n+1)}{2n+1}\frac{(n+m)!}{(n-m)!}\delta_{nn'}\delta_{mm'} \qquad (4)
\end{aligned}$$

$$\begin{aligned}
&\iint_{\Gamma(r)} \mathrm{d}S\boldsymbol{N}^*_{mn}\cdot\boldsymbol{N}_{m'n'}\\
&\quad=\iint \left[\left(\frac{n(n+1)}{kr}h_n(kr)P_n^m(\cos\theta)e^{im\phi}\right)^*\left(\frac{n(n+1)}{kr}h_n(kr)P_n^m(\cos\theta)e^{im\phi}\right)\right.\\
&\qquad+\left(\frac{1}{kr}\xi_n'(kr)\frac{\partial P_n^m(\cos\theta)}{\partial\theta}e^{im\phi}\right)^*\left(\frac{1}{kr}\xi_n'(kr)\frac{\partial P_n^m(\cos\theta)}{\partial\theta}e^{im\phi}\right)\\
&\qquad\left.+\left(i\frac{1}{kr}\frac{m}{\sin\theta}\xi_n'(kr)P_n^m(\cos\theta)e^{im\phi}\hat{\phi}\right)^*\left(i\frac{1}{kr}\frac{m}{\sin\theta}\xi_n'(kr)P_n^m(\cos\theta)e^{im\phi}\hat{\phi}\right)\right]\ r^2\sin\theta\mathrm{d}\theta\mathrm{d}\phi\\
&\quad=r^2\frac{\xi_n'^*\xi_{n'}'}{(kr)^2}\iint e^{i(m-m')\phi}\left(\frac{mm'}{\sin\theta}P_n^mP_{n'}^{m'}+\sin\theta\frac{\partial P_n^m}{\partial\theta}\frac{\partial P_{n'}^{m'}}{\partial\theta}\right)\ \mathrm{d}\theta\mathrm{d}\phi\\
&\qquad+r^2\frac{n^2(n+1)^2h_n^*h_{n'}}{(kr)^2}\iint e^{i(m-m')\phi}P_n^mP_{n'}^m\sin\theta\ \mathrm{d}\theta\mathrm{d}\phi\\
&\quad=4\pi r^2\left|\frac{\xi_n'}{kr}\right|^2\frac{n(n+1)}{2n+1}\frac{(n+m)!}{(n-m)!}\delta_{nn'}\delta_{mm'}+4\pi r^2|h_n|^2\frac{n^2(n+1)^2}{2n+1}\frac{(n+m)!}{(n-m)!}\delta_{nn'}\delta_{mm'}\\
&\qquad (5)
\end{aligned}$$

where $\Gamma(r)$ is denoted to the surface integral on the sphere of the radius r.

Similar relation is appear in the surface integral of the cross product of

$\boldsymbol{M} \times \boldsymbol{N}$.

$$\begin{aligned}
&\iint_{\Gamma(r)} \mathrm{d}\boldsymbol{S} \cdot (\boldsymbol{M}^*_{mn} \times \boldsymbol{N}_{m'n'}) \\
&\quad = \iint r^2 \sin\theta \mathrm{d}\theta \mathrm{d}\phi \ \left(i\frac{m}{\sin\theta} h_n P_n^m(\cos\theta) e^{im\phi}\right)^* \left(i\frac{1}{kr}\frac{m'}{\sin\theta}\xi'_{n'} P_{n'}^{m'}(\cos\theta) e^{im'\phi}\right) \\
&\qquad - \left(-h_n(kr)\frac{\partial P_n^m(\cos\theta)}{\partial\theta} e^{im\phi}\right)^* \left(\frac{1}{kr}\xi'_{n'}(kr)\frac{\partial P_{n'}^{m'}(\cos\theta)}{\partial\theta} e^{im'\phi}\right) \\
&\quad = r^2 \frac{h_n^* \xi'_{n'}}{kr} \iint e^{i(m-m')\phi} \left(\frac{mm'}{\sin\theta} P_n^m P_{n'}^{m'} + \sin\theta \frac{\partial P_n^m}{\partial\theta}\frac{\partial P_{n'}^{m'}}{\partial\theta}\right) \ \mathrm{d}\theta \mathrm{d}\phi \\
&\quad = 4\pi r^2 \frac{h_n^* \xi'_{n'}}{kr} \frac{n(n+1)}{2n+1} \frac{(n+m)!}{(n-m)!} \delta_{nn'} \delta_{mm'} \qquad (6)
\end{aligned}$$

Therefore, we get

$$\iint_{\Gamma(r)} \mathrm{d}S \boldsymbol{M}^*_{mn} \cdot \boldsymbol{M}_{m'n'} = 4\pi r^2 |h_n(kr)|^2 \mathcal{N}(m,n) \qquad (7)$$

$$\iint_{\Gamma(r)} \mathrm{d}S \boldsymbol{N}^*_{mn} \cdot \boldsymbol{N}_{m'n'} = 4\pi r^2 \left(\left| \frac{\xi'_n(kr)}{kr} \right|^2 + n(n+1)|h_n|^2 \right) \mathcal{N}(m,n) \qquad (8)$$

$$\iint_{\Gamma(r)} \mathrm{d}S \boldsymbol{M}^*_{mn} \times \boldsymbol{N}_{m'n'} = 4\pi r^2 \frac{h_n^* \xi'_{n'}}{kr} \mathcal{N}(m,n) \qquad (9)$$

with

$$\mathcal{N}(n,m) = \frac{n(n+1)}{2n+1} \frac{(n+m)!}{(n-m)!} \delta_{nn'} \delta_{mm'} \qquad (10)$$

Acknowledgement

This work was supported by the Graduate School of Engineering Science at Osaka University from April 2011 to March 2014. I would like to express my sincere gratitude to my supervisor, Prof. Hiroshi Katayama-Yoshida and Prof. Hiroshi Ajiki, for the professional advice and discussions. I would like to thank to Murata-san not only for her office work but also for her various support. I also acknowledge all students of the Yoshida laboratory and Kusakabe laboratory, Finally, I also thank my family and friends for their support, patience and encouragement.

List of Publications

Published

1. M.Uemoto, H.Ajiki ”Finite element method for the excitonic material”, The proceedings of 21st conference of the photophysics, pp 390-394, 2010
2. M.Uemoto, H.Ajiki ”Finite element method for the excitonic material II”, The proceedings of 22nd conference of the photophysics, pp 285-289, 2011
3. M.Uemoto, H.Ajiki ”The semiconductor nanogap as high-Q cavity” , The proceedings of 23rd conference of the photophysics, pp 417-420, 2012
4. M.Uemoto, H.Ajiki ”The calculation of the Rabi splitting for the semiconductor nanogap”, The proceedings of 24th conference of the photophysics, pp 459-462, 2013
5. M.Uemoto, H.Ajiki ”Simulation method for resonant light scattering of exciton confined in arbitrary geometry”, Optic Express, in preparation

International conferences

1. M.Uemoto, H.Ajiki, ”Finite Element Method for Electromagnetic Field Scattered by Confined Exciton”, The 10th International Conference on Excitonic Processes in Condensed Matter (EXCON 2012), No. 227, Groningen, Netherland, (7/2012)

2. M.Uemoto, H.Ajiki, "Finite Element Method for Calculating Electromagnetic Field Scattered by Semiconductor Nano-particles", The 32nd International Conference on the Physics of Semiconductors (ICPS 2012), No. 578, ETH, Switzerland, (8/2012)
3. M.Uemoto, H.Ajiki,"A New Extension of Finite Element Method for Electromagnetic Fields in Excitonic Media", International Symposium of Computec: Quantum Simulation and Design (ISC-QSD), P-86, Osaka University (10/2012)
4. M.Uemoto, H.Ajiki, "Finite Element Method for Calculating Electromagnetic Field Scattered by Semiconductor Nano-particles", 8th Handai Nanoscience and Nanotechnology International Symposium, Osaka University (12/2012)
5. M.Uemoto, H.Ajiki,"Semiconductor nano-gap antennas with high quality factor", American Physics Society (APS March Meeting 2013), BAPS.2013.MAR.V1.240 , Baltimore, US, (3/2013)
6. M.Uemoto, H.Ajiki,"The hot-spot in semiconductor nano-gap antenna", International Workshop of Computational Nano-Materials Design on Green Energy, Awaji Yumebutai International Conference Center (6/2013)
7. M.Uemoto, H.Ajiki,"Calculation of Large Rabi Splitting for Semiconductor Nanogap Microcavities",1st KANSAI Nanoscience and Nanotechnology International Symposium, P70, Osaka University (2/2014)